CHAPTER

13

HORN ANTENNAS

13.1 INTRODUCTION

One of the simplest and probably the most widely used microwave antenna is the horn. Its existence and early use dates back to the late 1800s. Although neglected somewhat in the early 1900s, its revival began in the late 1930s from the interest in microwaves and waveguide transmission lines during the period of World War II. Since that time a number of articles have been written describing its radiation mechanism, optimization design methods, and applications. Many of the articles published since 1939 which deal with the fundamental theory, operating principles, and designs of a horn as a radiator can be found in a book of reprinted papers [1] and chapters in handbooks [2], [3].

The horn is widely used as a feed element for large radio astronomy, satellite tracking, and communication dishes found installed throughout the world. In addition to its utility as a feed for reflectors and lenses, it is a common element of phased arrays and serves as a universal standard for calibration and gain measurements of other high-gain antennas. Its widespread applicability stems from its simplicity in construction, ease of excitation, versatility, large gain, and preferred overall performance.

An electromagnetic horn can take many different forms, four of which are shown in Figure 13.1. The horn is nothing more than a hollow pipe of different cross sections which has been tapered (flared) to a larger opening. The type, direction, and amount of taper (flare) can have a profound effect on the overall performance of the element as a radiator. In this chapter, the fundamental theory of horn antennas will be examined. In addition, data will be presented that can be used to understand better the operation of a horn and its design as an efficient radiator.

13.2 *E*-PLANE SECTORAL HORN

The *E*-plane sectoral horn is one whose opening is flared in the direction of the *E*-field, and it is shown in Figure 13.2(a). A more detailed geometry is shown in Figure 13.2(b).

*Portions of this chapter on aperture matched horns, multimode horns, and dielectric-loaded horns were first published by the author in [2]. Copyright 1988, reprinted by permission of Van Nostrand Reinhold Co.

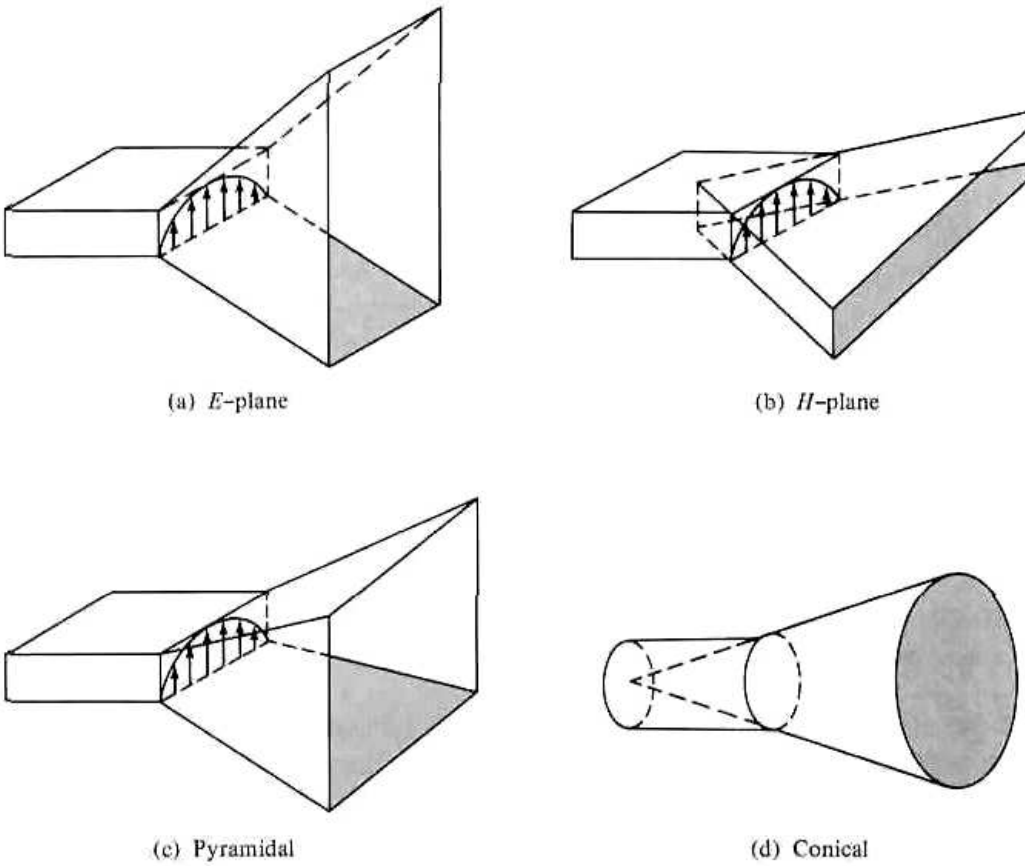

Figure 13.1 Typical electromagnetic horn antenna configurations.

13.2.1 Aperture Fields

The horn can be treated as an aperture antenna. To find its radiation characteristics, the equivalent principle techniques developed in Chapter 12 can be utilized. To develop an exact equivalent of it, it is necessary that the tangential electric and magnetic field components over a closed surface are known. The closed surface that is usually selected is an infinite plane that coincides with the aperture of the horn. When the horn is not mounted on an infinite ground plane, the fields outside the aperture are not known and an exact equivalent cannot be formed. However, the usual approximation is to assume that the fields outside the aperture are zero, as was done for the aperture of Section 12.5.2.

The fields at the aperture of the horn can be found by treating the horn as a radial waveguide [4]–[6]. The fields within the horn can be expressed in terms of cylindrical TE and TM wave functions which include Hankel functions. This method finds the fields not only at the aperture of the horn but also within the horn. The process is straightforward but laborious, and it will not be included here. However, it is assigned as an exercise at the end of the chapter (Problem 13.1).

It can be shown that if the (1) fields of the feed waveguide are those of its dominant TE_{10} mode and (2) horn length is large compared to the aperture dimensions, the lowest order mode fields at the aperture of the horn are given by

$$E_z' = E_x' = H_y' = 0 \tag{13-1a}$$

$$E_y'(x', y') \simeq E_1 \cos\left(\frac{\pi}{a}x'\right) e^{-j[ky'^2/(2\rho_1)]} \tag{13-1b}$$

$$H_z'(x', y') \simeq jE_1\left(\frac{\pi}{ka\eta}\right)\sin\left(\frac{\pi}{a}x'\right)e^{-j[ky'^2/(2\rho_1)]} \tag{13-1c}$$

$$H_x'(x', y') \simeq -\frac{E_1}{\eta}\cos\left(\frac{\pi}{a}x'\right)e^{-j[ky'^2/(2\rho_1)]} \tag{13-1d}$$

$$\rho_1 = \rho_e \cos\psi_e \tag{13-1e}$$

where E_1 is a constant. The primes are used to indicate the fields at the aperture of the horn. The expressions are similar to the fields of a TE_{10}-mode for a rectangular waveguide with aperture dimensions of a and $b_1(b_1 > a)$. The only difference is the complex exponential term which is used here to represent the quadratic phase variations of the fields over the aperture of the horn.

The necessity of the quadratic phase term in (13-1b)–(13-1d) can be illustrated geometrically. Referring to Figure 13.2(b), let us assume that at the imaginary apex of the horn (shown dashed) there exists a line source radiating cylindrical waves. As the waves travel in the outward radial direction, the constant phase fronts are cylin-

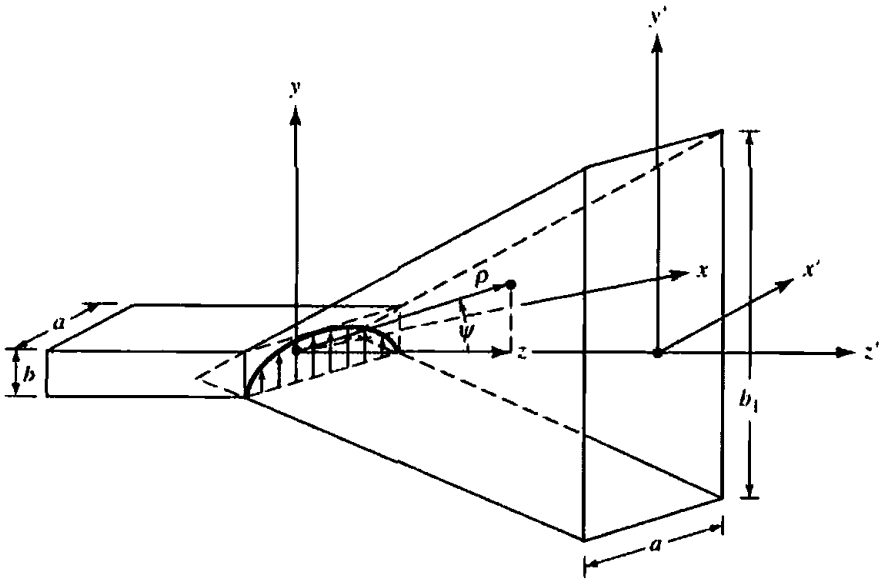

(a) E-plane horn

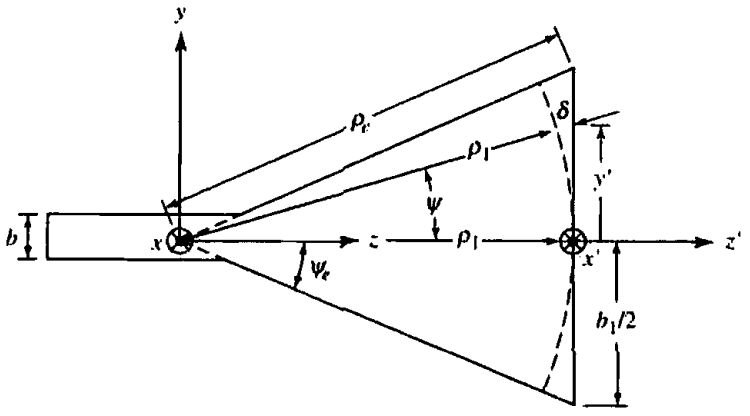

(b) E-plane view

Figure 13.2 E-plane horn and coordinate system.

drical. At any point y' at the aperture of the horn, the phase of the field will not be the same as that at the origin ($y' = 0$). The phase is different because the wave has traveled different distances from the apex to the aperture. The difference in path of travel, designated as $\delta(y')$, can be obtained by referring to Figure 13.2(b). For any point y'

$$[\rho_1 + \delta(y')]^2 = \rho_1^2 + (y')^2 \tag{13-2}$$

or

$$\delta(y') = -\rho_1 + [\rho_1^2 + (y')^2]^{1/2} = -\rho_1 + \rho_1\left[1 + \left(\frac{y'}{\rho_1}\right)^2\right]^{1/2} \tag{13-2a}$$

Using the binomial expansion and retaining only the first two terms of it, (13-2a) reduces to

$$\boxed{\delta(y') \simeq -\rho_1 + \rho_1\left[1 + \frac{1}{2}\left(\frac{y'}{\rho_1}\right)^2\right] = \frac{1}{2}\left(\frac{y'^2}{\rho_1}\right)} \tag{13-2b}$$

When (13-2b) is multiplied by the phase factor k, the result is identical to the quadratic phase term in (13-1b)–(13-1d).

The quadratic phase variation for the fields of the dominant mode at the aperture of a horn antenna has been a standard for many years, and it has been chosen because it yields in most practical cases very good results. Because of its simplicity, it leads to closed form expressions, in terms of sine and cosine Fresnel integrals, for the radiation characteristics (far-zone fields, directivity, etc.) of the horn. It has been shown recently [7] that using the more accurate expression of (13-2a) for the phase, error variations and numerical integration yield basically the same directivities as using the approximate expression of (13-2b) for large aperture horns (b_1 of Figures 13.2 or a_1 of Figure 13.10 greater than 50λ) or small peak aperture phase error ($S = \rho_e - \rho_1$ of Figure 13.2 or $T = \rho_{h_1} - \rho_2$ of Figure 13.10 less than 0.2λ). However, for intermediate aperture sizes ($5\lambda \leq b_1$ or $a_1 \leq 8\lambda$) or intermediate peak aperture phase errors ($0.2\lambda \leq S$ or $T \leq 0.6\lambda$) the more accurate expression of (13-2a) for the phase variation yields directivities which are somewhat higher (by as much as a few tenths of a decibel) than those obtained using (13-2b). Also it has been shown using a full-wave Moment Method analysis of the horn [8] that as the horn dimensions become large the amplitude distribution at the aperture of the horn contains higher order modes than the TE_{10} mode and the phase distribution at the aperture approaches the parabolic phase front.

Example 13.1

Design an E-plane sectoral horn so that the maximum phase deviation at the aperture of the horn is 56.72°. The dimensions of the horn are $a = 0.5\lambda$, $b = 0.25\lambda$, $b_1 = 2.75\lambda$.

SOLUTION

Using (13-2b)

$$\Delta\phi|_{\max} = k\delta(y')|_{y' = b_1/2} = \frac{k\,(b_1/2)^2}{2\rho_1} = 56.72\left(\frac{\pi}{180}\right)$$

or

$$\rho_1 = \left(\frac{2.75}{2}\right)^2 \frac{180}{56.72}\lambda = 6\lambda$$

The total flare angle of the horn should be equal to

$$2\psi_e = 2\tan^{-1}\left(\frac{b_1/2}{\rho_1}\right) = 2\tan^{-1}\left(\frac{2.75/2}{6}\right) = 25.81°$$

13.2.2 Radiated Fields

To find the fields radiated by the horn, only the tangential components of the **E**- and/or **H**-fields over a closed surface must be known. The closed surface is chosen to coincide with an infinite plane passing through the mouth of the horn. To solve for the fields, the approximate equivalent of Section 12.5.2 is used. That is,

$$\left.\begin{aligned} J_y &= -\frac{E_1}{\eta}\cos\left(\frac{\pi}{a}x'\right)e^{-jk\delta(y')} \\ M_x &= E_1\cos\left(\frac{\pi}{a}x'\right)e^{-jk\delta(y')} \end{aligned}\right\} \begin{aligned} &-a/2 \le x' \le a/2 \\ &-b_1/2 \le y' \le b_1/2 \end{aligned} \tag{13-3}$$

and

$$\mathbf{J}_s = \mathbf{M}_s = 0 \qquad \text{elsewhere} \tag{13-3a}$$

Using (12-12a)

$$N_\theta = -\frac{E_1}{\eta}\cos\theta\sin\phi\, I_1 I_2 \tag{13-4}$$

where

$$\begin{aligned} I_1 &= \int_{-a/2}^{+a/2}\cos\left(\frac{\pi}{a}x'\right)e^{jkx'\sin\theta\cos\phi}\,dx' \\ &= -\left(\frac{\pi a}{2}\right)\left[\frac{\cos\left(\dfrac{ka}{2}\sin\theta\cos\phi\right)}{\left(\dfrac{ka}{2}\sin\theta\cos\phi\right)^2 - \left(\dfrac{\pi}{2}\right)^2}\right] \end{aligned} \tag{13-4a}$$

$$I_2 = \int_{-b_1/2}^{+b_1/2} e^{-jk[\delta(y')-y'\sin\theta\sin\phi]}\,dy' \tag{13-4b}$$

The integral of (13-4b) can also be evaluated in terms of cosine and sine Fresnel integrals. To do this, I_2 can be written, by completing the square, as

$$\begin{aligned} I_2 &= \int_{-b_1/2}^{+b_1/2} e^{-j[ky'^2/(2\rho_1) - k_y y']}\,dy' \\ &= e^{j(k_y^2\rho_1/2k)}\int_{-b_1/2}^{+b_1/2} e^{-j[(ky' - k_y\rho_1)^2/2k\rho_1]}\,dy' \end{aligned} \tag{13-5}$$

where

$$k_y = k \sin\theta \sin\phi \tag{13-5a}$$

Making a change of variable

$$\sqrt{\frac{\pi}{2}}\, t = \sqrt{\frac{1}{2k\rho_1}}\,(ky' - k_y\rho_1) \tag{13-6a}$$

$$t = \sqrt{\frac{1}{\pi k\rho_1}}\,(ky' - k_y\rho_1) \tag{13-6b}$$

$$dt = \sqrt{\frac{k}{\pi\rho_1}}\, dy' \tag{13-6c}$$

reduces (13-5) to

$$\begin{aligned} I_2 &= \sqrt{\frac{\pi\rho_1}{k}}\, e^{j(k_x^2\rho_1/2k)} \int_{t_1}^{t_2} e^{-j(\pi/2)t^2}\, dt \\ &= \sqrt{\frac{\pi\rho_1}{k}}\, e^{j(k_x^2\rho_1/2k)} \int_{t_1}^{t_2} \left[\cos\left(\frac{\pi}{2}t^2\right) - j\sin\left(\frac{\pi}{2}t^2\right)\right] dt \end{aligned} \tag{13-7}$$

and takes the form of

$$I_2 = \sqrt{\frac{\pi\rho_1}{k}}\, e^{j(k_x^2\rho_1/2k)}\{[C(t_2) - C(t_1)] - j[S(t_2) - S(t_1)]\} \tag{13-8}$$

where

$$\boxed{t_1 = \sqrt{\frac{1}{\pi k\rho_1}}\left(-\frac{kb_1}{2} - k_y\rho_1\right)} \tag{13-8a}$$

$$\boxed{t_2 = \sqrt{\frac{1}{\pi k\rho_1}}\left(\frac{kb_1}{2} - k_y\rho_1\right)} \tag{13-8b}$$

$$C(x) = \int_0^x \cos\left(\frac{\pi}{2}t^2\right) dt \tag{13-8c}$$

$$S(x) = \int_0^x \sin\left(\frac{\pi}{2}t^2\right) dt \tag{13-8d}$$

$C(x)$ and $S(x)$ are known as the cosine and sine Fresnel integrals and are well tabulated [9] (see Appendix IV). Computer subroutines are also available for efficient numerical evaluation of each [10], [11].

Using (13-4a) and (13-8), (13-4) can be written as

$$N_\theta = E_1 \frac{\pi a}{2} \sqrt{\frac{\pi\rho_1}{k}}\, e^{j(k_x^2\rho_1/2k)} \times \left\{ \frac{\cos\theta\sin\phi}{\eta} \left[\frac{\cos\left(\frac{k_x a}{2}\right)}{\left(\frac{k_x a}{2}\right)^2 - \left(\frac{\pi}{2}\right)^2} \right] F(t_1, t_2) \right\} \tag{13-9}$$

where

$$\boxed{k_x = k \sin\theta \cos\phi} \tag{13-9a}$$

$$\boxed{k_y = k \sin\theta \sin\phi} \tag{13-9b}$$

$$\boxed{F(t_1, t_2) = [C(t_2) - C(t_1)] - j[S(t_2) - S(t_1)]} \tag{13-9c}$$

In a similar manner, N_ϕ, L_θ, L_ϕ of (12-12b)–(12-12d) reduce to

$$N_\phi = E_1 \frac{\pi a}{2} \sqrt{\frac{\pi\rho_1}{k}} e^{j(k_x^2\rho_1/2k)} \left\{ \frac{\cos\phi}{\eta} \left[\frac{\cos\left(\frac{k_x a}{2}\right)}{\left(\frac{k_x a}{2}\right)^2 - \left(\frac{\pi}{2}\right)^2} \right] F(t_1, t_2) \right\} \tag{13-10a}$$

$$L_\theta = E_1 \frac{\pi a}{2} \sqrt{\frac{\pi\rho_1}{k}} e^{j(k_x^2\rho_1/2k)} \times \left\{ -\cos\theta\cos\phi \left[\frac{\cos\left(\frac{k_x a}{2}\right)}{\left(\frac{k_x a}{2}\right)^2 - \left(\frac{\pi}{2}\right)^2} \right] F(t_1, t_2) \right\} \tag{13-10b}$$

$$L_\phi = E_1 \frac{\pi a}{2} \sqrt{\frac{\pi\rho_1}{k}} e^{j(k_x^2\rho_1/2k)} \left\{ \sin\phi \left[\frac{\cos\left(\frac{k_x a}{2}\right)}{\left(\frac{k_x a}{2}\right)^2 - \left(\frac{\pi}{2}\right)^2} \right] F(t_1, t_2) \right\} \tag{13-10c}$$

The electric field components radiated by the horn can be obtained by using (12-10a)–(12-10c), and (13-9)–(13-10c). Thus,

$$\boxed{E_r = 0} \tag{13-11a}$$

$$\boxed{\begin{aligned} E_\theta &= -j \frac{a\sqrt{\pi k\rho_1}\, E_1 e^{-jkr}}{8r} \\ &\times \left\{ e^{j(k_x^2\rho_1/2k)} \sin\phi(1 + \cos\theta) \left[\frac{\cos\left(\frac{k_x a}{2}\right)}{\left(\frac{k_x a}{2}\right)^2 - \left(\frac{\pi}{2}\right)^2} \right] F(t_1, t_2) \right\} \end{aligned}} \tag{13-11b}$$

$$\boxed{\begin{aligned} E_\phi &= -j \frac{a\sqrt{\pi k\rho_1}\, E_1 e^{-jkr}}{8r} \\ &\times \left\{ e^{j(k_x^2\rho_1/2k)} \cos\phi(\cos\theta + 1) \left[\frac{\cos\left(\frac{k_x a}{2}\right)}{\left(\frac{k_x a}{2}\right)^2 - \left(\frac{\pi}{2}\right)^2} \right] F(t_1, t_2) \right\} \end{aligned}} \tag{13-11c}$$

where t_1, t_2, k_x, k_y, and $F(t_1, t_2)$ are given, respectively, by (13-8a), (13-8b), (13-9a), (13-9b), and (13-9c). The corresponding **H**-field components are obtained using (12-10d)–(12-10f).

In the principal E- and H-planes, the electric field reduces to

E-Plane ($\phi = \pi/2$)

$$E_r = E_\phi = 0 \tag{13-12a}$$

$$E_\theta = -j\frac{a\sqrt{\pi k\rho_1}E_1 e^{-jkr}}{8r}\left\{-e^{j(k\rho_1 \sin^2\theta/2)}\left(\frac{2}{\pi}\right)^2(1 + \cos\theta)F(t_1', t_2')\right\} \tag{13-12b}$$

$$t_1' = \sqrt{\frac{k}{\pi\rho_1}}\left(-\frac{b_1}{2} - \rho_1 \sin\theta\right) \tag{13-12c}$$

$$t_2' = \sqrt{\frac{k}{\pi\rho_1}}\left(+\frac{b_1}{2} - \rho_1 \sin\theta\right) \tag{13-12d}$$

H-Plane ($\phi = 0$)

$$E_r = E_\theta = 0 \tag{13-13a}$$

$$E_\phi = -j\frac{a\sqrt{\pi k\rho_1}E_1 e^{-jkr}}{8r}\left\{(1 + \cos\theta)\left[\frac{\cos\left(\frac{ka}{2}\sin\theta\right)}{\left(\frac{ka}{2}\sin\theta\right)^2 - \left(\frac{\pi}{2}\right)^2}\right]F(t_1'', t_2'')\right\} \tag{13-13b}$$

$$t_1'' = -\frac{b_1}{2}\sqrt{\frac{k}{\pi\rho_1}} \tag{13-13c}$$

$$t_2'' = +\frac{b_1}{2}\sqrt{\frac{k}{\pi\rho_1}} \tag{13-13d}$$

To better understand the performance of an E-plane sectoral horn and gain some insight into its performance as an efficient radiator, a three-dimensional normalized field pattern has been plotted in Figure 13.3 utilizing (13-11a)–(13-11c). As expected, the E-plane pattern is much narrower than the H-plane because of the flaring and larger dimensions of the horn in that direction. Figure 13.3 provides an excellent visual view of the overall radiation performance of the horn. To display additional details, the corresponding normalized E- and H-plane patterns (in dB) are illustrated in Figure 13.4. These patterns also illustrate the narrowness of the E-plane and provide information on the relative levels of the pattern in those two planes.

To examine the behavior of the pattern as a function of flaring, the E-plane patterns for a horn antenna with $\rho_1 = 15\lambda$ and with flare angles of $20° \le 2\psi_e \le 35°$ are plotted in Figure 13.5. A total of four patterns is illustrated. Since each pattern is *symmetrical, only half of each pattern is displayed. For small included angles,* the pattern becomes narrower as the flare increases. Eventually the pattern begins to widen, becomes flatter around the main lobe, and the phase tapering at the aperture is such that even the main maximum does not occur on axis. This is illustrated in Figure 13.5 by the pattern with $2\psi_e = 35°$. As the flaring is extended beyond that point, the flatness (with certain allowable ripple) increases and eventually the main

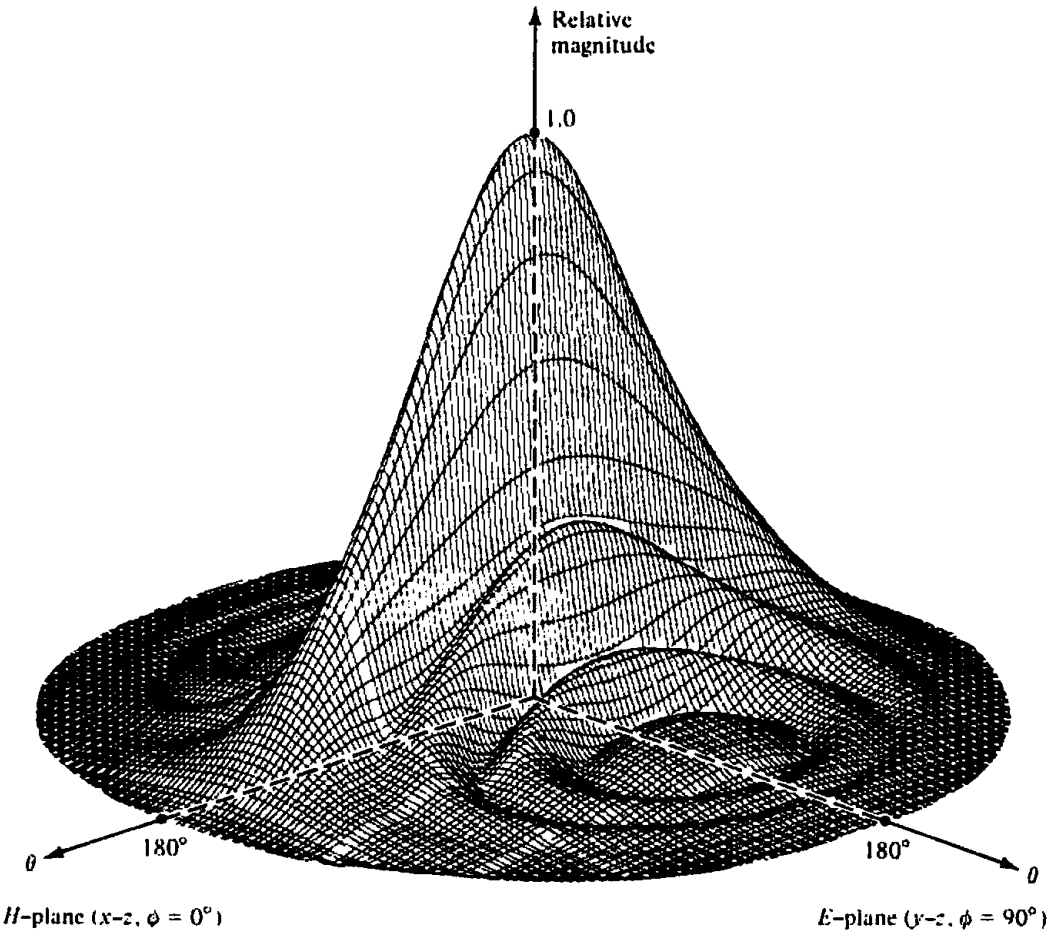

Figure 13.3 Three-dimensional field pattern of *E*-plane sectoral horn ($\rho_1 = 6\lambda$, $b_1 = 2.75\lambda$, $a = 0.5\lambda$).

maximum returns again on axis. It is also observed that as the flaring increases, the pattern exhibits much sharper cutoff characteristics. In practice, to compensate for the phase taper at the opening, a lens is usually placed at the aperture making the pattern of the horn always narrower as its flare increases.

Similar pattern variations occur as the length of the horn is varied while the flare angle is held constant. As the length increases, the pattern begins to broaden and eventually becomes flatter (with a ripple). Beyond a certain length, the main maximum does not even occur on axis, and the pattern continues to broaden and to become flatter (within an allowable ripple) until the maximum returns on axis. The process continues indefinitely.

An observation of the *E*-plane pattern, as given by (13-12a)–(13-12d), indicates that the *magnitude of the normalized pattern, excluding the factor* $(1 + \cos\theta)$, can be written as

$$E_{\theta n} = F(t_1', t_2') = [C(t_2') - C(t_1')] - j[S(t_2') - S(t_1')] \tag{13-14a}$$

$$\begin{aligned} t_1' &= \sqrt{\frac{k}{\pi\rho_1}}\left(-\frac{b_1}{2} - \rho_1 \sin\theta\right) \\ &= 2\sqrt{\frac{b_1^2}{8\lambda\rho_1}}\left[-1 - \frac{1}{4}\left(\frac{8\rho_1\lambda}{b_1^2}\right)\left(\frac{b_1}{\lambda}\sin\theta\right)\right] \\ &= 2\sqrt{s}\left[-1 - \frac{1}{4}\left(\frac{1}{s}\right)\left(\frac{b_1}{\lambda}\sin\theta\right)\right] \end{aligned} \tag{13-14b}$$

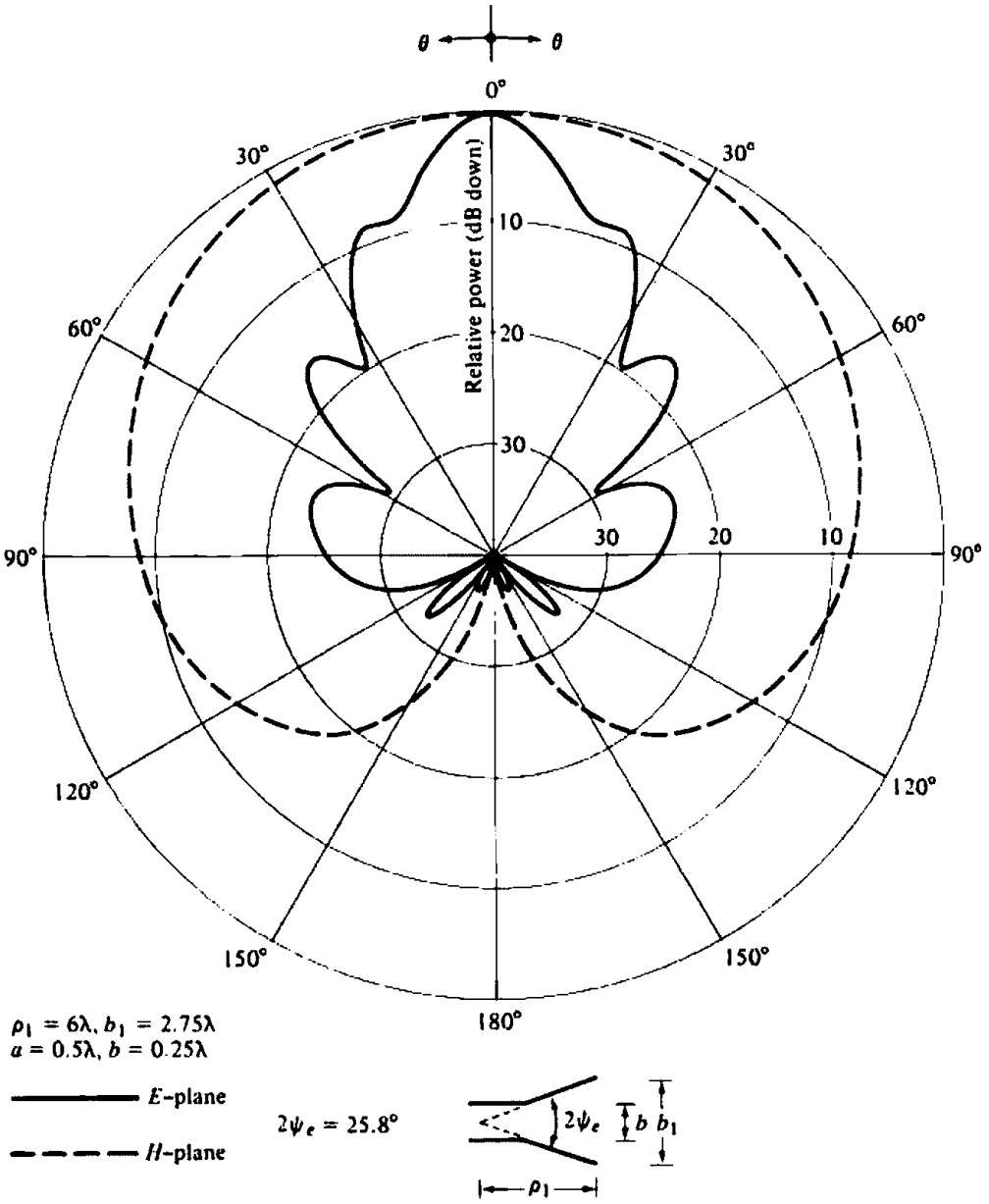

Figure 13.4 *E*- and *H*-plane patterns of an *E*-plane sectoral horn.

$$t_2' = \sqrt{\frac{k}{\pi\rho_1}}\left(\frac{b_1}{2} - \rho_1 \sin\theta\right)$$

$$= 2\sqrt{\frac{{b_1}^2}{8\lambda\rho_1}}\left[1 - \frac{1}{4}\left(\frac{8\rho_1\lambda}{{b_1}^2}\right)\left(\frac{b_1}{\lambda}\sin\theta\right)\right]$$

$$= 2\sqrt{s}\left[1 - \frac{1}{4}\left(\frac{1}{s}\right)\left(\frac{b_1}{\lambda}\sin\theta\right)\right] \tag{13-14c}$$

$$s = \frac{{b_1}^2}{8\lambda\rho_1} \tag{13-14d}$$

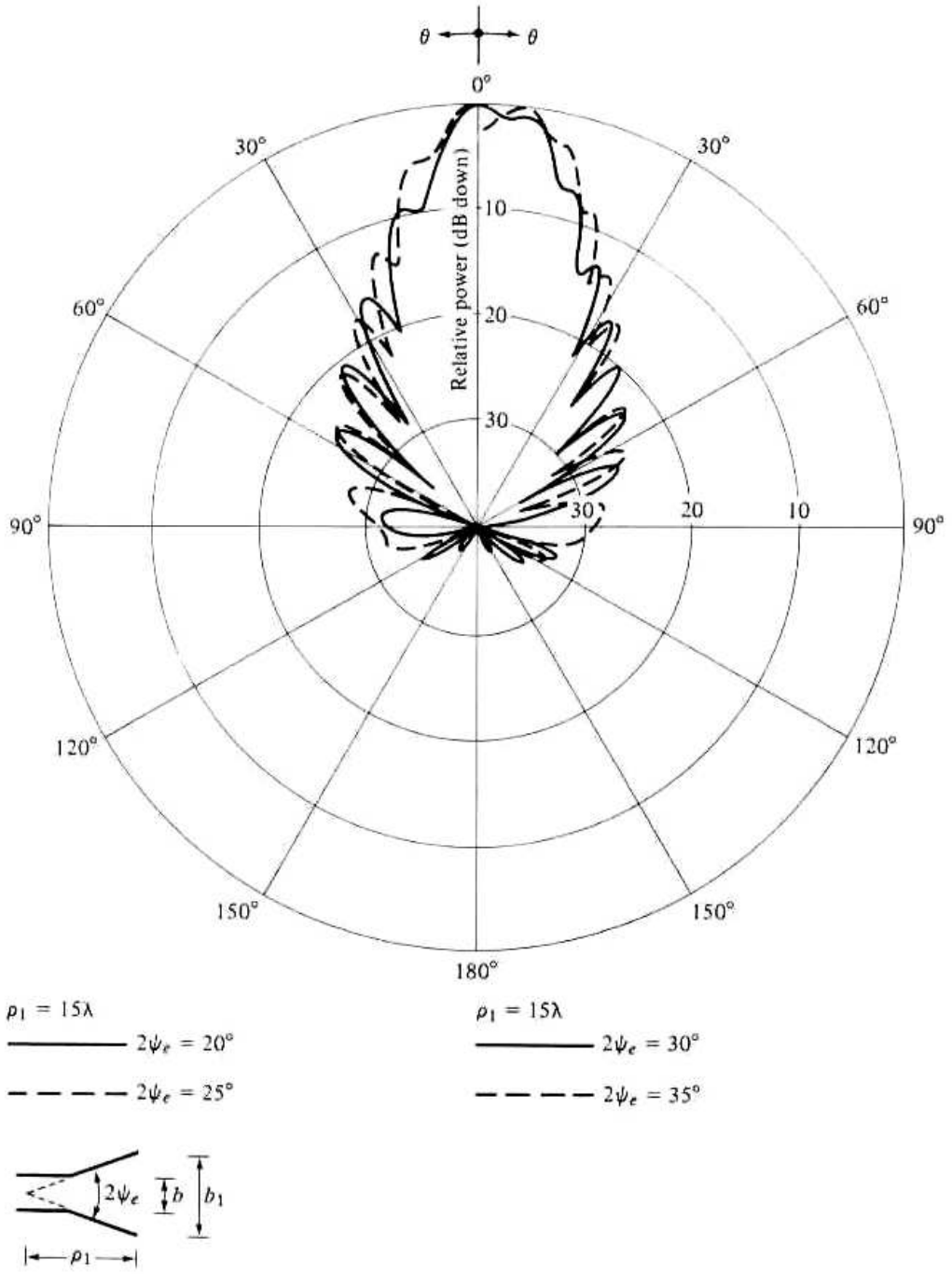

Figure 13.5 *E*-plane patterns of *E*-plane sectoral horn for constant length and different included angles.

For a given value of s, the field of (13-14a) can be plotted as a function of $b_1/\lambda \sin\theta$, as shown in Figure 13.6 for $s = \frac{1}{64}, \frac{1}{8}, \frac{1}{4}, \frac{1}{2}, \frac{3}{4}$, and 1. These plots are usually referred to as *universal curves*, because from them the normalized *E*-plane pattern of any *E*-plane sectoral horn can be obtained. This is accomplished by first determining the value of s from a given b_1 and ρ_1 by using (13-14d). For that value of s, the field strength (in dB) as a function of $(b_1/\lambda)\sin\theta$ (or as a function of θ for a given b_1) is obtained from Figure 13.6. Finally the value of $(1 + \cos\theta)$, normalized to 0 dB and written as $20 \log_{10}[(1 + \cos\theta)/2]$, is added to that number to arrive at the required field strength.

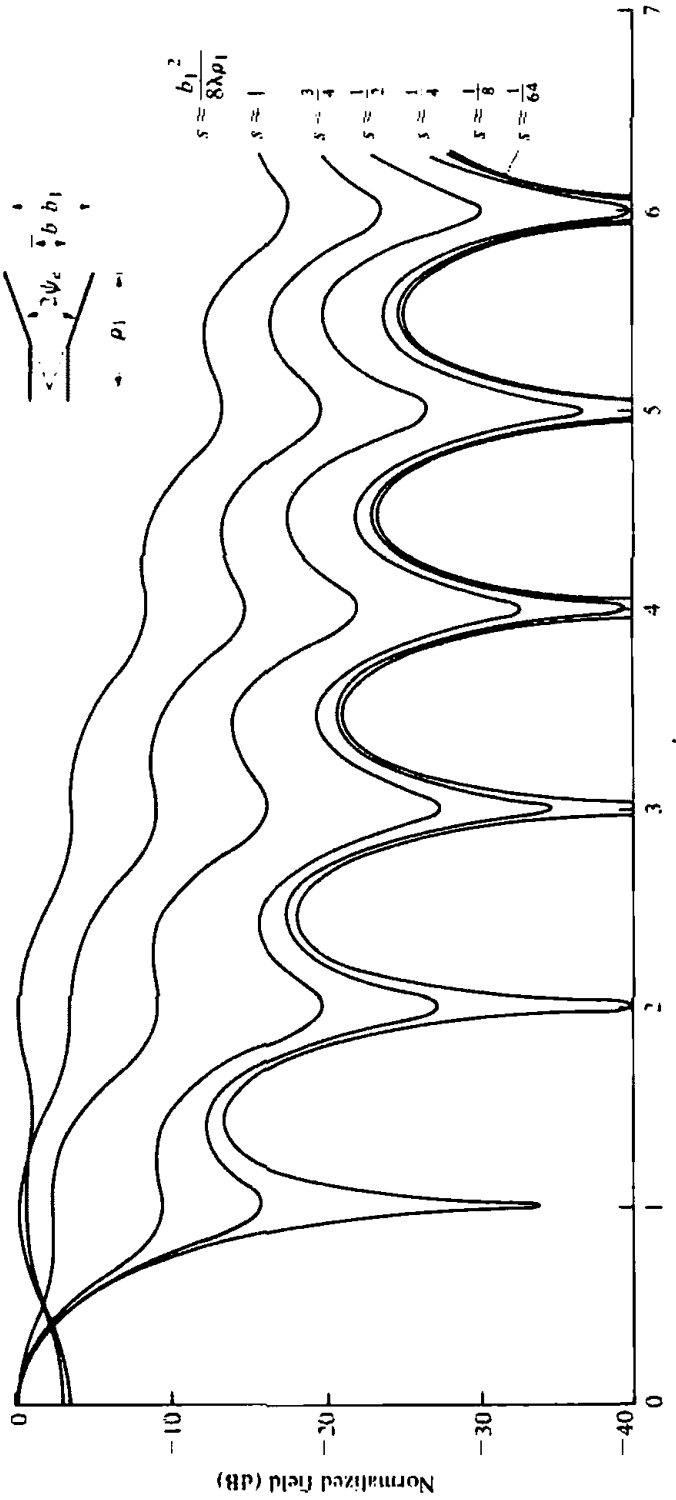

Figure 13.6 *E*-plane universal patterns for *E*-plane sectoral and pyramidal horns.

Example 13.2

An *E*-plane horn has dimensions of $a = 0.5\lambda$, $b = 0.25\lambda$, $b_1 = 2.75\lambda$, and $\rho_1 = 6\lambda$. Find its *E*-plane normalized field intensity (in dB *and* as a voltage ratio) at an angle of $\theta = 90°$ using the universal curves of Figure 13.6.

SOLUTION

Using (13-14d)

$$s = \frac{b_1^2}{8\lambda\rho_1} = \frac{(2.75)^2}{8(6)} \simeq 0.1575 \simeq \frac{1}{6.3}$$

None of the curves in Figure 13.6 represents $s = \frac{1}{6.3}$. Therefore interpolation will be used between the $s = \frac{1}{4}$ and $s = \frac{1}{8}$ curves.

At $\theta = 90°$

$$\frac{b_1}{\lambda} \sin(\theta) = 2.75 \sin(90°) = 2.75$$

and at that point the field intensity between the $s = \frac{1}{4}$ and $s = \frac{1}{8}$ curves is about -20 dB. Therefore the total field intensity at $\theta = 90°$ is equal to

$$E_\theta = -20 + 20 \log_{10}\left(\frac{1 + \cos 90°}{2}\right) = -20 - 6 = -26 \text{ dB}$$

or as a normalized voltage ratio of

$$E_\theta = 0.05$$

which closely agrees with the results of Figure 13.4.

13.2.3 Directivity

The directivity is one of the parameters that is often used as a figure-of-merit to describe the performance of an antenna. To find the directivity, the maximum radiation is formed. That is,

$$U_{\max} = U(\theta, \phi)|_{\max} = \frac{r^2}{2\eta} |\mathbf{E}|^2_{\max} \tag{13-15}$$

For most horn antennas $|\mathbf{E}|_{\max}$ is directed nearly along the z-axis ($\theta = 0°$). Thus,

$$|\mathbf{E}|_{\max} = \sqrt{|E_\theta|^2_{\max} + |E_\phi|^2_{\max}} = \frac{2a\sqrt{\pi k\rho_1}}{\pi^2 r} |E_1||F(t)| \tag{13-16}$$

Using (13-11b), (13-11c), and (13-9c)

$$|E_\theta|_{\max} = \frac{2a\sqrt{\pi k\rho_1}}{\pi^2 r} |E_1 \sin\phi\, F(t)| \tag{13-16a}$$

$$|E_\phi|_{\max} = \frac{2a\sqrt{\pi k\rho_1}}{\pi^2 r} |E_1 \cos\phi\, F(t)| \tag{13-16b}$$

$$F(t) = [C(t) - jS(t)] \tag{13-16c}$$

$$t = \frac{b_1}{2}\sqrt{\frac{k}{\pi\rho_1}} = \frac{b_1}{\sqrt{2\lambda\rho_1}} \tag{13-16d}$$

since

$$k_x = k_y = 0 \tag{13-16e}$$

$$t_1 = -t = -\frac{b_1}{2}\sqrt{\frac{k}{\pi\rho_1}} = -\frac{b_1}{\sqrt{2\lambda\rho_1}} \tag{13-16f}$$

$$t_2 = +t = +\frac{b_1}{2}\sqrt{\frac{k}{\pi\rho_1}} = \frac{b_1}{\sqrt{2\lambda\rho_1}} \tag{13-16g}$$

$$C(-t) = -C(t) \tag{13-16h}$$

$$S(-t) = -S(t) \tag{13-16i}$$

Thus

$$U_{\max} = \frac{r^2}{2\eta}|\mathbf{E}|^2_{\max} = \frac{2a^2k\rho_1}{\eta\pi^3}|E_1|^2|F(t)|^2$$

$$= \frac{4a^2\rho_1|E_1|^2}{\eta\lambda\pi^2}|F(t)|^2 \tag{13-17}$$

where

$$|F(t)|^2 = \left[C^2\left(\frac{b_1}{\sqrt{2\lambda\rho_1}}\right) + S^2\left(\frac{b_1}{\sqrt{2\lambda\rho_1}}\right)\right] \tag{13-17a}$$

The total power radiated can be found by simply integrating the average power density over the aperture of the horn. Using (13-1a)–(13-1d)

$$P_{\text{rad}} = \frac{1}{2}\iint_{S_0}\text{Re}(\mathbf{E}' \times \mathbf{H}'^*)\cdot d\mathbf{s} = \frac{1}{2\eta}\int_{-b_1/2}^{+b_1/2}\int_{-a/2}^{+a/2}|E_1|^2\cos^2\left(\frac{\pi}{a}x'\right)dx'\,dy' \tag{13-18}$$

which reduces to

$$P_{\text{rad}} = |E_1|^2\frac{b_1a}{4\eta} \tag{13-18a}$$

Using (13-17) and (13-18a), the directivity for the E-plane horn can be written as

$$\boxed{\begin{aligned} D_E &= \frac{4\pi U_{\max}}{P_{\text{rad}}} = \frac{64a\rho_1}{\pi\lambda b_1}|F(t)|^2 \\ &= \frac{64a\rho_1}{\pi\lambda b_1}\left[C^2\left(\frac{b_1}{\sqrt{2\lambda\rho_1}}\right) + S^2\left(\frac{b_1}{\sqrt{2\lambda\rho_1}}\right)\right] \end{aligned}} \tag{13-19}$$

The overall performance of an antenna system can often be judged by its beamwidth and/or its directivity. The half-power beamwidth (HPBW), as a function of flare angle, for different horn lengths is shown in Figure 13.7. In addition, the directivity (normalized with respect to the constant aperture dimension a) is displayed in Figure 13.8. For a given length, the horn exhibits a monotonic decrease in half-power beam-

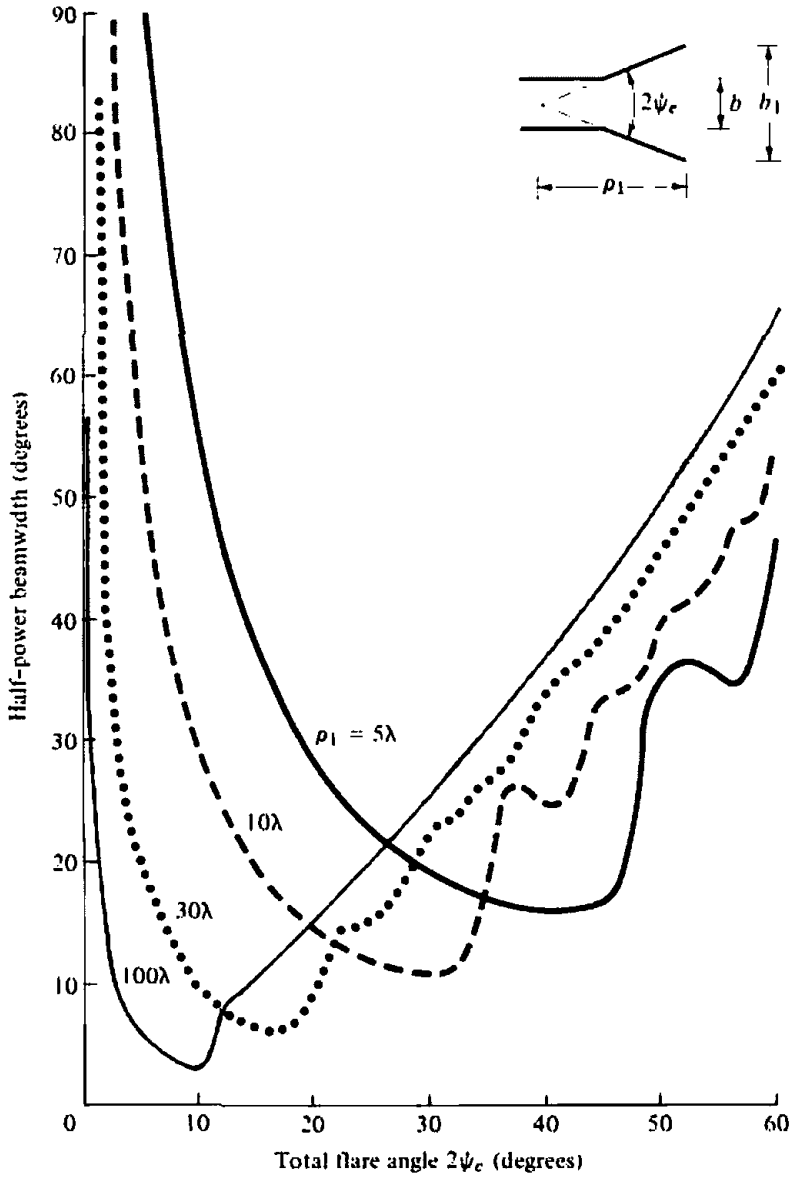

Figure 13.7 Half-power beamwidth of *E*-plane sectoral horn as a function of included angle and for different lengths.

width and an increase in directivity up to a certain flare. Beyond that point a monotonic increase in beamwidth and decrease in directivity is indicated followed by rises and falls. The increase in beamwidth and decrease in directivity beyond a certain flare indicate the broadening of the main beam.

If the values of b_1 (in λ), which correspond to the maximum directivities in Figure 13.8, are plotted versus their corresponding values of ρ_1 (in λ), it can be shown that each optimum directivity occurs when

$$\boxed{b_1 \simeq \sqrt{2\lambda\rho_1}} \tag{13-19a}$$

with a corresponding value of s equal to

$$\boxed{s|_{b_1 = \sqrt{2\lambda\rho_1}} = s_{op} = \frac{b_1^2}{8\lambda\rho_1}\bigg|_{b_1 = \sqrt{2\lambda\rho_1}} = \frac{1}{4}} \tag{13-19b}$$

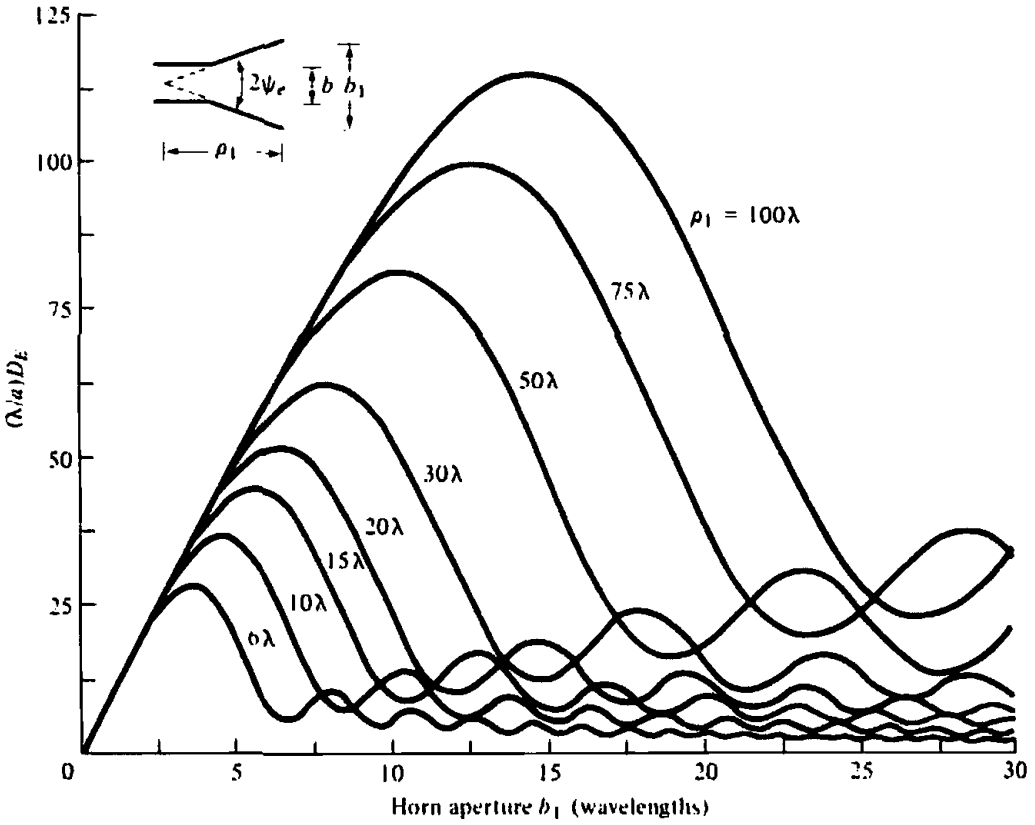

Figure 13.8 Normalized directivity of E-plane sectoral horn as a function of aperture size and for different lengths.

The classic expression of (13-19) for the directivity of an E-plane horn has been the standard for many years. However, it has been shown that this expression may not always yield very accurate values for the on-axis directivity. A more accurate expression for the maximum on-axis directivity based on an exact open-ended parallel-plate waveguide analysis has been derived, and it yields a modification to the on-axis value of (13-19), which provides sufficient accuracy for most designs [12], [13]. Using (13-19a), the modified formula for the on-axis value of (13-19) can be written as [12], [13]

$$D_E(\max) = \frac{16ab_1}{\lambda^2(1 + \lambda_g/\lambda)}\left[C^2\left(\frac{b_1}{\sqrt{2\lambda\rho_1}}\right) + S^2\left(\frac{b_1}{\sqrt{2\lambda\rho_1}}\right)\right]e^{\frac{\pi a}{\lambda}\left(1 - \frac{\lambda}{\lambda_g}\right)} \tag{13-19c}$$

where λ_g is the guide wavelength in the feed waveguide for the dominant TE_{10} mode. Predicted values based on (13-19) and (13-19c) have been compared with measurements and it was found that (13-19c) yielded results which were closer to the measured values [12].

The directivity of an E-plane sectoral horn can also be computed by using the following procedure [14].

1. Calculate B by

$$B = \frac{b_1}{\lambda}\sqrt{\frac{50}{\rho_e/\lambda}} \tag{13-20a}$$

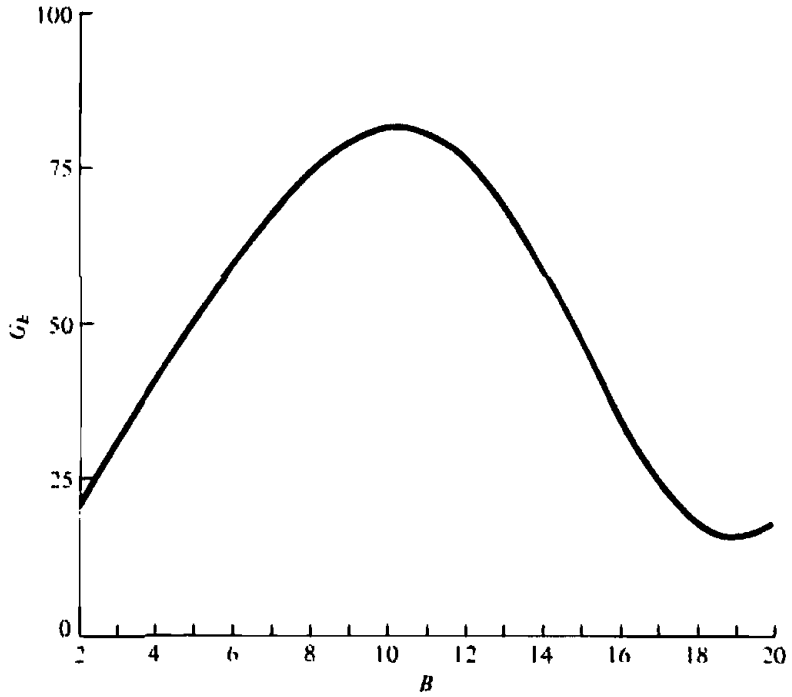

Figure 13.9 G_E as a function of B. (SOURCE: Adopted from data by E. H. Braun, "Some Data for the Design of Electromagnetic Horns," *IRE Trans. Antennas Propagat.*, Vol. AP-4, No. 1, January 1956. © (1956) IEEE)

2. Using this value of B, find the corresponding value of G_E from Figure 13.9. If, however, the value of B is smaller than 2, compute G_E using

$$G_E = \frac{32}{\pi} B \tag{13-20b}$$

3. Calculate D_E by using the value of G_E from Figure 13.9 or from (13-20b). Thus

$$\boxed{D_E = \frac{a}{\lambda} \frac{G_E}{\sqrt{\dfrac{50}{\rho_1/\lambda}}}} \tag{13-20c}$$

Example 13.3

An E-plane sectoral horn has dimensions of $a = 0.5\lambda$, $b = 0.25\lambda$, $b_1 = 2.75\lambda$, and $\rho_1 = 6\lambda$. Compute the directivity using (13-19) and (13-20c). Compare the answers.

SOLUTION

For this horn

$$\frac{b_1}{\sqrt{2\lambda\rho_1}} = \frac{2.75}{\sqrt{2(6)}} = 0.794$$

Therefore (from Appendix IV)

$$|C(0.794)|^2 = (0.72)^2 = 0.518$$
$$|S(0.794)|^2 = (0.24)^2 = 0.0576$$

Using (13-19)

$$D_E = \frac{64(0.5)6}{2.75\pi}(0.518 + 0.0576) = 12.79 = 11.07 \text{ dB}$$

To compute the directivity using (13-20c), the following parameters are evaluated:

$$\rho_e = \lambda\sqrt{(6)^2 + \left(\frac{2.75}{2}\right)^2} = 6.1555\lambda$$

$$\sqrt{\frac{50}{\rho_e/\lambda}} = \sqrt{\frac{50}{6.1555}} = 2.85$$

$$B = 2.75(2.85) = 7.84$$

For $B = 7.84$, $G_E = 73.5$ from Figure 13.9. Thus, using (13-20c)

$$D_E = \frac{0.5(73.5)}{2.85} = 12.89 = 11.10 \text{ dB}$$

Obviously an excellent agreement between the results of (13-19) and (13-20c).

13.3 *H*-PLANE SECTORAL HORN

Flaring the dimensions of a rectangular waveguide in the direction of the **H**-field, while keeping the other constant, forms an *H*-plane sectoral horn shown in Figure 13.1(b). A more detailed geometry is shown in Figure 13.10.

The analysis procedure for this horn is similar to that for the *E*-plane horn, which was outlined in the previous section. Instead of including all the details of the formulation, a summary of each radiation characteristic will be given.

13.3.1 Aperture Fields

The fields at the aperture of the horn can be found by treating the horn as a radial waveguide forming an imaginary apex shown dashed in Figure 13.10. Using this method, it can be shown that at the aperture of the horn

$$E_x' = H_y' = 0 \tag{13-21a}$$

$$E_y'(x') = E_2 \cos\left(\frac{\pi}{a_1}x'\right) e^{-jk\delta(x')} \tag{13-21b}$$

$$H_x'(x') = -\frac{E_2}{\eta}\cos\left(\frac{\pi}{a_1}x'\right) e^{-jk\delta(x')} \tag{13-21c}$$

$$\delta(x') = \frac{1}{2}\left(\frac{x'^2}{\rho_2}\right) \tag{13-21d}$$

$$\rho_2 = \rho_h \cos\psi_h \tag{13-21e}$$

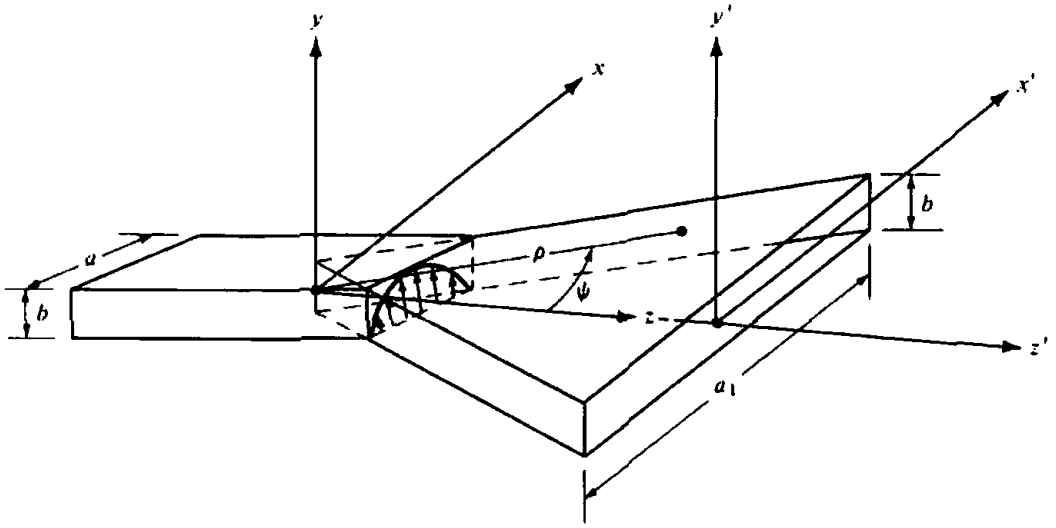

(a) *H*-plane sectoral horn

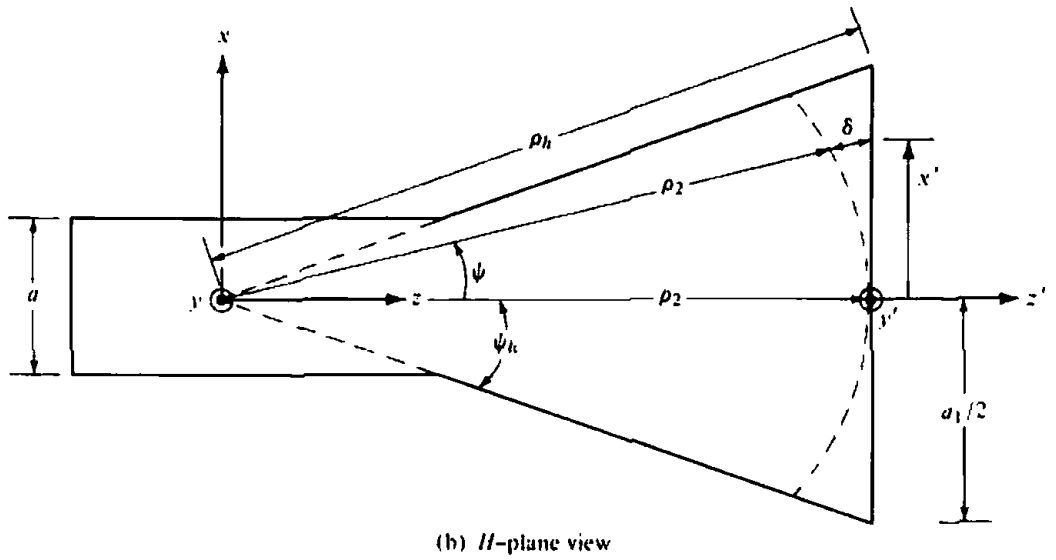

(b) *H*-plane view

Figure 13.10 *H*-plane sectoral horn and coordinate system.

13.3.2 Radiated Fields

The fields radiated by the horn can be found by first formulating the equivalent current densities $\mathbf{J}_s$ and $\mathbf{M}_s$. Using (13-21a)–(13-21c), it can be shown that over the aperture of the horn

$$J_x = J_z = M_y = M_z = 0 \tag{13-22a}$$

$$J_y = -\frac{E_2}{\eta}\cos\left(\frac{\pi}{a_1}x'\right)e^{-jk\delta(x')} \tag{13-22b}$$

$$M_x = E_2\cos\left(\frac{\pi}{a_1}x'\right)e^{-jk\delta(x')} \tag{13-22c}$$

and they are assumed to be zero elsewhere. Thus (12-12a) can be expressed as

$$N_\theta = \iint_S J_y\cos\theta\cos\phi\, e^{+jkr'\cos\psi}\,ds' = -\frac{E_2}{\eta}\cos\theta\sin\phi\, I_1 I_2 \tag{13-23}$$

where

$$I_1 = \int_{-b/2}^{+b/2} e^{+jky' \sin\theta\sin\phi}\, dy' = b\left[\frac{\sin\left(\frac{kb}{2}\sin\theta\sin\phi\right)}{\frac{kb}{2}\sin\theta\sin\phi}\right] \tag{13-23a}$$

$$I_2 = \int_{-a_1/2}^{+a_1/2} \cos\left(\frac{\pi}{a_1}x'\right) e^{-jk[\delta(x')-x'\sin\theta\cos\phi]}\, dx' \tag{13-23b}$$

By rewriting $\cos[(\pi/a_1)x']$ as

$$\cos\left(\frac{\pi}{a_1}x'\right) = \left[\frac{e^{j(\pi/a_1)x'} + e^{-j(\pi/a_1)x'}}{2}\right] \tag{13-24}$$

(13-23b) can be expressed as

$$I_2 = I_2' + I_2'' \tag{13-25}$$

where

$$I_2' = \frac{1}{2}\sqrt{\frac{\pi\rho_2}{k}}\, e^{j(k_x'^2\rho_2/2k)}\{[C(t_2') - C(t_1')] - j[S(t_2') - S(t_1')]\} \tag{13-26}$$

$$\boxed{t_1' = \sqrt{\frac{1}{\pi k\rho_2}}\left(-\frac{ka_1}{2} - k_x'\rho_2\right)} \tag{13-26a}$$

$$\boxed{t_2' = \sqrt{\frac{1}{\pi k\rho_2}}\left(+\frac{ka_1}{2} - k_x'\rho_2\right)} \tag{13-26b}$$

$$\boxed{k_x' = k\sin\theta\cos\phi + \frac{\pi}{a_1}} \tag{13-26c}$$

$$I_2'' = \frac{1}{2}\sqrt{\frac{\pi\rho_2}{k}}\, e^{j(k_x''^2\rho_2/2k)}\{[C(t_2'') - C(t_1'')] - j[S(t_2'') - S(t_1'')]\} \tag{13-27}$$

$$\boxed{t_1'' = \sqrt{\frac{1}{\pi k\rho_2}}\left(-\frac{ka_1}{2} - k_x''\rho_2\right)} \tag{13-27a}$$

$$\boxed{t_2'' = \sqrt{\frac{1}{\pi k\rho_2}}\left(+\frac{ka_1}{2} - k_x''\rho_2\right)} \tag{13-27b}$$

$$\boxed{k_x'' = k\sin\theta\cos\phi - \frac{\pi}{a_1}} \tag{13-27c}$$

$C(x)$ and $S(x)$ are the cosine and sine Fresnel integrals of (13-8c) and (13-8d), and they are well tabulated (see Appendix IV).

With the aid of (13-23a), (13-25), (13-26), and (13-27), (13-23) reduces to

$$N_\theta = -E_2 \frac{b}{2}\sqrt{\frac{\pi\rho_2}{k}} \times \left\{\frac{\cos\theta\sin\phi}{\eta}\frac{\sin Y}{Y}\left[e^{jf_1}F(t_1', t_2') + e^{jf_2}F(t_1'', t_2'')\right]\right\} \tag{13-28}$$

$$\boxed{F(t_1, t_2) = [C(t_2) - C(t_1)] - j[S(t_2) - S(t_1)]} \tag{13-28a}$$

$$\boxed{f_1 = \frac{k_x'^2\rho_2}{2k}} \tag{13-28b}$$

$$\boxed{f_2 = \frac{k_x''^2\rho_2}{2k}} \tag{13-28c}$$

$$\boxed{Y = \frac{kb}{2}\sin\theta\sin\phi} \tag{13-28d}$$

In a similar manner, N_ϕ, L_θ, and L_ϕ of (12-12b)–(12-12d) can be written as

$$N_\phi = -E_2 \frac{b}{2}\sqrt{\frac{\pi\rho_2}{k}} \times \left\{\frac{\cos\phi}{\eta}\frac{\sin Y}{Y}\left[e^{jf_1}F(t_1', t_2') + e^{jf_2}F(t_1'', t_2'')\right]\right\} \tag{13-29a}$$

$$L_\theta = E_2 \frac{b}{2}\sqrt{\frac{\pi\rho_2}{k}} \times \left\{\cos\theta\cos\phi\frac{\sin Y}{Y}\left[e^{jf_1}F(t_1', t_2') + e^{jf_2}F(t_1'', t_2'')\right]\right\} \tag{13-29b}$$

$$L_\phi = -E_2 \frac{b}{2}\sqrt{\frac{\pi\rho_2}{k}} \times \left\{\sin\phi\frac{\sin Y}{Y}\left[e^{jf_1}F(t_1', t_2') + e^{jf_2}F(t_1'', t_2'')\right]\right\} \tag{13-29c}$$

The far-zone electric field components of (12-10a)–(12-10c) can then be expressed as

$$\boxed{E_r = 0} \tag{13-30a}$$

$$\boxed{E_\theta = jE_2\frac{b}{8}\sqrt{\frac{k\rho_2}{\pi}}\frac{e^{-jkr}}{r} \times \left\{\sin\phi(1 + \cos\theta)\frac{\sin Y}{Y}\left[e^{jf_1}F(t_1', t_2') + e^{jf_2}F(t_1'', t_2'')\right]\right\}} \tag{13-30b}$$

$$E_\phi = jE_2\frac{b}{8}\sqrt{\frac{k\rho_2}{\pi}}\frac{e^{-jkr}}{r} \times \left\{\cos\phi(\cos\theta + 1)\frac{\sin Y}{Y}\left[e^{jf_1}F(t_1', t_2') + e^{jf_2}F(t_1'', t_2'')\right]\right\} \tag{13-30c}$$

The electric field in the principal E- and H-planes reduces to

E-Plane ($\phi = \pi/2$)

$$E_r = E_\phi = 0 \tag{13-31a}$$

$$E_\theta = jE_2\frac{b}{8}\sqrt{\frac{k\rho_2}{\pi}}\frac{e^{-jkr}}{r} \times \left\{(1 + \cos\theta)\frac{\sin Y}{Y}\left[e^{jf_1}F(t_1', t_2') + e^{jf_2}F(t_1'', t_2'')\right]\right\} \tag{13-31b}$$

$$Y = \frac{kb}{2}\sin\theta \tag{13-31c}$$

$$k_x' = \frac{\pi}{a_1} \tag{13-31d}$$

$$k_x'' = -\frac{\pi}{a_1} \tag{13-31e}$$

H-Plane ($\phi = 0$)

$$E_r = E_\theta = 0 \tag{13-32a}$$

$$E_\phi = jE_2\frac{b}{8}\sqrt{\frac{k\rho_2}{\pi}}\frac{e^{-jkr}}{r} \times \{(\cos\theta + 1)\left[e^{jf_1}F(t_1', t_2') + e^{jf_2}F(t_1'', t_2'')\right]\} \tag{13-32b}$$

$$k_x' = k\sin\theta + \frac{\pi}{a_1} \tag{13-32c}$$

$$k_x'' = k\sin\theta - \frac{\pi}{a_1} \tag{13-32d}$$

with f_1, f_2, $F(t_1', t_2')$, $F(t_1'', t_2'')$, t_1', t_2', t_1'', and t_2'' as defined previously.

Computations similar to those for the E-plane sectoral horn were also performed for the H-plane sectoral horn. A three-dimensional field pattern of an H-plane sectoral horn is shown in Figure 13.11. Its corresponding E- and H-plane patterns are displayed in Figure 13.12. This horn exhibits narrow pattern characteristics in the flared H-plane.

Normalized H-plane patterns for a given length horn ($\rho_2 = 12\lambda$) and different flare angles are shown in Figure 13.13. A total of four patterns is illustrated. Since each pattern is symmetrical, only half of each pattern is displayed. As the included angle is increased, the pattern begins to become narrower up to a given flare. Beyond that point the pattern begins to broaden, attributed primarily to the phase taper (phase

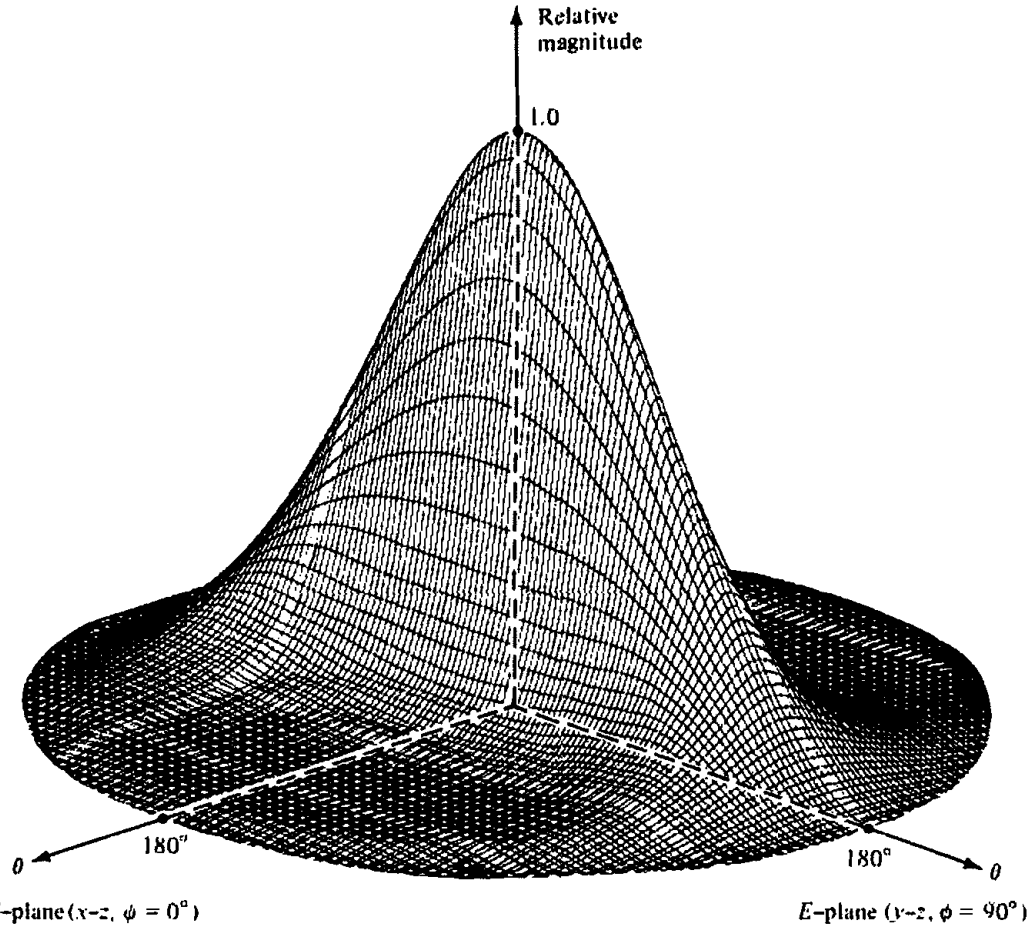

Figure 13.11 Three-dimensional field pattern of an *H*-plane sectoral horn ($\rho_2 = 6\lambda$, $a_1 = 5.5\lambda$, $b = 0.25\lambda$).

error) across the aperture of the horn. To correct this, a lens is usually placed at the horn aperture which would yield narrower patterns as the flare angle is increased. Similar pattern variations are evident when the flare angle of the horn is maintained fixed while its length is varied.

The *universal curves* for the *H*-plane sectoral horn are based on (13-32b), in the absence of the factor $(1 + \cos\theta)$. Neglecting the $(1 + \cos\theta)$ factor, the normalized *H*-plane electric field of the *H*-plane sectoral horn can be written as

$$E_{\phi n} = |e^{jf_1}F(t_1', t_2') + e^{jf_2}F(t_1'', t_2'')| \tag{13-33}$$

$$F(t_1, t_2) = [C(t_2) - C(t_1)] - j[S(t_2) - S(t_1)] \tag{13-33a}$$

$$f_1 = \frac{k_x'^2\rho_2}{2k} = \frac{\rho_2}{2k}\left(k\sin\theta + \frac{\pi}{a_1}\right)^2$$

$$= \frac{\pi}{8}\left(\frac{1}{t}\right)\left(\frac{a_1}{\lambda}\sin\theta\right)^2\left[1 + \frac{1}{2}\left(\frac{\lambda}{a_1\sin\theta}\right)\right]^2 \tag{13-33b}$$

$$f_2 = \frac{k_x''^2\rho_2}{2k} = \frac{\rho_2}{2k}\left(k\sin\theta - \frac{\pi}{a_1}\right)^2$$

$$= \frac{\pi}{8}\left(\frac{1}{t}\right)\left(\frac{a_1}{\lambda}\sin\theta\right)^2\left[1 - \frac{1}{2}\left(\frac{\lambda}{a_1\sin\theta}\right)\right]^2 \tag{13-33c}$$

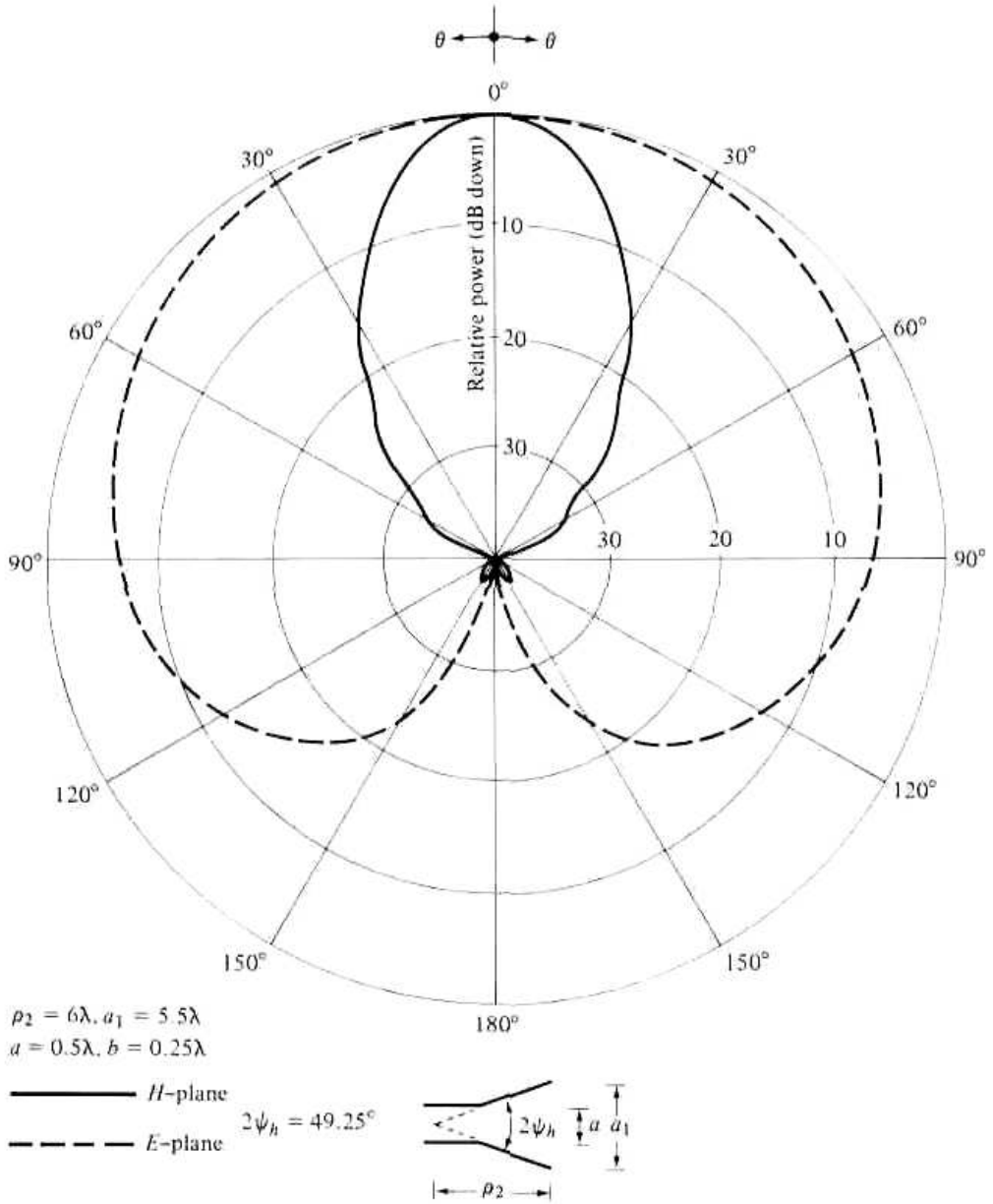

Figure 13.12 *E*- and *H*-plane patterns of *H*-plane sectoral horn.

$$t_1' = \sqrt{\frac{1}{\pi k \rho_2}}\left(-\frac{ka_1}{2} - k_x'\rho_2\right)$$

$$= 2\sqrt{t}\left[-1 - \frac{1}{4}\left(\frac{1}{t}\right)\left(\frac{a_1}{\lambda}\sin\theta\right) - \frac{1}{8}\left(\frac{1}{t}\right)\right] \tag{13-33d}$$

$$t_2' = \sqrt{\frac{1}{\pi k \rho_2}}\left(+\frac{ka_1}{2} - k_x'\rho_2\right)$$

$$= 2\sqrt{t}\left[+1 - \frac{1}{4}\left(\frac{1}{t}\right)\left(\frac{a_1}{\lambda}\sin\theta\right) - \frac{1}{8}\left(\frac{1}{t}\right)\right] \tag{13-33e}$$

$$t_1'' = \sqrt{\frac{1}{\pi k \rho_2}}\left(-\frac{ka_1}{2} - k_x''\rho_2\right)$$

$$= 2\sqrt{t}\left[-1 - \frac{1}{4}\left(\frac{1}{t}\right)\left(\frac{a_1}{\lambda}\sin\theta\right) + \frac{1}{8}\left(\frac{1}{t}\right)\right] \tag{13-33f}$$

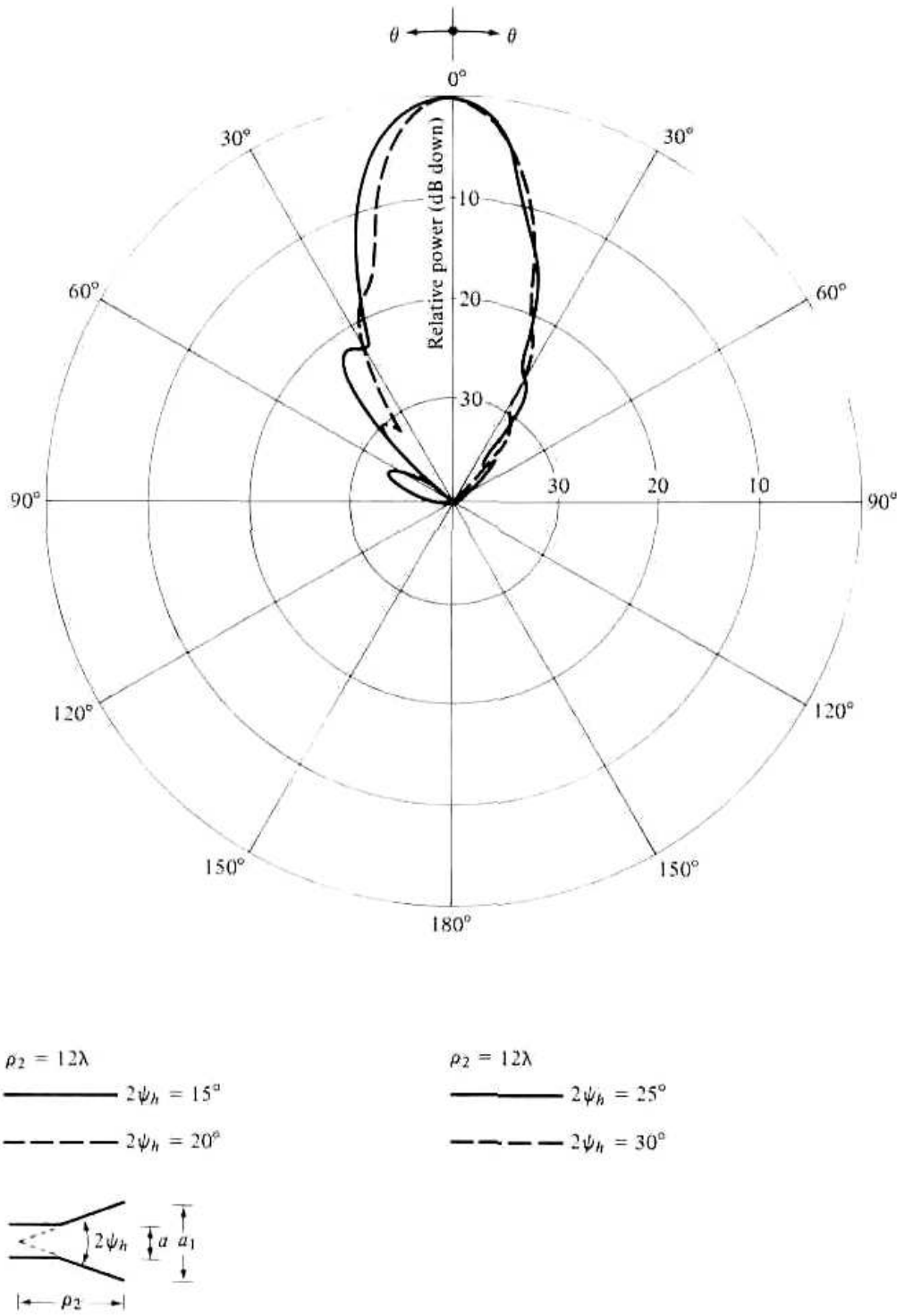

Figure 13.13 *H*-plane patterns of *H*-plane sectoral horn for constant length and different included angles.

$$t_2'' = \sqrt{\frac{1}{\pi k \rho_2}}\left(+\frac{ka_1}{2} - k_x''\rho_2\right)$$

$$= 2\sqrt{t}\left[+1 - \frac{1}{4}\left(\frac{1}{t}\right)\left(\frac{a_1}{\lambda}\sin\theta\right) + \frac{1}{8}\left(\frac{1}{t}\right)\right] \tag{13-33g}$$

$$t = \frac{a_1^2}{8\lambda\rho_2} \tag{13-33h}$$

For a given value of t, as given by (13-33h), the normalized field of (13-33) is plotted in Figure 13.14 as a function of $(a_1/\lambda)\sin\theta$ for $t = \frac{1}{\sqrt{3}}, \frac{1}{8}, \frac{1}{3}, \frac{1}{2}, \frac{3}{5}$ and 1. Following a procedure identical to that for the E-plane sectoral horn, the H-plane pattern of any H-plane sectoral horn can be obtained from these curves. The normalized value of the $(1 + \cos\theta)$ factor in dB, written as $20\log_{10}[(1 + \cos\theta)/2]$, must also be included.

13.3.3 Directivity

To find the directivity of the H-plane sectoral horn, a procedure similar to that for the E-plane is used. As for the E-plane sectoral horn, the maximum radiation is directed nearly along the z-axis ($\theta = 0°$). Thus

$$|E_\theta|_{\max} = |E_2|\frac{b}{4r}\sqrt{\frac{2\rho_2}{\lambda}}\Big|\sin\phi\{[C(t_2') + C(t_2'') - C(t_1') - C(t_1'')] - j[S(t_2') + S(t_2'') - S(t_1') - S(t_1'')]\}\Big| \tag{13-34}$$

$$t_1' = \sqrt{\frac{1}{\pi k\rho_2}}\left(-\frac{ka_1}{2} - \frac{\pi}{a_1}\rho_2\right) \tag{13-34a}$$

$$t_2' = \sqrt{\frac{1}{\pi k\rho_2}}\left(+\frac{ka_1}{2} - \frac{\pi}{a_1}\rho_2\right) \tag{13-34b}$$

$$t_1'' = \sqrt{\frac{1}{\pi k\rho_2}}\left(-\frac{ka_1}{2} + \frac{\pi}{a_1}\rho_2\right) = -t_2' = v \tag{13-34c}$$

$$t_2'' = \sqrt{\frac{1}{\pi k\rho_2}}\left(+\frac{ka_1}{2} + \frac{\pi}{a_1}\rho_2\right) = -t_1' = u \tag{13-34d}$$

Since

$$C(-x) = -C(x) \tag{13-35a}$$

$$S(-x) = -S(x) \tag{13-35b}$$

$$|E_\theta|_{\max} = |E_2|\frac{b}{r}\sqrt{\frac{\rho_2}{2\lambda}}\Big|\sin\phi\{[C(u) - C(v)] - j[S(u) - S(v)]\}\Big| \tag{13-36}$$

$$u = t_2'' = -t_1' = \sqrt{\frac{1}{\pi k\rho_2}}\left(+\frac{ka_1}{2} + \frac{\pi}{a_1}\rho_2\right) = \frac{1}{\sqrt{2}}\left(\frac{\sqrt{\lambda\rho_2}}{a_1} + \frac{a_1}{\sqrt{\lambda\rho_2}}\right) \tag{13-36a}$$

$$v = t_1'' = -t_2' = \sqrt{\frac{1}{\pi k\rho_2}}\left(-\frac{ka_1}{2} + \frac{\pi}{a_1}\rho_2\right) = \frac{1}{\sqrt{2}}\left(\frac{\sqrt{\lambda\rho_2}}{a_1} - \frac{a_1}{\sqrt{\lambda\rho_2}}\right) \tag{13-36b}$$

Similarly

$$|E_\phi|_{\max} = |E_2|\frac{b}{r}\sqrt{\frac{\rho_2}{2\lambda}}\Big|\cos\phi\{[C(u) - C(v)] - j[S(u) - S(v)]\}\Big| \tag{13-37}$$

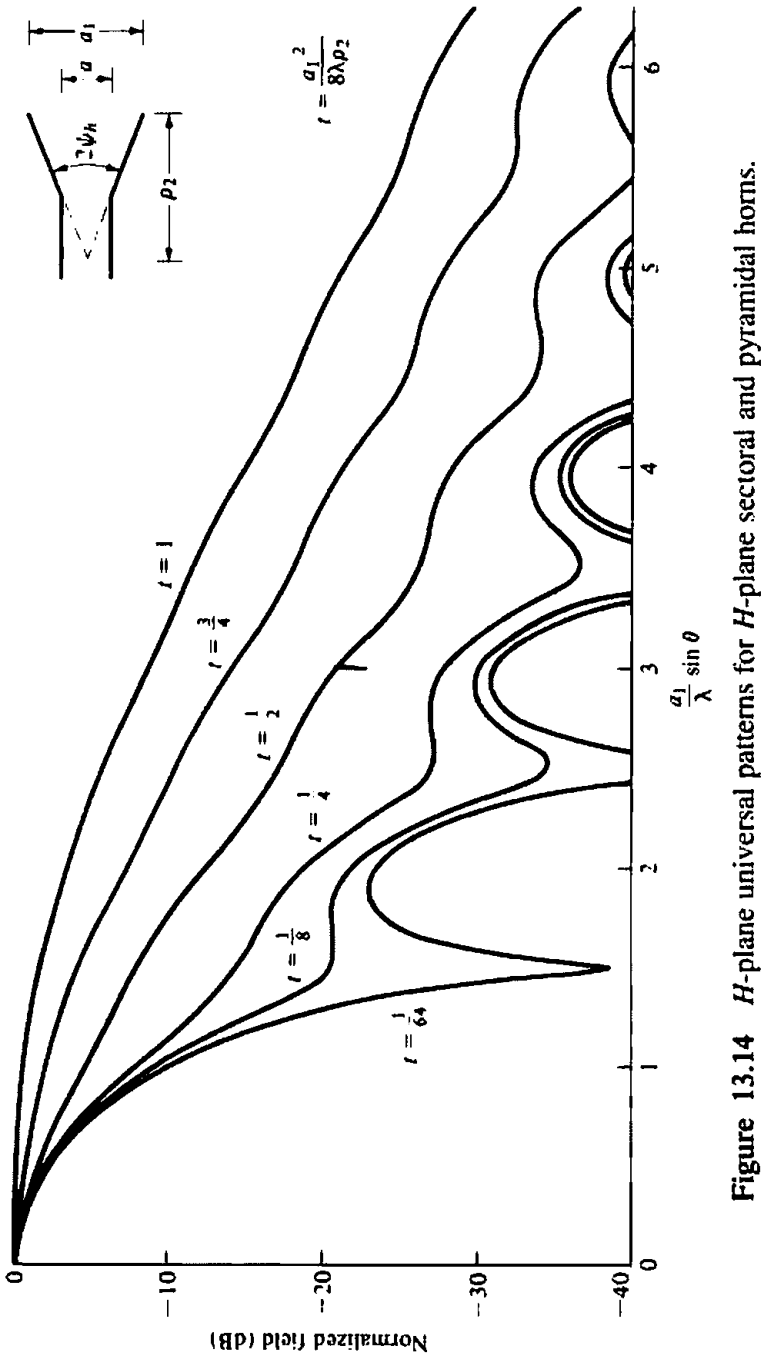

Figure 13.14 *H*-plane universal patterns for *H*-plane sectoral and pyramidal horns.

Thus

$$|\mathbf{E}|_{\max} = \sqrt{|E_\theta|^2_{\max} + |E_\phi|^2_{\max}} = |E_2|\frac{b}{r}\sqrt{\frac{\rho_2}{2\lambda}}\{[C(u) - C(v)]^2 + [S(u) - S(v)]^2\}^{1/2} \tag{13-38}$$

$$U_{\max} = |E_2|^2\frac{b^2\rho_2}{4\eta\lambda}\{[C(u) - C(v)]^2 + [S(u) - S(v)]^2\} \tag{13-39}$$

The total power radiated can be obtained by simply integrating the average power density over the mouth of the horn, and it is given by

$$P_{\text{rad}} = |E_2|^2\frac{ba_1}{4\eta} \tag{13-40}$$

Using (13-39) and (13-40), the directivity for the H-plane sectoral horn can be written as

$$\boxed{D_H = \frac{4\pi U_{\max}}{P_{\text{rad}}} = \frac{4\pi b\rho_2}{a_1\lambda} \times \{[C(u) - C(v)]^2 + [S(u) - S(v)]^2\}} \tag{13-41}$$

where

$$\boxed{u = \frac{1}{\sqrt{2}}\left(\frac{\sqrt{\lambda\rho_2}}{a_1} + \frac{a_1}{\sqrt{\lambda\rho_2}}\right)} \tag{13-41a}$$

$$\boxed{v = \frac{1}{\sqrt{2}}\left(\frac{\sqrt{\lambda\rho_2}}{a_1} - \frac{a_1}{\sqrt{\lambda\rho_2}}\right)} \tag{13-41b}$$

The half-power beamwidth (HPBW) as a function of flare angle is plotted in Figure 13.15. The normalized directivity (relative to the constant aperture dimension b) for different horn lengths, as a function of aperture dimension a_1, is displayed in Figure 13.16. As for the E-plane sectoral horn, the HPBW exhibits a monotonic decrease and the directivity a monotonic increase up to a given flare; beyond that, the trends are reversed.

If the values of a_1 (in λ), which correspond to the maximum directivities in Figure 13.16, are plotted versus their corresponding values of ρ_2 (in λ), it can be shown that each optimum directivity occurs when

$$\boxed{a_1 \simeq \sqrt{3\lambda\rho_2}} \tag{13-41c}$$

with a corresponding value of t equal to

$$\boxed{t|_{a_1=\sqrt{3\lambda\rho_2}} = t_{op} = \left.\frac{a_1^2}{8\lambda\rho_2}\right|_{a_1=\sqrt{3\lambda\rho_2}} = \frac{3}{8}} \tag{13-41d}$$

The directivity of an H-plane sectoral horn can also be computed by using the following procedure [14].

1. Calculate A by

$$A = \frac{a_1}{\lambda}\sqrt{\frac{50}{\rho_h/\lambda}} \tag{13-42a}$$

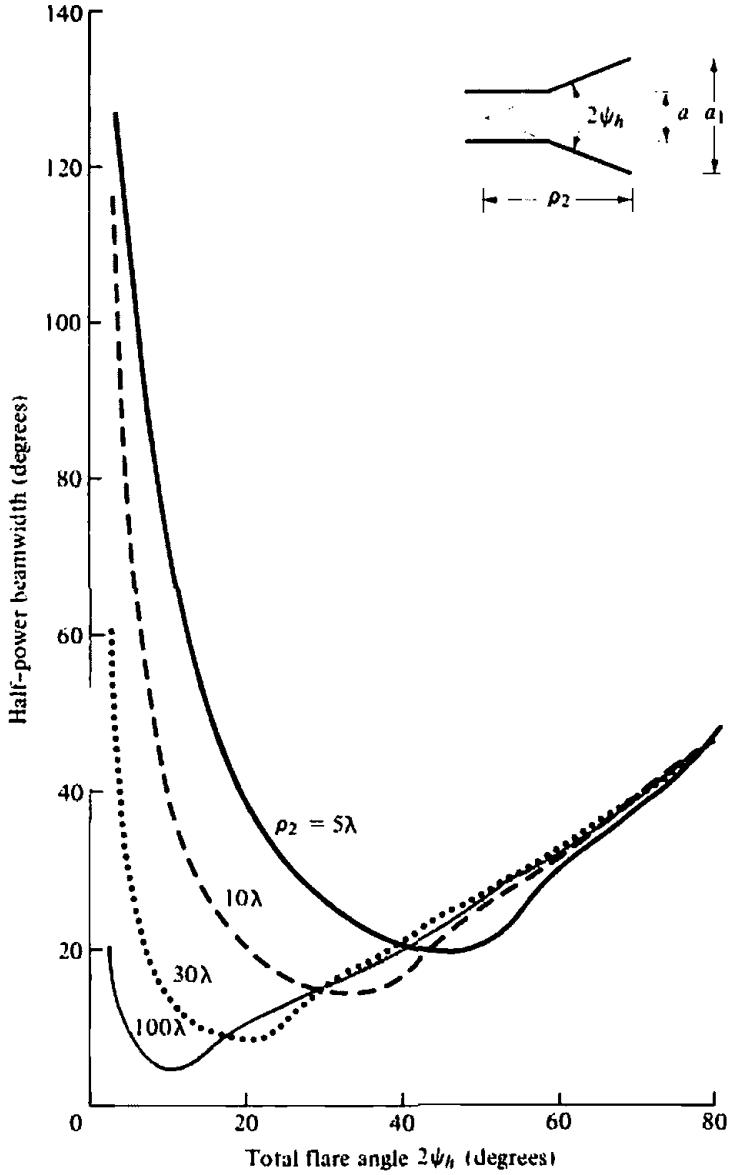

Figure 13.15 Half-power beamwidth of *H*-plane sectoral horn as a function of included angle and for different lengths.

2. Using this value of A, find the corresponding value of G_H from Figure 13.17. If the value of A is smaller than 2, then compute G_H using

$$G_H = \frac{32}{\pi} A \tag{13-42b}$$

3. Calculate D_H by using the value of G_H from Figure 13.17 or from (13-42b). Thus

$$\boxed{D_H = \frac{b}{\lambda} \frac{G_h}{\sqrt{\frac{50}{\rho_h/\lambda}}}} \tag{13-42c}$$

This is the actual directivity of the horn.

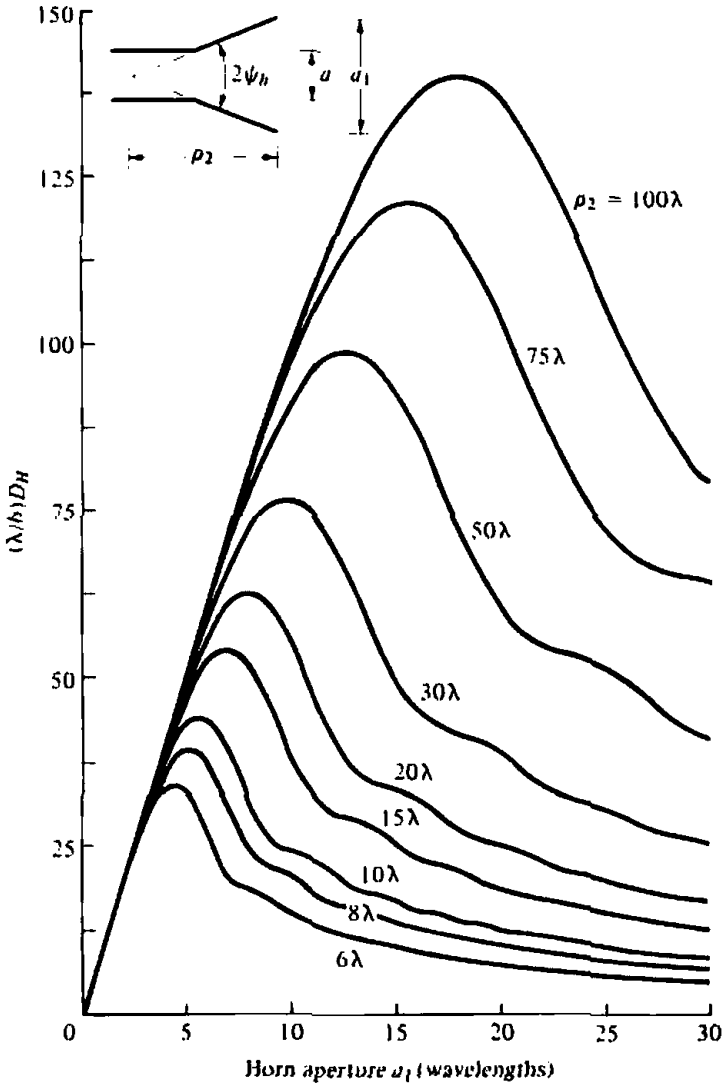

Figure 13.16 Normalized directivity of H-plane sectoral horn as a function of aperture size and for different lengths.

Example 13.4

An H-plane sectoral horn has dimensions of $a = 0.5\lambda$, $b = 0.25\lambda$, $a_1 = 5.5\lambda$, and $\rho_2 = 6\lambda$. Compute the directivity using (13-41) and (13-42c). Compare the answers.

SOLUTION

For this horn

$$u = \frac{1}{\sqrt{2}}\left(\frac{\sqrt{6}}{5.5} + \frac{5.5}{\sqrt{6}}\right) = 1.9$$

$$v = \frac{1}{\sqrt{2}}\left(\frac{\sqrt{6}}{5.5} - \frac{5.5}{\sqrt{6}}\right) = -1.273$$

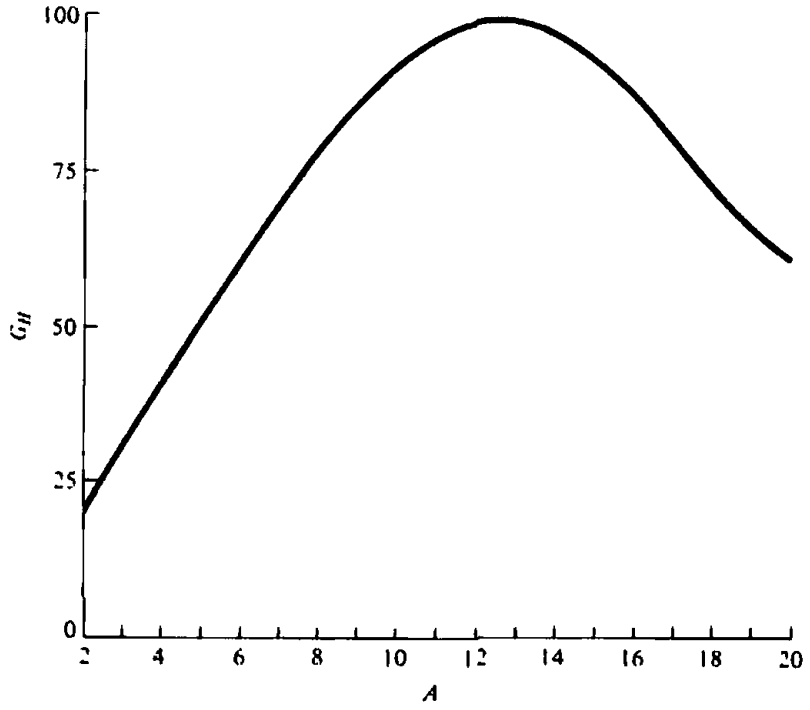

Figure 13.17 G_H as a function of A. (SOURCE: Adopted from data by E. H. Braun, "Some Data for the Design of Electromagnetic Horns," *IRE Trans. Antennas Propagat.*, Vol. AP-4, No. 1, January 1956. © (1956) IEEE)

Therefore (from Appendix IV)

$$\begin{aligned} C(1.9) &= 0.394 \\ C(-1.273) &= -C(1.273) = -0.659 \\ S(1.9) &= 0.373 \\ S(-1.273) &= -S(1.273) = -0.669 \end{aligned}$$

Using (13-41)

$$D_H = \frac{4\pi(0.25)6}{5.5}[(0.394 + 0.659)^2 + (0.373 + 0.669)^2]$$

$$D_H = 7.52 = 8.763 \text{ dB}$$

To compute the directivity using (13-42c), the following parameters are computed:

$$\rho_h = \lambda\sqrt{(6)^2 + (5.5/2)^2} = 6.6\lambda$$

$$\sqrt{\frac{50}{\rho_h/\lambda}} = \sqrt{\frac{50}{6.6}} = 2.7524$$

$$A = 5.5(2.7524) = 15.14$$

For $A = 15.14$, $G_H = 91.8$ from Figure 13.17. Thus, using (13-42c)

$$D_H = \frac{0.25(91.8)}{2.7524} = 8.338 = 9.21 \text{ dB}$$

Although there is a good agreement between the results of (13-41) and (13-42c), they do not compare as well as those of Example 13.3.

13.4 PYRAMIDAL HORN

The most widely used horn is the one which is flared in both directions, as shown in Figure 13.18. It is widely referred to as a pyramidal horn, and its radiation characteristics are essentially a combination of the E- and H-plane sectoral horns.

13.4.1 Aperture Fields, Equivalent, and Radiated Fields

To simplify the analysis and to maintain a modeling that leads to computations that have been shown to correlate well with experimental data, the tangential components of the E- and H-fields over the aperture of the horn are approximated by

$$E_y'(x', y') = E_0 \cos\left(\frac{\pi}{a_1} x'\right) e^{-j[k(x'^2/\rho_2 + y'^2/\rho_1)/2]} \tag{13-43a}$$

$$H_x'(x', y') = -\frac{E_0}{\eta} \cos\left(\frac{\pi}{a_1} x'\right) e^{-j[k(x'^2/\rho_2 + y'^2/\rho_1)/2]} \tag{13-43b}$$

and the equivalent current densities by

$$J_y(x', y') = -\frac{E_0}{\eta} \cos\left(\frac{\pi}{a_1} x'\right) e^{-j[k(x'^2/\rho_2 + y'^2/\rho_1)/2]} \tag{13-44a}$$

$$M_x(x', y') = E_0 \cos\left(\frac{\pi}{a_1} x'\right) e^{-j[k(x'^2/\rho_2 + y'^2/\rho_1)/2]} \tag{13-44b}$$

The above expressions contain a cosinusoidal amplitude distribution in the x' direction and quadratic phase variations in both the x' and y' directions, similar to those of the sectoral E- and H-plane horns.

The N_θ, N_ϕ, L_θ and L_ϕ can now be formulated as before, and it can be shown that they are given by

$$N_\theta = -\frac{E_0}{\eta} \cos\theta \sin\phi I_1 I_2 \tag{13-45a}$$

$$N_\phi = -\frac{E_0}{\eta} \cos\phi I_1 I_2 \tag{13-45b}$$

$$L_\theta = E_0 \cos\theta \cos\phi I_1 I_2 \tag{13-45c}$$

$$L_\phi = -E_0 \sin\phi I_1 I_2 \tag{13-45d}$$

where

$$I_1 = \int_{-a_1/2}^{+a_1/2} \cos\left(\frac{\pi}{a} x'\right) e^{-jk[x'^2/(2\rho_1) - x'\sin\theta\cos\phi]}\, dx' \tag{13-45e}$$

$$I_2 = \int_{-b_1/2}^{+b_1/2} e^{-jk[y'^2/(2\rho_1) - y'\sin\theta\sin\phi]}\, dy' \tag{13-45f}$$

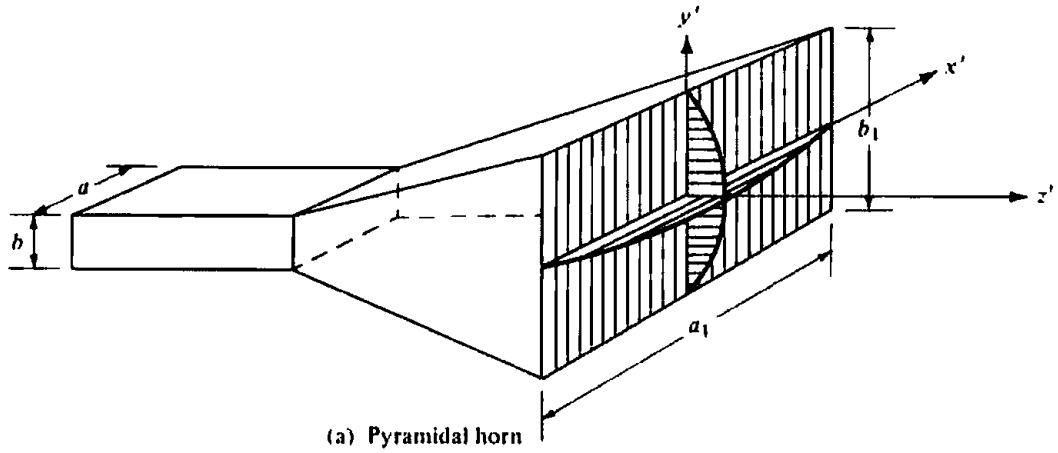

(a) Pyramidal horn

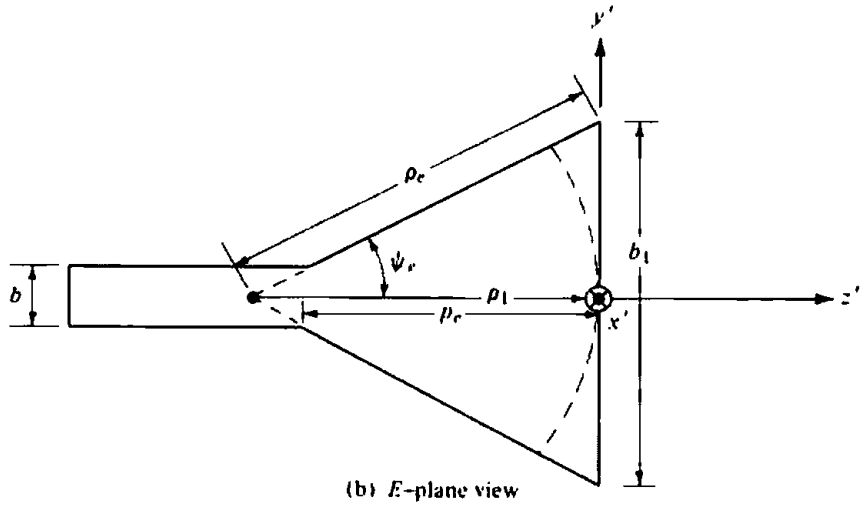

(b) *E*-plane view

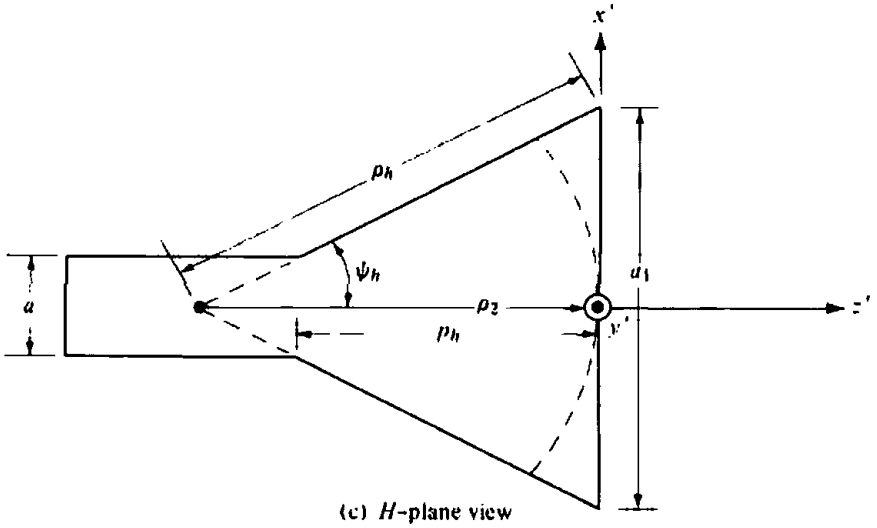

(c) *H*-plane view

Figure 13.18 Pyramidal horn and coordinate system.

Using (13-23b), (13-25), (13-26), and (13-27), (13-45e) can be expressed as

$$I_1 = \frac{1}{2}\sqrt{\frac{\pi\rho_2}{k}}\left\{e^{j(k_x'^2\rho_2/2k)}\{[C(t_2') - C(t_1')] - j[S(t_2') - S(t_1')]\} + e^{j(k_x''^2\rho_2/2k)}\{[C(t_2'') - C(t_1'')] - j[S(t_2'') - S(t_1'')]\}\right\} \tag{13-46}$$

where t_1', t_2', k_x', t_1'', t_2'', and k_x'' are given by (13-26a)–(13-26c) and (13-27a)–(13-27c). Similarly, using (13-5)–(13-8d), I_2 of (13-45f) can be written as

$$I_2 = \sqrt{\frac{\pi\rho_1}{k}}\, e^{j(k_x^2\rho_1/2k)}\{[C(t_2) - C(t_1)] - j[S(t_2) - S(t_1)]\} \tag{13-47}$$

where k_x, t_1, and t_2 are given by (13-5a), (13-8a), and (13-8b).

Combining (13-45a)–(13-45d), the far-zone **E**- and **H**-field components of (12-10a)–(12-10c) reduce to

$$E_r = 0 \tag{13-48a}$$

$$E_\theta = -j\frac{ke^{jkr}}{4\pi r}[L_\phi + \eta N_\theta] = j\frac{kE_0e^{-jkr}}{4\pi r}[\sin\phi(1 + \cos\theta)\, I_1I_2] \tag{13-48b}$$

$$E_\phi = +j\frac{ke^{-jkr}}{4\pi r}[L_\theta - \eta N_\phi] = j\frac{kE_0e^{-jkr}}{4\pi r}[\cos\phi(\cos\theta + 1)\, I_1I_2] \tag{13-48c}$$

where I_1 and I_2 are given by (13-46) and (13-47), respectively.

The fields radiated by a pyramidal horn, as given by (13-48a)–(13-48c), are valid for all angles of observation. An examination of these equations reveals that the principal E-plane pattern ($\phi = \pi/2$) of a pyramidal horn, aside from a normalization factor, is identical to the E-plane pattern of an E-plane sectoral horn. Similarly the H-plane ($\phi = 0$) is identical to that of an H-plane sectoral horn. Therefore the pattern of a pyramidal horn is very narrow in both principal planes and, in fact, in all planes. This is illustrated in Figure 13.19. The corresponding E-plane pattern is shown in Figure 13.4 and the H-plane pattern in Figure 13.12.

To demonstrate that the maximum radiation for a pyramidal horn is not necessarily directed along its axis, the three-dimensional field pattern for a horn with $\rho_1 = \rho_2 = 6\lambda$, $a_1 = 12\lambda$, $b_1 = 6\lambda$, $a = 0.50\lambda$ and $b = 0.25\lambda$ is displayed in Figure 13.20. The corresponding two-dimensional E- and H-plane patterns are shown in Figure 13.21. The maximum does not occur on axis because the phase error taper at the aperture is such that the rays emanating from the different parts of the aperture toward the axis are not in phase and do not add constructively.

To physically construct a pyramidal horn, the dimension p_e of Figure 13.18(b) given by

$$p_e = (b_1 - b)\left[\left(\frac{\rho_e}{b_1}\right)^2 - \frac{1}{4}\right]^{1/2} \tag{13-49a}$$

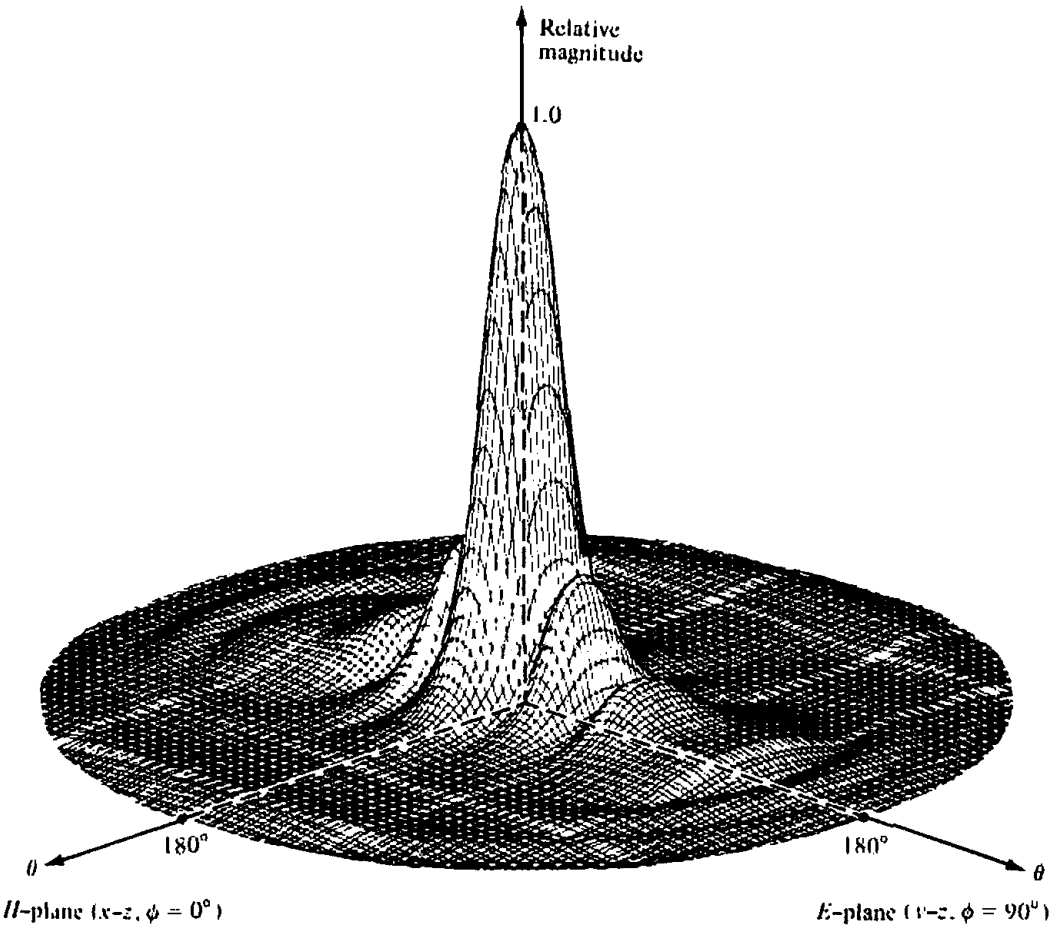

Figure 13.19 Three-dimensional field pattern of a pyramidal horn ($\rho_1 = \rho_2 = 6\lambda$, $a_1 = 5.5\lambda$, $b_1 = 2.75\lambda$, $a = 0.5\lambda$, $b = 0.25\lambda$).

should be equal to the dimension ρ_h of Figure 13.18(c) given by

$$\rho_h = (a_1 - a)\left[\left(\frac{\rho_h}{a_1}\right)^2 - \frac{1}{4}\right]^{1/2} \tag{13-49b}$$

The dimensions chosen for Figures 13.19 and 13.20 do satisfy these requirements. For the horn of Figure 13.19, $\rho_e = 6.1555\lambda$, $\rho_h = 6.6\lambda$, and $\rho_e = \rho_h = 5.4544\lambda$, whereas for that of Figure 13.20, $\rho_e = 6.7082\lambda$, $\rho_h = 8.4853\lambda$, and $\rho_e = \rho_h = 5.75\lambda$. The fields of (13-48a)–(13-48c) provide accurate patterns for angular regions near the main lobe and its closest minor lobes. To accurately predict the field intensity of the pyramidal and other horns, especially in the minor lobes, diffraction techniques can be utilized [15]–[18]. These methods take into account diffractions that occur near the aperture edges of the horn. The diffraction contributions become more dominant in regions where the radiation of (13-48a)–(13-48c) is of very low intensity.

In addition to the previous methods, the horn antenna has been examined using full-wave analyses, such as the Method of Moments (MoM) [8] and the Finite-Difference Time-Domain (FDTD) [19]. These methods yield more accurate results in all regions, and they are able to include many of the other features of the horn, such as its wall thickness, etc. Predicted patterns based on these methods compare extremely well with measurements, even in regions of very low intensity (such as the back lobes). An example of such a comparison is made in Figure 13.22 (a,b) for the E- and

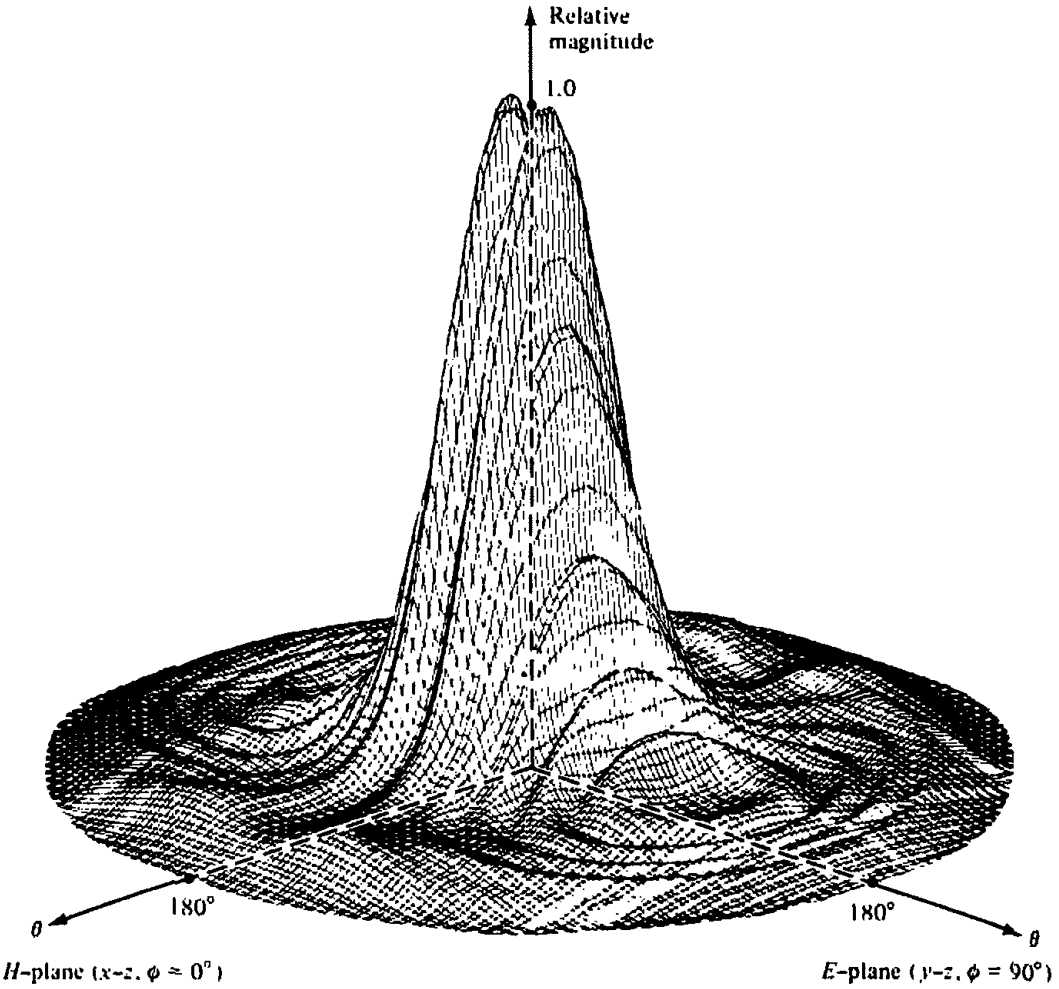

Figure 13.20 Three-dimensional field pattern of a pyramidal horn with maximum not on axis ($\rho_1 = \rho_2 = 6\lambda$, $a_1 = 12\lambda$, $b_1 = 6\lambda$, $a = 0.5\lambda$, $b = 0.25\lambda$).

H-plane patterns of a 20-dB standard gain horn whose Method of Moment predicted values are compared with measured patterns and with predicted values based on (13-48a) and (13-48c), which in Figure 13.22 are labeled as *approximate*. It is apparent that the MoM predicted patterns compare extremely well with the measured data.

All of the patterns presented previously represent the main polarization of the field radiated by the antenna (referred to as *co-polarized* or *co-pol*). If the horn is symmetrical and it is excited in the dominant mode, ideally there should be no field component radiated by the antenna which is orthogonal to the main polarization (referred to as *cross-polarization* or *cross-pol*), especially in the principal planes. However, in practice, either because of nonsymmetries, defects in construction and/or excitation of higher order modes, all antennas exhibit cross-polarized components. These cross-pol components are usually of very low intensity compared to those of the primarily polarization. For good designs, these should be 30 or more dB below the co-polarized fields and are difficult to measure accurately or be symmetrical, as they should be in some cases.

13.4.2 Directivity

As for the *E*- and *H*-plane sectoral horns, the directivity of the pyramidal configuration is vital to the antenna designer. The maximum radiation of the pyramidal horn is

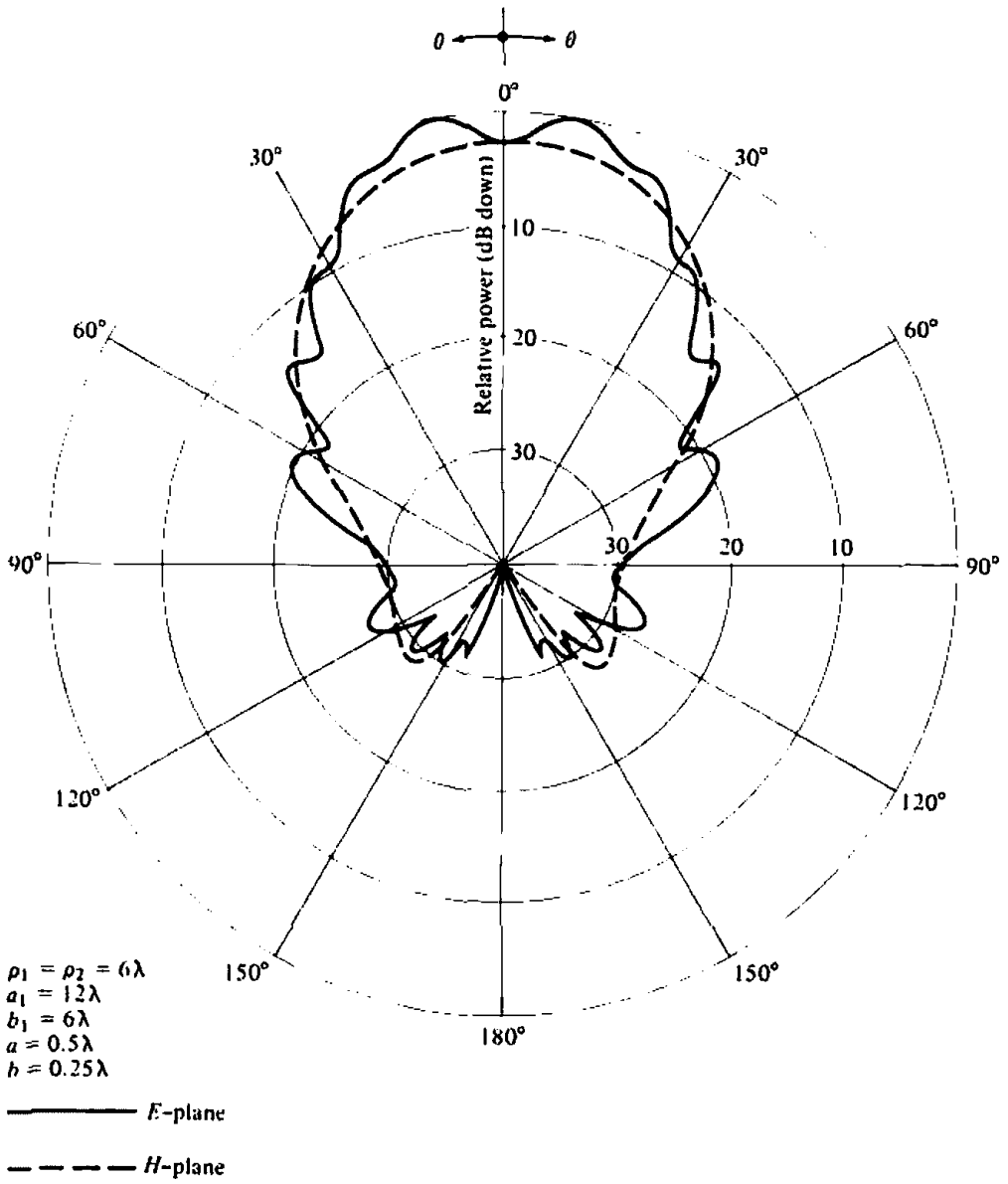

Figure 13.21 *E*- and *H*-plane amplitude patterns of a pyramidal horn with maximum not on-axis.

directed nearly along the z-axis ($\theta = 0°$). It is a very simple exercise to show that $|E_\theta|_{\max}$, $|E_\phi|_{\max}$, and in turn $U_{\max}$ can be written, using (13-48b) and (13-48c), as

$$|E_\theta|_{\max} = |E_0 \sin\phi| \frac{\sqrt{\rho_1\rho_2}}{r} \{[C(u) - C(v)]^2 + [S(u) - S(v)]^2\}^{1/2} \times \left\{ C^2\left(\frac{b_1}{\sqrt{2\lambda\rho_1}}\right) + S^2\left(\frac{b_1}{\sqrt{2\lambda\rho_1}}\right)\right\}^{1/2} \tag{13-50a}$$

$$|E_\phi|_{\max} = |E_0 \cos\phi| \frac{\sqrt{\rho_1\rho_2}}{r} \{[C(u) - C(v)]^2 + [S(u) - S(v)]^2\}^{1/2} \times \left\{ C^2\left(\frac{b_1}{\sqrt{2\lambda\rho_1}}\right) + S^2\left(\frac{b_1}{\sqrt{2\lambda\rho_1}}\right)\right\}^{1/2} \tag{13-50b}$$

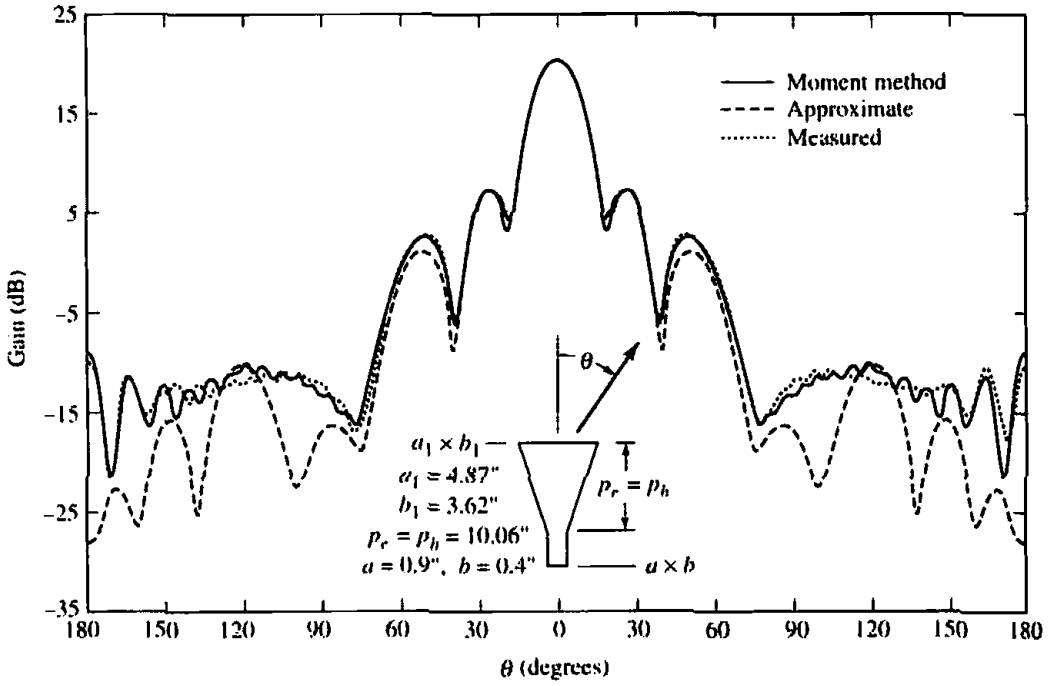

(a) E-plane

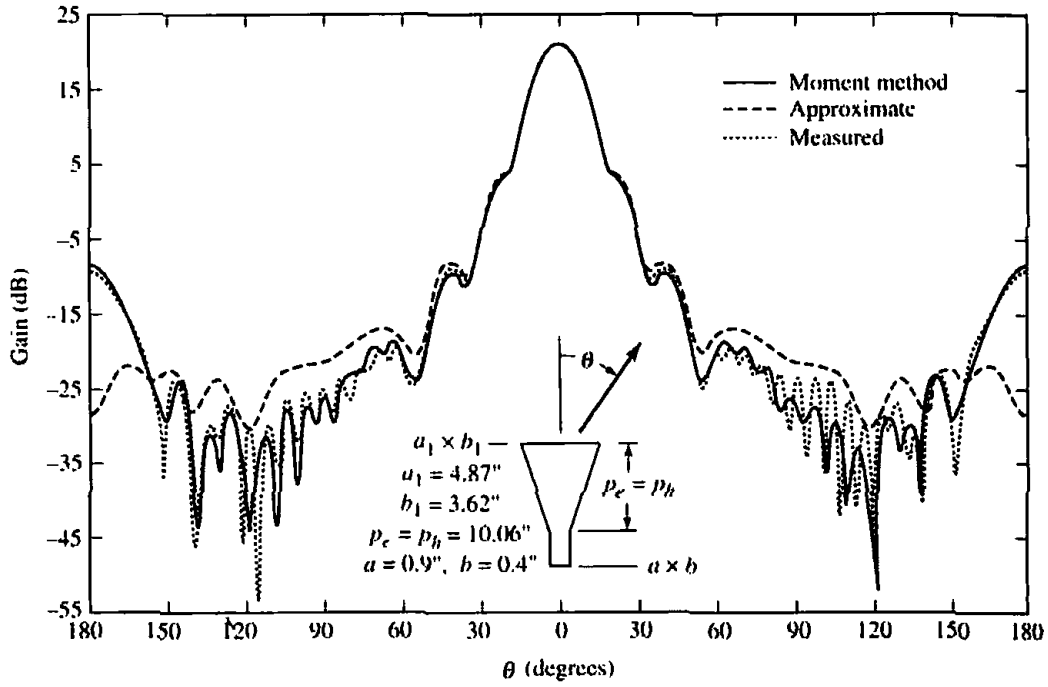

(b) H-plane

Figure 13.22 Comparison of E- and H-plane patterns for 20-dB standard-gain horn at 10 GHz.

$$U_{\max} = \frac{r^2}{2\eta}|\mathbf{E}|^2_{\max} = |E_0|^2 \frac{\rho_1\rho_2}{2\eta}\{[C(u) - C(v)]^2 + [S(u) - S(v)]^2\} \times \left\{C^2\left(\frac{b_1}{\sqrt{2\lambda\rho_1}}\right) + S^2\left(\frac{b_1}{\sqrt{2\lambda\rho_1}}\right)\right\} \tag{13-50c}$$

where u and v are defined by (13-41a) and (13-41b).

Since

$$P_{\text{rad}} = |E_0|^2 \frac{a_1 b_1}{4\eta} \tag{13-51}$$

the directivity of the pyramidal horn can be written as

$$\boxed{D_p = \frac{4\pi U_{\max}}{P_{\text{rad}}} = \frac{8\pi\rho_1\rho_2}{a_1 b_1}\{[C(u) - C(v)]^2 + [S(u) - S(v)]^2\} \times \left\{C^2\left(\frac{b_1}{\sqrt{2\lambda\rho_1}}\right) + S^2\left(\frac{b_1}{\sqrt{2\lambda\rho_1}}\right)\right\}} \tag{13-52}$$

which reduces to

$$\boxed{D_p = \frac{\pi\lambda^2}{32ab} D_E D_H} \tag{13-52a}$$

where D_E and D_H are the directivities of the E- and H-plane sectoral horns as given by (13-19) and (13-41), respectively. This is a well-known relationship and has been used extensively in the design of pyramidal horns.

The directivity (in dB) of a pyramidal horn, over isotropic, can also be approximated by

$$\boxed{D_p(\text{dB}) = 10\left[1.008 + \log_{10}\left(\frac{a_1 b_1}{\lambda^2}\right)\right] - (L_e + L_h)} \tag{13-53}$$

where L_e and L_h represent, respectively, the losses (in dB) due to phase errors in the E- and H-planes of the horn which are found plotted in Figure 13.23.

The directivity of a pyramidal horn can also be calculated by doing the following [14].

1. Calculate

$$A = \frac{a_1}{\lambda}\sqrt{\frac{50}{\rho_h/\lambda}} \tag{13-54a}$$

$$B = \frac{b_1}{\lambda}\sqrt{\frac{50}{\rho_e/\lambda}} \tag{13-54b}$$

2. Using A and B, find G_H and G_E, respectively, from Figures 13.17 and 13.9. If the values of either A or B or both are smaller than 2, then calculate G_E and/or G_H by

$$G_E = \frac{32}{\pi} B \tag{13-54c}$$

$$G_H = \frac{32}{\pi} A \tag{13-54d}$$

3. Calculate D_p by using the values of G_E and G_H from Figures 13.9 and 13.17 or from (13-54c) and (13-54d). Thus

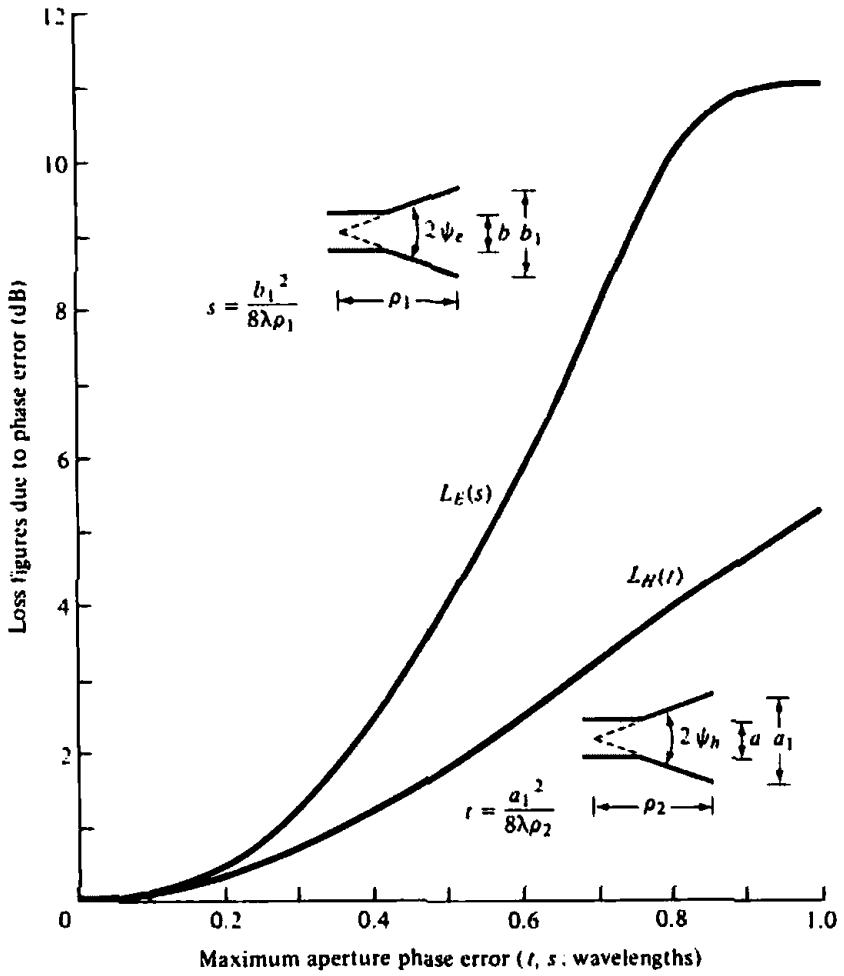

Figure 13.23 Loss figures for E- and H-planes due to phase errors. (SOURCE: W. C. Jakes, in H. Jasik (ed.), *Antenna Engineering Handbook*, McGraw-Hill, New York, 1961)

$$D_p = \frac{G_E G_H}{\frac{32}{\pi}\sqrt{\frac{50}{\rho_e/\lambda}}\sqrt{\frac{50}{\rho_h/\lambda}}} = \frac{G_E G_H}{10.1859\sqrt{\frac{50}{\rho_e/\lambda}}\sqrt{\frac{50}{\rho_h/\lambda}}} = \frac{\lambda^2\pi}{32ab} D_E D_H \tag{13-54e}$$

where D_E and D_H are, respectively, the directivities of (13-20c) and (13-42c). This is the actual directivity of the horn. The above procedure has led to results accurate to within 0.01 dB for a horn with $\rho_e = \rho_h = 50\lambda$.

A commercial X-band (8.2–12.4 GHz) horn is that shown in Figure 13.24. It is a lightweight precision horn antenna, which is usually cast of aluminum, and it can be used as a

1. standard for calibrating other antennas
2. feed for reflectors and lenses
3. pickup (probe) horn for sampling power
4. receiving and/or transmitting antenna

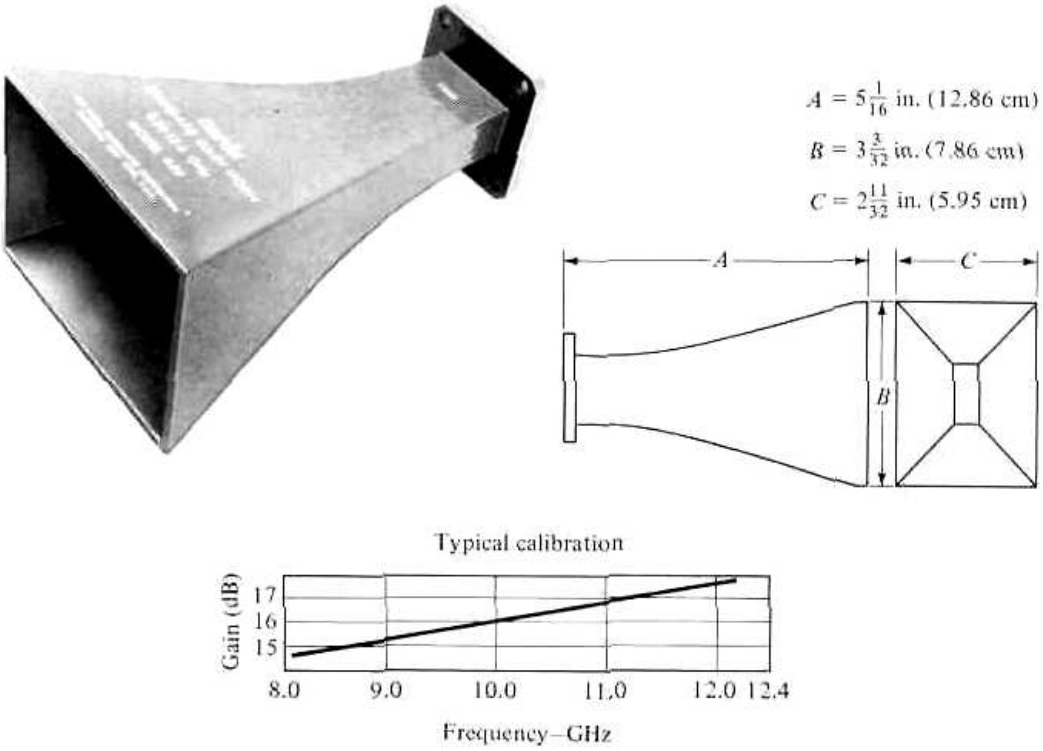

Figure 13.24 Typical standard gain X-band (8.2–12.4 GHz) pyramidal horn and its gain characteristics (courtesy of The NARDA Microwave Corporation).

It possesses an exponential taper, and its dimensions and typical gain characteristics are indicated in the figure. The half-power beamwidth in both the E- and H-planes is about 28° while the side lobes in the E- and H-planes are, respectively, about 13 and 20 dB down.

Gains of the horn antenna which were measured, predicted and provided by the manufacturer, whose amplitude patterns are shown in Figure 13.22, are displayed in Figure 13.25. A very good agreement amongst all three sets is indicated.

Example 13.5

A pyramidal horn has dimensions of $\rho_1 = \rho_2 = 6\lambda$, $a_1 = 5.5\lambda$, $b_1 = 2.75\lambda$, $a = 0.5\lambda$, and $b = 0.25\lambda$.

(a) Check to see if such a horn can be constructed physically.

(b) Compute the directivity using (13-52a), (13-53), and (13-54e).

SOLUTION

From Examples 13.3 and 13.4.

$$\rho_e = 6.1555\lambda$$
$$\rho_h = 6.6\lambda$$

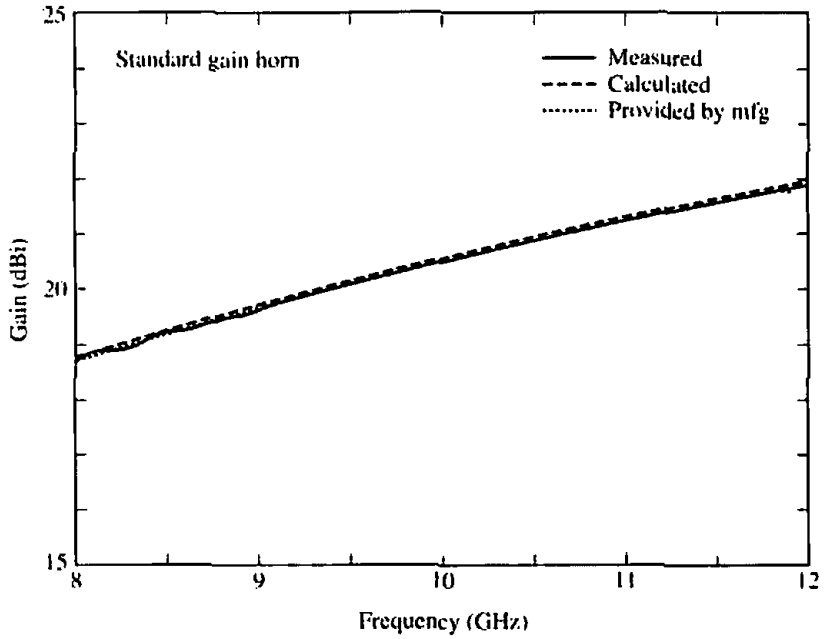

Figure 13.25 Gains of the pyramidal horn which were measured, computed and provided by the manufacturer. The amplitude patterns of the horn are shown in Figure 13.22.

Thus

$$\rho_e = (2.75 - 0.25)\lambda \sqrt{\left(\frac{6.1555}{2.75}\right)^2 - \frac{1}{4}} = 5.454\lambda$$

$$\rho_h = (5.5 - 0.5)\lambda \sqrt{\left(\frac{6}{5.5}\right)^2 - \frac{1}{4}} = 5.454\lambda$$

Therefore the horn can be constructed physically.

The directivity can be computed by utilizing the results of Examples 13.3 and 13.4. Using (13-52a) with the values of D_E and D_H computed using, respectively, (13-19) and (13-41) gives

$$D_0 = \frac{\pi\lambda^2}{32ab} D_E D_H = \frac{\pi}{32(0.5)(0.25)} (12.79)(7.52) = 75.54 = 18.78 \text{ dB}$$

Utilizing the values of D_E and D_H computed using, respectively, (13-20c) and (13-42c), the directivity of (13-54e) is equal to

$$D_0 = \frac{\pi\lambda^2}{32ab} D_E D_H = \frac{\pi}{32(0.5)0.25} (12.89)(8.338) = 84.41 = 19.26 \text{ dB}$$

For this horn

$$s = \frac{b_1^2}{8\lambda\rho_1} = \frac{(2.75)^2}{8(6)} = 0.1575$$

$$t = \frac{a_1^2}{8\lambda\rho_2} = \frac{(5.5)^2}{8(6)} = 0.63$$

For these values of s and t

$$L_E = 0.20 \text{ dB}$$
$$L_H = 2.75 \text{ dB}$$

from Figure 13.23. Using (13-53)

$$D_p = 10\{1.008 + \log_{10}[5.5(2.75)]\} - (0.20 + 2.75) = 18.93 \text{ dB}$$

The agreement is best between the directivities of (13-52a) and (13-53).

A computer program entitled PYRAMIDAL HORN-ANALYSIS has been developed to analyze the radiation characteristics of a pyramidal horn and the directivities of the corresponding E- and H-plane sectoral horns. The program is found at the end of this chapter.

13.4.3 Design Procedure

The pyramidal horn is widely used as a standard to make gain measurements of other antennas (see Section 16.4, Chapter 16), and as such it is often referred to as a *standard gain horn*. To design a pyramidal horn, one usually knows the desired gain G_0 and the dimensions a, b of the rectangular feed waveguide. The objective of the design is to determine the remaining dimensions (a_1, b_1, ρ_e, ρ_h, p_e, and p_h) that will lead to an optimum gain. The procedure that follows can be used to accomplish this [2], [3].

The design equations are derived by first selecting values of b_1 and a_1 that lead, respectively, to optimum directivities for the E- and H-plane sectoral horns using (13-19a) and (13-41c). Since the overall efficiency (including both the antenna and aperture efficiencies) of a horn antenna is about 50% [2], [3], the gain of the antenna can be related to its physical area. Thus it can be written using (12-39c), (12-40), and (13-19a), (13-41c) as

$$G_0 = \frac{1}{2}\frac{4\pi}{\lambda^2}(a_1 b_1) = \frac{2\pi}{\lambda^2}\sqrt{3\lambda\rho_2}\sqrt{2\lambda\rho_1} \simeq \frac{2\pi}{\lambda^2}\sqrt{3\lambda\rho_h}\sqrt{2\lambda\rho_e} \tag{13-55}$$

since for long horns $\rho_2 \simeq \rho_h$ and $\rho_1 \simeq \rho_e$. For a pyramidal horn to be physically realizable, p_e and p_h of (13-49a) and (13-49b) must be equal. Using this equality, it can be shown that (13-55) reduces to

$$\boxed{\left(\sqrt{2\chi} - \frac{b}{\lambda}\right)^2 (2\chi - 1) = \left(\frac{G_0}{2\pi}\sqrt{\frac{3}{2\pi}}\frac{1}{\sqrt{\chi}} - \frac{a}{\lambda}\right)^2 \left(\frac{G_0^2}{6\pi^3}\frac{1}{\chi} - 1\right)} \tag{13-56}$$

where

$$\boxed{\frac{\rho_e}{\lambda} = \chi} \tag{13-56a}$$

$$\boxed{\frac{\rho_h}{\lambda} = \frac{G_0^2}{8\pi^3}\left(\frac{1}{\chi}\right)} \tag{13-56b}$$

Equation (13-56) is the horn design equation.

1. As a first step of the design, find the value of χ which satisfies (13-56) for a desired gain G_0 (dimensionless). Use an iterative technique and begin with a trial value of

$$\chi\,(\text{trial}) = \chi_1 = \frac{G_0}{2\pi\sqrt{2\pi}} \tag{13-57}$$

2. Once the correct χ has been found, determine ρ_e and ρ_h using (13-56a) and (13-56b), respectively.
3. Find the corresponding values of a_1 and b_1 using (13-19a) and (13-41c) or

$$a_1 = \sqrt{3\lambda\rho_2} \simeq \sqrt{3\lambda\rho_h} = \frac{G_0}{2\pi}\sqrt{\frac{3}{2\pi\chi}}\,\lambda \tag{13-58a}$$

$$b_1 = \sqrt{2\lambda\rho_1} \simeq \sqrt{2\lambda\rho_e} = \sqrt{2\chi}\lambda \tag{13-58b}$$

4. The values of ρ_e and ρ_h can be found using (13-49a) and (13-49b).

A computer program entitled PYRAMIDAL HORN-DESIGN has been developed to accomplish this, and it is found at the end of this chapter.

Example 13.6

Design an optimum gain X-band (8.2–12.4 GHz) pyramidal horn so that its gain (above isotropic) at $f = 11$ GHz is 22.6 dB. The horn is fed by a WR 90 rectangular waveguide with inner dimensions of $a = 0.9$ in. (2.286 cm) and $b = 0.4$ in. (1.016 cm).

SOLUTION

Convert the gain G_0 from dB to a dimensionless quantity. Thus

$$G_0\,(\text{dB}) = 22.6 = 10\log_{10}G_0 \Rightarrow G_0 = 10^{2.26} = 181.97$$

Since $f = 11$ GHz, $\lambda = 2.7273$ cm and

$$a = 0.8382\lambda$$
$$b = 0.3725\lambda$$

1. The initial value of χ is taken, using (13-57), as

$$\chi_1 = \frac{181.97}{2\pi\sqrt{2\pi}} = 11.5539$$

which does not satisfy (13-56) for the desired design specifications. After a few iterations, a more accurate value is $\chi = 11.1157$.

2. *Using (13-56a) and (13-56b)*

$$\rho_e = 11.1157\lambda = 30.316 \text{ cm} = 11.935 \text{ in.}$$
$$\rho_h = 12.0094\lambda = 32.753 \text{ cm} = 12.895 \text{ in.}$$

3. The corresponding values of a_1 and b_1 are

$$a_1 = 6.002\lambda = 16.370 \text{ cm} = 6.445 \text{ in.}$$
$$b_1 = 4.715\lambda = 12.859 \text{ cm} = 5.063 \text{ in.}$$

4. The values of p_e and p_h are equal to

$$p_e = p_h = 10.005\lambda = 27.286 \text{ cm} = 10.743 \text{ in.}$$

The same values are obtained using the computer program at the end of this chapter.

The derived design parameters agree closely with those of a commercial gain horn available in the market. As a check, the gain of the designed horn was computed using (13-52a) and (13-53), assuming an antenna efficiency e_t of 100%, and (13-55). The values were

$$G_0 \simeq D_0 \simeq 22.4 \text{ dB} \quad \text{for (13-52a)}$$
$$G_0 \simeq D_0 = 22.1 \text{ dB} \quad \text{for (13-53)}$$
$$G_0 = 22.5 \text{ dB} \quad \text{for (13-55)}$$

All three computed values agree closely with the designed value of 22.6 dB.

13.5 CONICAL HORN

Another very practical microwave antenna is the conical horn shown in Figure 13.26. While the pyramidal, E-, and H-plane sectoral horns are usually fed by a rectangular waveguide, the feed of a conical horn is often a circular waveguide.

The first rigorous treatment of the fields radiated by a conical horn is that of Schorr and Beck [20]. The modes within the horn are found by introducing a spherical coordinate system and are in terms of spherical Bessel functions and Legendre polynomials. The analysis is too involved and will not be attempted here. However data, in the form of curves [21], will be presented which give a qualitative description of the performance of a conical horn.

Referring to Figure 13.27, it is apparent that the behavior of a conical horn is similar to that of a pyramidal or a sectoral horn. As the flare angle increases, the directivity for a given length horn increases until it reaches a maximum beyond which it begins to decrease. The decrease is a result of the dominance of the quadratic phase error at the aperture. In the same figure, an optimum directivity line is indicated.

The results of Figure 13.27 behave as those of Figures 13.8 and 13.16. When the horn aperture (d_m) is held constant and its length (L) is allowed to vary, the maximum directivity is obtained when the flare angle is zero ($\psi_c = 0$ or $L = \infty$). This is equivalent to a circular waveguide of diameter d_m. As for the pyramidal and sectoral horns, a lens is usually placed at the aperture of the conical horn to compensate for its quadratic phase error. The result is a narrower pattern as its flare increases.

The directivity (in dB) of a conical horn, with an aperture efficiency of ϵ_{ap} and aperture circumference C, can be computed using

$$D_c \text{ (dB)} = 10\log_{10}\left[\epsilon_{ap}\frac{4\pi}{\lambda^2}(\pi a^2)\right] = 10\log_{10}\left(\frac{C}{\lambda}\right)^2 - L(s) \tag{13-59}$$

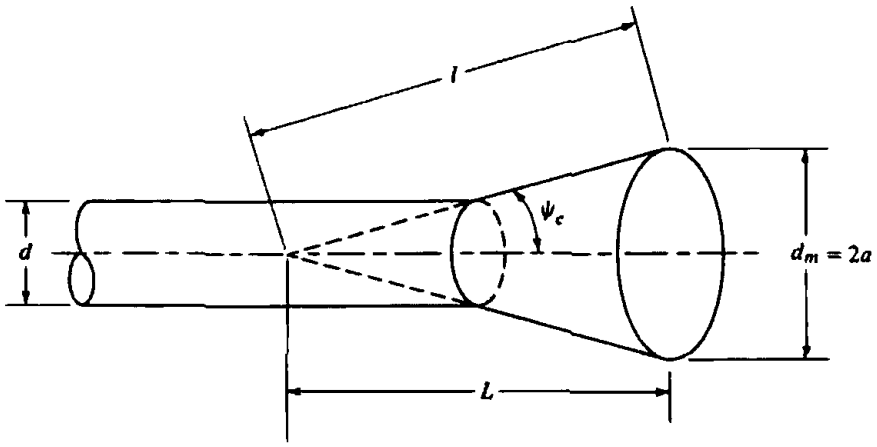

Figure 13.26 Geometry of conical horn.

where a is the radius of horn at the aperture and

$$\boxed{L(s) = -10\log_{10}(\epsilon_{ap})} \tag{13-59a}$$

The first term in (13-59) represents the directivity of a uniform circular aperture whereas the second term, represented by (13-59a), is a correction figure to account for the loss in directivity due to the aperture efficiency. Usually the term in (13-59a) is referred to as *loss figure* which can be computed (in decibels) using [2], [3]

$$L(s) \simeq (0.8 - 1.71s + 26.25s^2 - 17.79s^3) \tag{13-59b}$$

where s is the maximum phase deviation (in number of wavelengths), and it is given by

$$s = \frac{d_m^2}{8\lambda l} \tag{13-59c}$$

The directivity of a conical horn is optimum when its diameter is equal to

$$\boxed{d_m \simeq \sqrt{3l\lambda}} \tag{13-60}$$

which corresponds to a maximum aperture phase deviation of $s = 3/8$ (wavelengths) and a loss figure of about 2.9 dB (or an aperture efficiency of about 51%).

13.6 CORRUGATED HORN

The large emphasis placed on horn antenna research in the 1960s was inspired by the need to reduce spillover efficiency and cross-polarization losses and increase aperture efficiencies of large reflectors used in radio astronomy and satellite communications. In the 1970s high-efficiency and rotationally symmetric antennas were needed in microwave radiometry. Using conventional feeds, aperture efficiencies of 50–60% were obtained. However, efficiencies of the order of 75–80% can be obtained with improved feed systems utilizing corrugated horns.

The aperture techniques introduced in Chapter 12 can be used to compute the pattern of a horn antenna and would yield accurate results only around the main lobe and the first few minor lobes. The antenna pattern structure in the back lobe region is strongly influenced by diffractions from the edges, especially from those that are perpendicular to the E-field at the horn aperture. The diffractions lead to undesirable

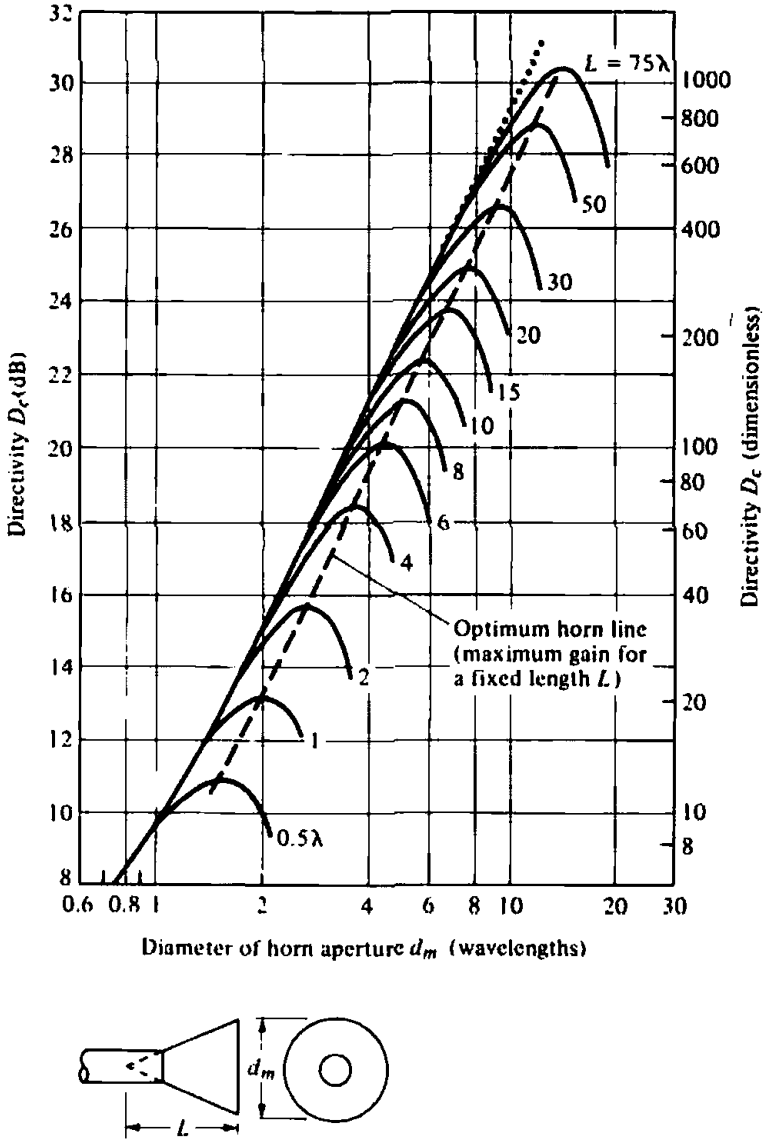

Figure 13.27 Directivity of a conical horn as a function of aperture diameter and for different axial horn lengths. (SOURCE: A. P. King, "The Radiation Characteristics of Conical Horn Antennas," *Proc. IRE*, Vol. 38, pp. 249–251, March 1950. © (1950) IEEE)

radiation not only in the back lobes but also in the main lobe and in the minor lobes. However, they dominate only in low-intensity regions.

In 1964 Kay [22] realized that grooves on the walls of a horn antenna would present the same boundary conditions to all polarizations and would taper the field distribution at the aperture in all the planes. The creation of the same boundary conditions on all four walls would eliminate the spurious diffractions at the edges of the aperture. For a square aperture, this would lead to an almost rotationally symmetric pattern with equal E- and H-plane beamwidths. A *corrugated (grooved)* pyramidal horn, with corrugations in the E-plane walls, is shown in Figure 13.28(a) with a side view in Figure 13.28(b). Since diffractions at the edges of the aperture in the H-plane are minimal, corrugations are usually not placed on the walls of that plane. Corrugations can also be placed in a conical horn forming a *conical corrugated* horn, also referred to in [22] as *scalar horn*. However, instead of the corrugations being formed as shown in Figure 13.29(a), practically it is much easier to machine them to have the profile shown in Figure 13.29(b).

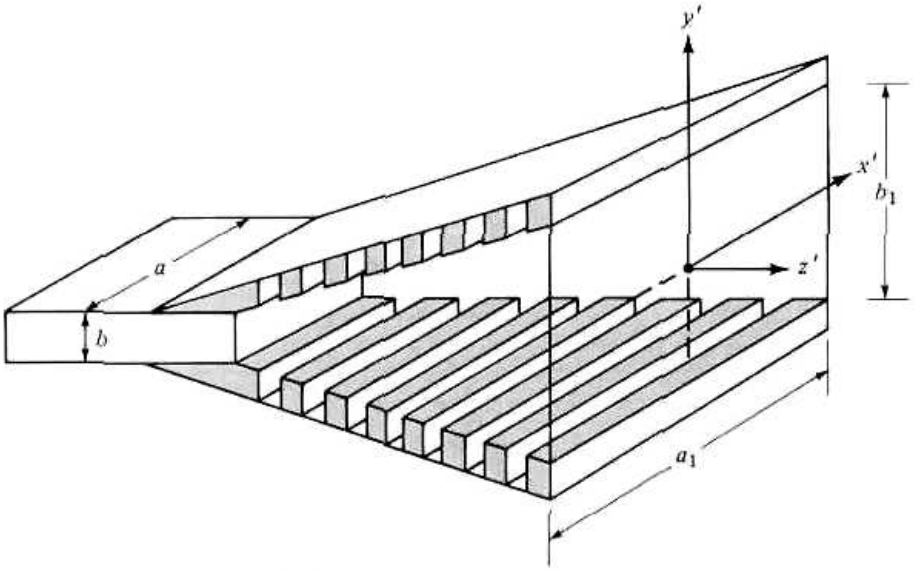

(a) Corrugated horn

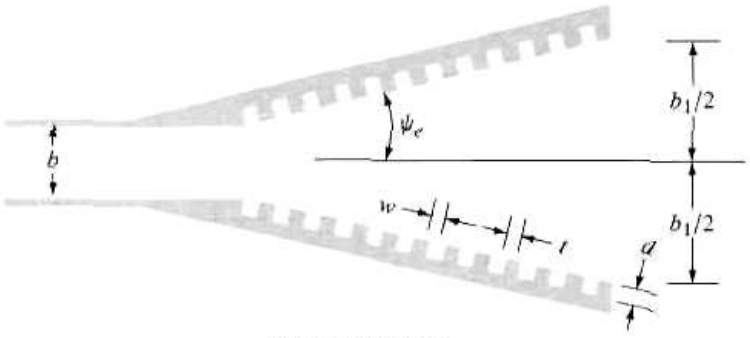

(b) *E*-plane view

Figure 13.28 Pyramidal horn with corrugations in the *E*-plane.

To form an effective corrugated surface, it usually requires 10 or more slots (corrugations) per wavelength [23]. To simplify the analysis of an infinite corrugated surface, the following assumptions are usually required:

1. The teeth of the corrugations are vanishingly thin.
2. Reflections from the base of the slot are only those of a TEM mode.

The second assumption is satisfied provided the width of the corrugation (w) is small compared to the free-space wavelength (λ_0) and the slot depth (d) (usually $w < \lambda_0/10$). For a corrugated surface satisfying the above assumptions, its approximate surface reactance is given by [24]

$$X = \frac{w}{w + t}\sqrt{\frac{\mu_0}{\epsilon_0}}\tan(k_0 d) \tag{13-61}$$

when

$$\frac{w}{w + t} \simeq 1 \tag{13-61a}$$

which can be satisfied provided $t \leq w/10$.

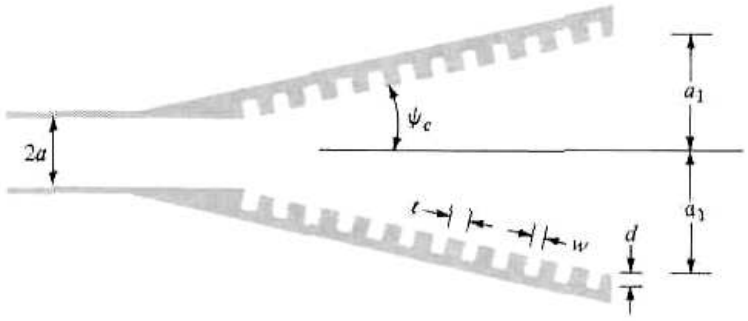

(a) Corrugations perpendicular to surface

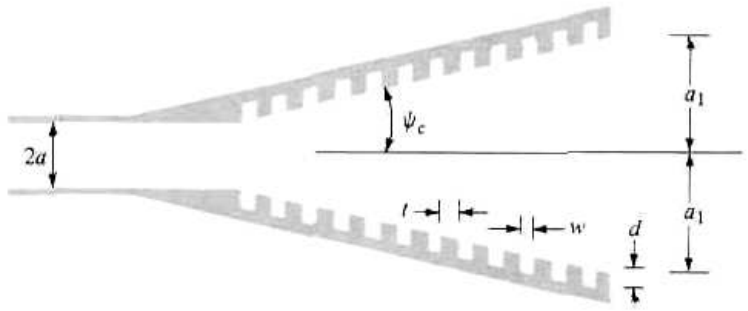

(b) Corrugations perpendicular to axis

Figure 13.29 Side view profiles of conical corrugated horns.

The surface reactance of a corrugated surface, used on the walls of a horn, must be capacitive in order for the surface to force to zero the tangential magnetic field parallel to the edge at the wall. Thus the surface will not support surface waves, will prevent illumination of the E-plane edges, and will diminish diffractions. This can be accomplished, according to (13-61), if $\lambda_0/4 < d < \lambda_0/2$ or more generally when $(2n + 1)\lambda_0/4 < d < (n + 1)\lambda_0/2$. Even though the cutoff depth is also a function of the slot width w, its influence is negligible if $w < \lambda_0/10$ and $\lambda_0/4 < d < \lambda_0/2$.

To study the performance of a corrugated surface, an analytical model was developed and parametric studies were performed [25]. Although the details are numerous, only the results will be presented here. In Figure 13.30(a) a corrugated surface is sketched and in Figure 13.30(b) its corresponding uncorrugated counterpart is shown.

For a free-space wavelength of $\lambda_0 = 8$ cm, the following have been plotted for point B in Figure 13.30(a) relative to point A in Figure 13.30(b):

1. In Figure 13.31(a) the surface current density decay at B relative to that at $A[J_s(B)/J_s(A)]$ as a function of corrugation number (for 20 total corrugations) due to energy being forced away from the corrugations. As expected, no decay occurs for $d = 0.5\lambda_0$ and the most rapid decay is obtained for $d = 0.25\lambda_0$.
2. In Figure 13.31(b) the surface current density decay at B relative to that in $A[J_s(B)/J_s(A)]$ as a function of the distance z from the onset of the corrugations for four and eight corrugations per wavelength. The results indicate an almost independence of current density decay as a function of corrugation density for the cases considered.
3. In Figure 13.31(c) the surface current density decay at B relative to that in $A[J_s(B)/J_s(A)]$ as a function of the distance z from the onset of the corrugations

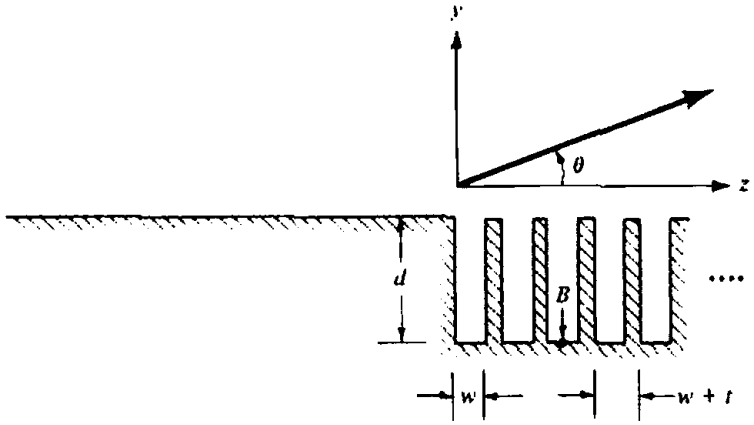

(a) Corrugated surface

(b) Noncorrugated surface

Figure 13.30 Geometry of corrugated and plane surfaces. (SOURCE: C. A. Mentzer and L. Peters, Jr., "Properties of Cutoff Corrugated Surfaces for Corrugated Horn Design," *IEEE Trans. Antennas Propagat.*, Vol. AP-22, No. 2, March 1974. © (1974) IEEE)

for $w/(w + t)$ ratios ranging from 0.5 to 0.9. For $z < 4$ cm $\approx \lambda_0/2$, thinner corrugations [larger $w/(w + t)$ ratios] exhibit larger rates of decay. Beyond that point, the rate of decay is approximately constant. This would indicate that in a practical design thinner corrugations can be used at the onset followed by thicker ones, which are easier to construct.

The effect of the corrugations on the walls of a horn is to modify the electric field distribution in the E-plane from uniform (at the waveguide-horn junction) to cosine (at the aperture). Through measurements, it has been shown that the transition from uniform to cosine distribution takes place almost at the onset of the corrugations. For a horn of about 45 corrugations, the cosine distribution has been established by the fifth corrugation (from the onset) and the spherical phase front by the fifteenth [26]. The E- and H-plane amplitude and phase distributions at the aperture of the horn with 45 corrugations are shown in Figure 13.32(a,b). It is clear that the cosine distribution is well established.

Referring to Figure 13.28(a), the field distribution at the aperture can be written as

$$E_x'(x', y') = E_0 \cos\left(\frac{\pi}{a_1}x'\right) \cos\left(\frac{\pi}{b_1}y'\right) e^{-j[k(x'^2/\rho_2 + y'^2/\rho_1)/2]} \tag{13-62a}$$

$$H_y'(x', y') = -\frac{E_0}{\eta} \cos\left(\frac{\pi}{a_1}x'\right) \cos\left(\frac{\pi}{b_1}y'\right) e^{-j[k(x'^2/\rho_2 + y'^2/\rho_1)/2]} \tag{13-62b}$$

corresponding to (13-43a) and (13-43b) of the uncorrugated pyramidal horn. Using the above distributions, the fields radiated by the horn can be computed in a manner analogous to that of the pyramidal horn of Section 13.4. Patterns have been computed and compare very well with measurements [26].

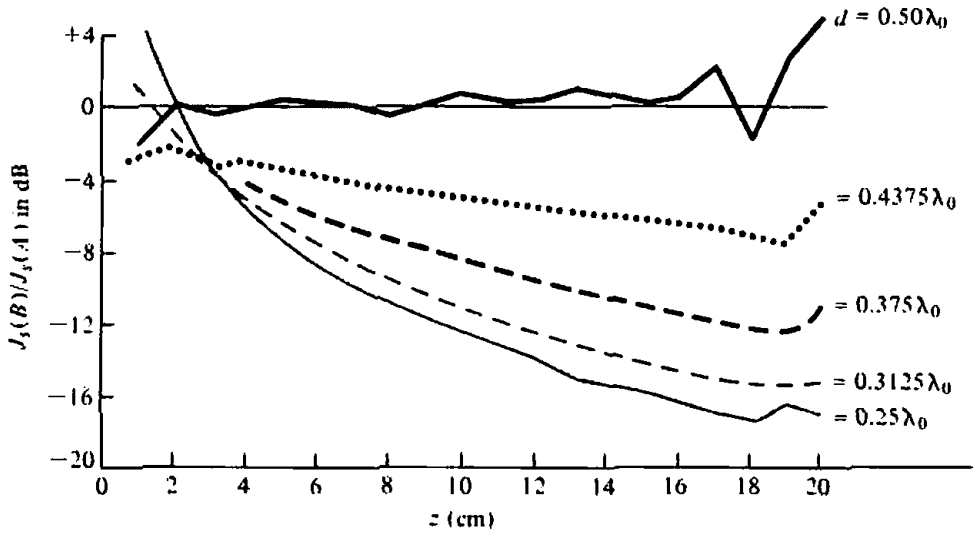

(a) Surface current decay on corrugated surface due to energy forced away from corrugations.

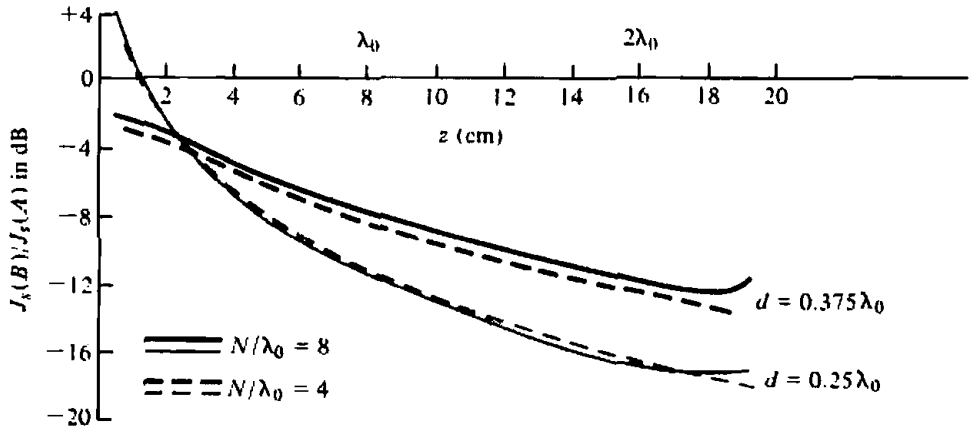

(b) Surface current decay on corrugations as a function of corrugation density.

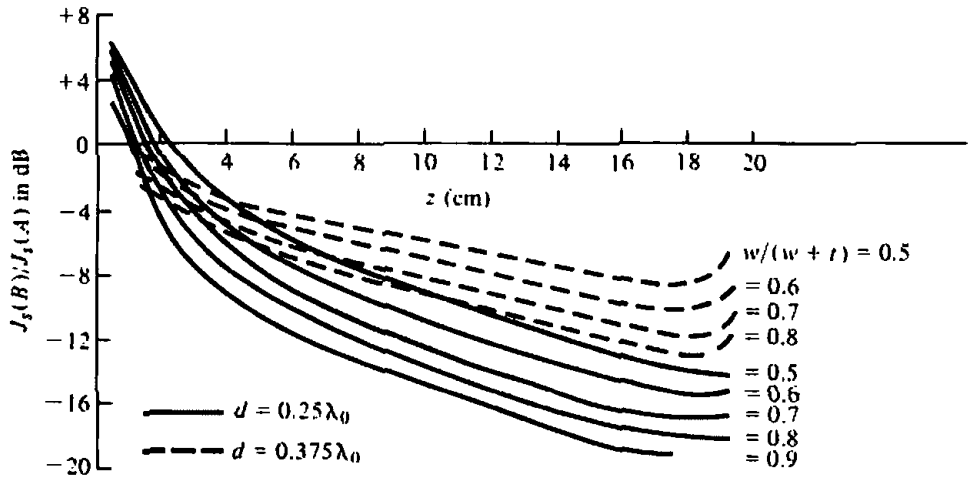

(c) Surface current decay on corrugations as a function of corrugation shape.

Figure 13.31 Surface current decays on corrugated surface. (SOURCE: C. A. Mentzer and L. Peters, Jr., "Properties of Cutoff Corrugated Surfaces for Corrugated Horn Design," *IEEE Trans. Antennas Propagat.*, Vol. AP-22, No. 2, March 1974. © (1974) IEEE)

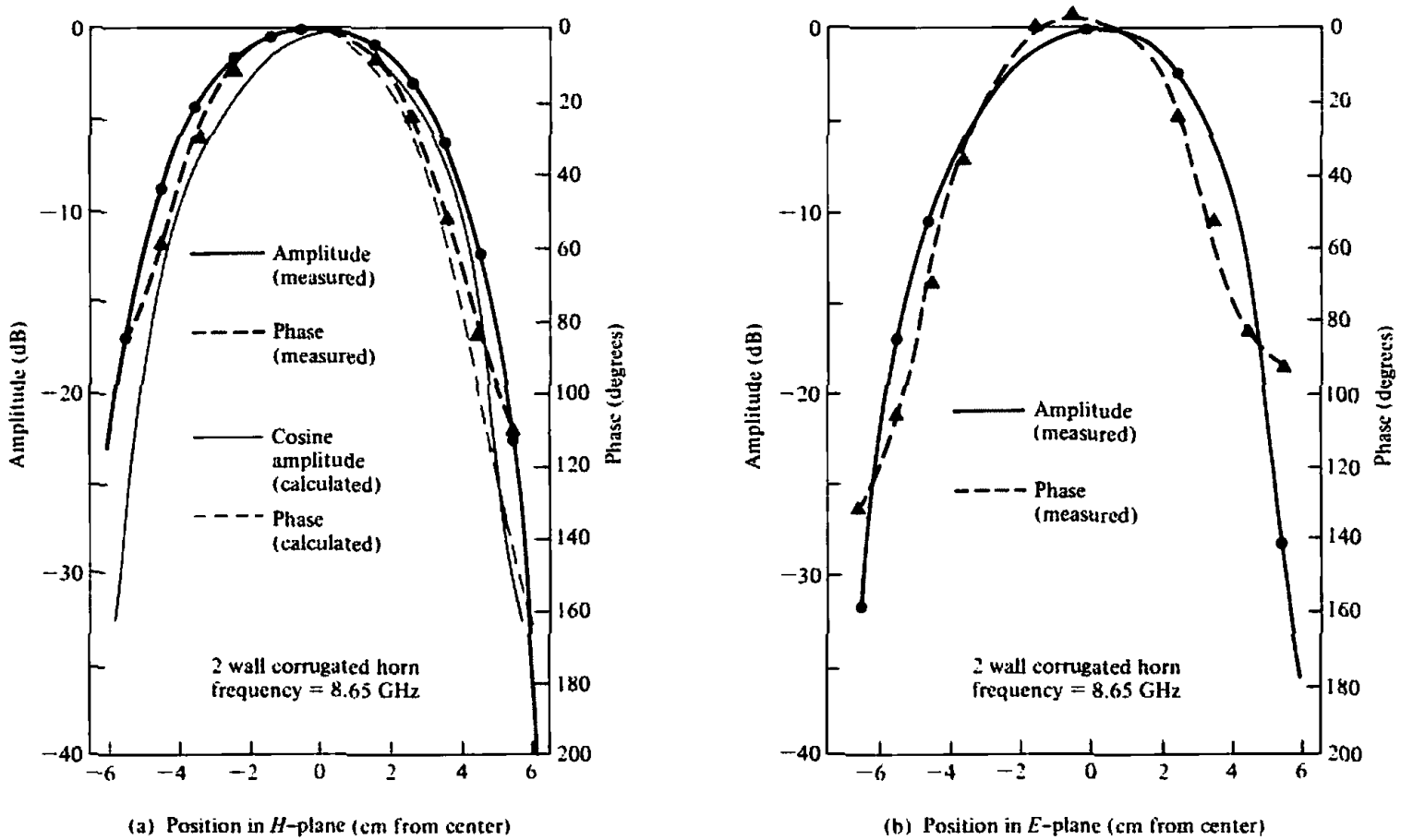

Figure 13.32 Amplitude and phase distributions in *H*- and *E*-planes. (SOURCE: C. A. Mentzer and L. Peters, Jr., "Pattern Analysis of Corrugated Horn Antennas," *IEEE Trans. Antennas Propagat.*, Vol. AP-24, No. 3, May 1976. © (1976) IEEE)

In Figure 13.33(a) the measured E-plane patterns of an uncorrugated square pyramidal horn (*referred to as the control horn*) and a corrugated square pyramidal horn are shown. The aperture size on each side was 3.5 in. (2.96λ at 10 GHz) and the total flare angle in each plane was 50°. It is evident that the levels of the minor lobes and back lobes are much lower for the corrugated horn than those of the control horn. However the corrugated horn also exhibits a wider main beam for small angles: thus a larger 3-dB beamwidth (HPBW) but a lower 10-dB beamwidth. This is attributed to the absence of the diffracted fields from the edges of the corrugated horn which, for nearly on-axis observations, add to the direct wave contribution because of their in-phase relationship. The fact that the on-axis far-fields of the direct and diffracted fields are nearly in-phase is also evident from the pronounced on-axis maximum of the control horn. The E- and H-plane patterns of the corrugated horn are almost identical to those of Figure 13.33(a) over the frequency range from 8 to 14 GHz. These suggest that the main beam in the E-plane can be obtained from known H-plane patterns of horn antennas.

In Figure 13.33(b) the measured E-plane patterns of larger control and corrugated square pyramidal horns, having an aperture of 9.7 in. on each side (8.2λ at 10 GHz) and included angles of 34° and 31° in the E- and H-planes, respectively, are shown. For this geometry, the pattern of the corrugated horn is narrower and its minor and back lobes are much lower than those of the corresponding control horn. The saddle formed on the main lobe of the control horn is attributed to the out-of-phase relations between the direct and diffracted rays. The diffracted rays are nearly absent from the corrugated horn and the minimum on-axis field is eliminated. The control horn is a thick-edged horn which has the same interior dimensions as the corrugated horn. The H-plane pattern of the corrugated horn is almost identical to the H-plane pattern of the corresponding control horn.

In Figures 13.33(c) and 13.33(d) the back lobe level and the 3-dB beamwidth for the smaller size control and corrugated horns, whose E-plane patterns are shown in Figure 13.33(a), are plotted as a function of frequency. All the observations made previously for that horn are well evident in these figures.

The presence of the corrugations, especially near the waveguide-horn junction, can affect the impedance and VSWR of the antenna. The usual practice is to begin the corrugations at a small distance away from the junction. This leads to low VSWR's over a broad band. Previously it was indicated that the width w of the corrugations must be small (usually $w < \lambda_0/10$) to approximate a corrugated surface. This would cause corona and other breakdown phenomena. However the large corrugated horn, whose E-plane pattern is shown in Figure 13.33(b), has been used in a system whose peak power was 20 kW at 10 GHz with no evidence of any breakdown phenomena.

The design concepts of the pyramidal corrugated horn can be extended to include circumferentially corrugated conical horns, as shown in Figure 13.29. Several designs of conical corrugated horns were investigated in terms of pattern symmetry, low cross polarization, low side lobe levels, circular polarization, axial ratio, and phase center [27]–[36]. For small flare angles (ψ_0 less than about 20° to 25°) the slots can be machined perpendicular to the axis of the horn, as shown in Figure 13.29(b), and the grooves can be considered sections of parallel-plate TEM-mode waveguides of depth d. For large flare angles, however, the slots should be constructed perpendicular to the surface of the horn, as shown in Figure 13.29(a). The groove arrangement of Figure 13.29(b) is usually preferred because it is easier to fabricate.

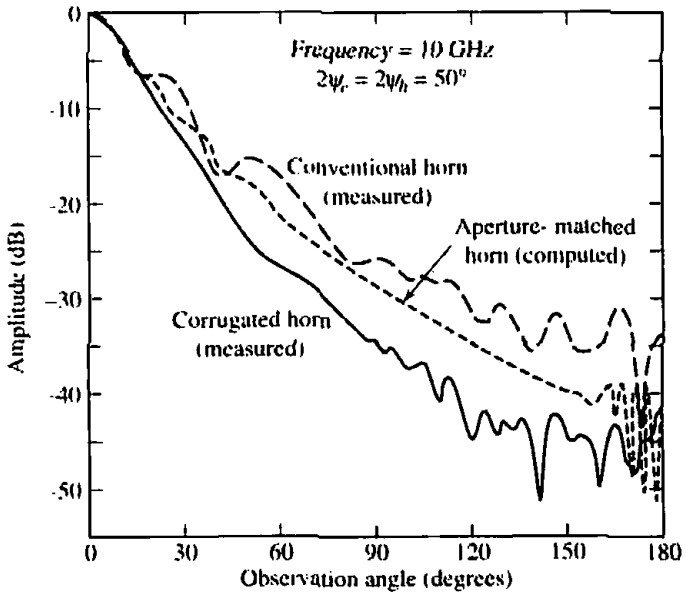

(a) E-plane ($2.96\lambda \times 2.96\lambda$)

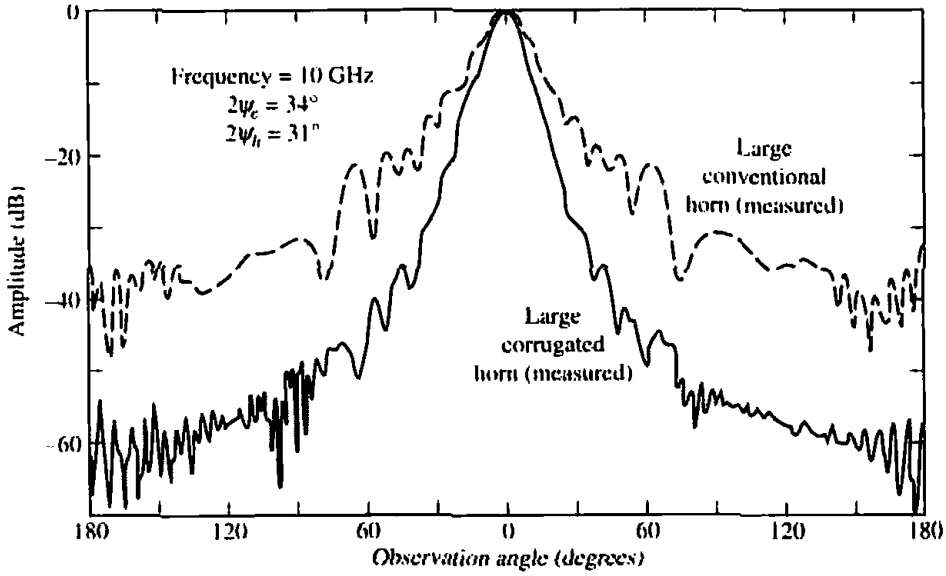

(b) E-plane ($8.2\lambda \times 8.2\lambda$)

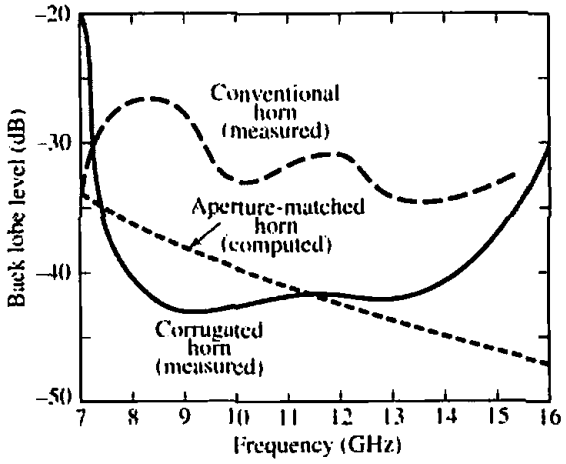

(c) E-plane back lobe level ($2.96\lambda \times 2.96\lambda$)

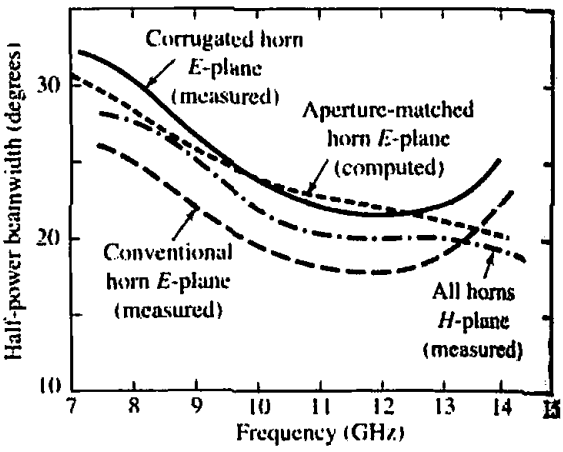

(d) E-plane half-power beamwidth ($2.96\lambda \times 2.96\lambda$)

Figure 13.33 Radiation characteristics of conventional (control), corrugated, and aperture-matched pyramidal horns. (SOURCE: (a), (c), (d). W. D. Burnside and C. W. Chuang, "An Aperture-Matched Horn Design," *IEEE Trans. Antennas Propagat.*, Vol. AP-30, No. 4, pp. 790–796, July 1982. © (1982) IEEE. (b) R. E. Laurie and L. Peters, Jr., "Modifications of Horn Antennas for Low Side Lobe Levels," *IEEE Trans. Antennas Propagat.*, Vol. AP-14, No. 5, pp. 605–610, September 1966. © (1966) IEEE)

13.7 APERTURE-MATCHED HORNS

A horn which provides significantly better performance than an ordinary horn (in terms of pattern, impedance, and frequency characteristics) is that shown in Figure 13.34(a), which is referred to as an *aperture-matched* horn [37]. The main modification to the ordinary (conventional) horn, which we refer to here as the *control* horn, consists of the attachment of curved surface sections to the outside of the aperture edges, which reduces the diffractions that occur at the sharp edges of the aperture and provides smooth matching sections between the horn modes and the free-space radiation.

In contrast to the corrugated horn, which is complex and costly and reduces the diffractions at the edges of the aperture by minimizing the incident field, the aperture-matched horn reduces the diffractions by modifying the structure (without sacrificing size, weight, bandwidth, and cost) so that the diffraction coefficient is minimized. The basic concepts were originally investigated using elliptic cylinder sections, as shown in Figure 13.34(b); however, other convex curved surfaces, which smoothly blend to the ordinary horn geometry at the attachment point, will lead to similar improvements. This modification in geometry can be used in a wide variety of horns, and includes *E*-plane, *H*-plane, pyramidal, and conical horns. Bandwidths of 2:1 can be attained easily with aperture-matched horns having elliptical, circular, or other curved surfaces. The radii of curvature of the curved surfaces used in experimental models [37] ranged over $1.69\lambda \leq a \leq 8.47\lambda$ with $a = b$ and $b = 2a$. Good results can be obtained by using circular cylindrical surfaces with $2.5\lambda \leq a \leq 5\lambda$.

The basic radiation mechanism of such a horn is shown in Figure 13.34(c). The introduction of the curved sections at the edges does not eliminate diffractions; instead it substitutes edge diffractions by curved-surface diffractions which have a tendency to provide an essentially undisturbed energy flow across the junction, around the curved surface, and into free space. Compared with conventional horns, this radiation mechanism leads to smoother patterns with greatly reduced black lobes and negligible reflections back into the horn. The size, weight, and construction costs of the aperture-matched horn are usually somewhat larger and can be held to a minimum if half (one-half sections of an ellipse) or quadrant (one-fourth sections of an ellipse) sections are used instead of the complete closed surfaces.

To illustrate the improvements provided by the aperture-matched horns, the *E*-plane pattern, back lobe level, and half-power beamwidth of a pyramidal $2.96\lambda \times 2.96\lambda$ horn were computed and compared with the measured data of corresponding control and corrugated horns. The data are shown in Figures 13.33 (a, c, d). It is evident by examining the patterns of Figure 13.33(a) that the aperture-matched horn provides a smoother pattern and lower back lobe level than conventional horns (referred to here as control horn); however, it does not provide, for the wide minor lobes, the same reduction as the corrugated horn. To achieve nearly the same *E*-plane pattern for all three horns, the overall horn size must be increased. If the modifications for the aperture-matched and corrugated horns were only made in the *E*-plane edges, the *H*-plane patterns for all three horns would be virtually the same except that the back lobe level of the aperture-matched and corrugated horns would be greatly reduced.

The back lobe level of the same three horns (control, corrugated, and aperture-matched) are shown in Figure 13.33(c). The corrugated horn has lower back lobe intensity at the lower end of the frequency band, while the aperture-matched horn exhibits superior performance at the high end. However, both the corrugated and aperture-matched horns exhibit superior back lobe level characteristics to the control

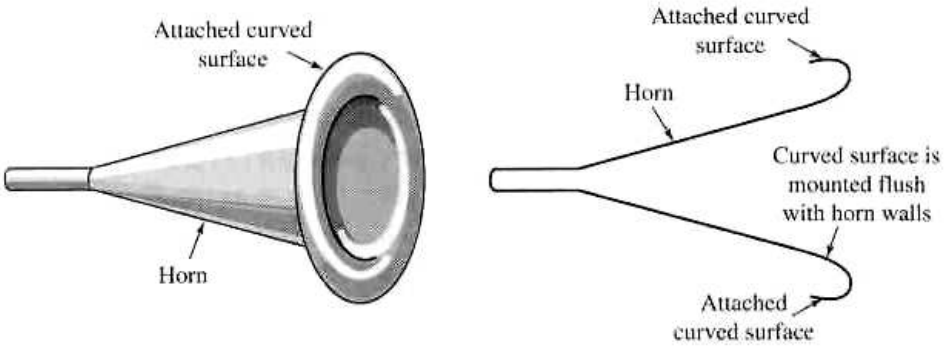

(a) Basic geometry

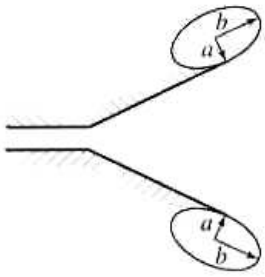

(b) Elliptical cylinder curved surface

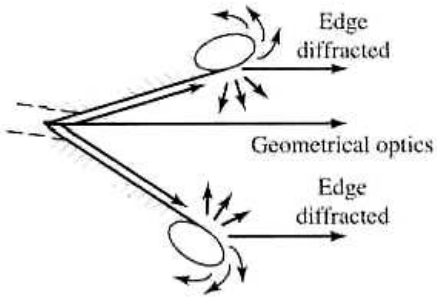

(c) Diffraction mechanism

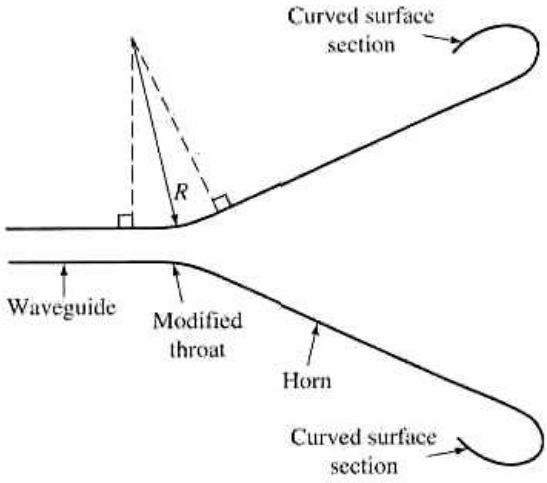

(d) Modified throat

Figure 13.34 Geometry and diffraction mechanism of an aperture-matched horn. (SOURCE: W. D. Burnside and C. W. Chuang, "An Aperture-Matched Horn Design," *IEEE Trans. Antennas Propagat.*, Vol. AP-30, No. 4, pp. 790–796, July 1982. © (1982) IEEE)

(conventional) horn throughout almost the entire frequency band. The half-power beamwidth characteristics of the same three horns are displayed in Figure 13.33(d). Because the control (conventional) horn has uniform distribution across the complete aperture plane, compared with the tapered distributions for the corrugated and aperture-matched horns, it possesses the smallest beamwidth almost over the entire frequency band.

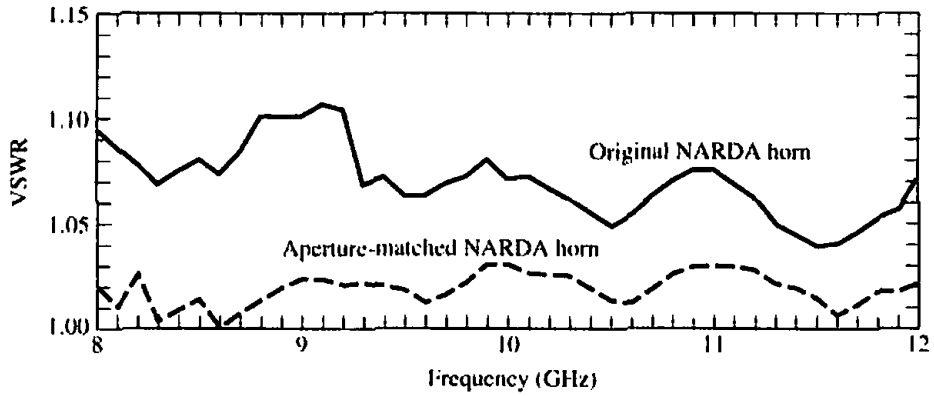

Figure 13.35 Measured VSWR for exponentially tapered pyramidal horns (conventional and aperture-matched). (SOURCE: W. D. Burnside and C. W. Chuang, "An Aperture-Matched Horn Design," *IEEE Trans. Antennas Propagat.*, Vol. AP-30, No. 4, pp. 790–796, July 1982. © (1982) IEEE)

In a conventional horn the VSWR and antenna impedance are primarily influenced by the throat and aperture reflections. Using the aperture-matched horn geometry of Figure 13.34(a), the aperture reflections toward the inside of the horn are greatly reduced. Therefore the only remaining dominant factors are the throat reflections. To reduce the throat reflections it has been suggested that a smooth curved surface be used to connect the waveguide and horn walls, as shown in Figure 13.34(d). Such a transition has been applied in the design and construction of a commerical *X*-band (8.2–12.4 GHz) pyramidal horn (see Fig. 13.24), whose tapering is of an exponential nature. The VSWR's measured in the 8-12 GHz frequency band using the conventional exponential *X*-band horn (shown in Figure 13.24), with and without curved sections at its aperture, are shown in Figure 13.35.

The matched sections used to create the aperture-matched horn were small cylinder sections. The VSWR's for the conventional horn are very small (less than 1.1) throughout the frequency band because the throat reflections are negligible compared with the aperture reflections. It is evident, however, that the VSWR's of the corresponding aperture-matched horn are much superior to those of the conventional horn because both the throat and aperture reflections are very minimal.

The basic design of the aperture-matched horn can be extended to include corrugations on its inside surface [29]. This type of design enjoys the advantages presented by both the aperture-matched and corrugated horns with cross-polarized components of less than -45 dB over a significant part of the bandwidth. Because of its excellent cross-polarization characteristics, this horn is recommended for use as a reference and for frequency reuse applications in both satellite and terrestrial applications.

13.8 MULTIMODE HORNS

Over the years there has been a need in many applications for horn antennas which provide symmetric patterns in all planes, phase center coincidence for the electric and magnetic planes, and side lobe suppression. All of these are attractive features for designs of optimum reflector systems and monopulse radar systems. Side lobe reduction is a desired attribute for horn radiators utilized in antenna range, anechoic cham-

ber, and standard gain applications, while pattern plane symmetry is a valuable feature for polarization diversity.

Pyramidal horns have traditionally been used over the years, with good success, in many of these applications. Such radiators, however, possess nonsymmetric beamwidths and undesirable side lobe levels, especially in the *E*-plane. Conical horns, operating in the dominant TE_{11} mode, have a tapered aperture distribution in the *E*-plane. Thus, they exhibit more symmetric electric- and magnetic-plane beamwidths and reduced side lobes than do the pyramidal horns. One of the main drawbacks of a conical horn is its relative incompatibility with rectangular waveguides.

To remove some of the deficiencies of pyramidal and conical horns and further improve some of their attractive characteristics, corrugations were introduced on the interior walls of the waveguides, which lead to the corrugated horns that were discussed in a previous section of this chapter. In some other cases designs were suggested to improve the beamwidth equalization in all planes and reduce side lobe levels by utilizing horn structures with multiple-mode excitations. These have been designated as *multimode* horns, and some of the designs will be discussed briefly here. For more information the reader should refer to the cited references.

One design of a multimode horn is the "diagonal" horn [38], shown in Figure 13.36, all of whose cross sections are square and whose internal fields consist of a superposition of TE_{10} and TE_{01} modes in a square waveguide. For small flare angles, the field structure within the horn is such that the **E**-field vector is parallel to one of the diagonals. Although it is not a multimode horn in the true sense of the word, because it does not make use of higher-order TE and TM modes, it does possess the desirable attributes of the usual multimode horns, such as equal beamwidths and suppressed beamwidths and side lobes in the *E*- and *H*-planes which are nearly equal to those in the principal planes. These attractive features are accomplished, however, at the expense of pairs of cross-polarized lobes in the intercardinal planes which make such a horn unattractive for applications where a high degree of polarization purity is required.

Diagonal horns have been designed, built, and tested [38] such that the 3-, 10-, and 30-dB beamwidths are nearly equal not only in the principal *E*- and *H*-planes, but also in the 45° and 135° planes. Although the theoretical limit of the side lobe level in the principal planes is 31.5 dB down, side lobes of at least 30 dB down have been observed in those planes. Despite a theoretically predicted level of -19.2 dB in the $\pm 45°$ planes, side lobes with level of -23 to -27 dB have been observed. The principal deficiency in the side lobe structure appears in the $\pm 45°$-plane cross-polarized lobes whose intensity is only 16 dB down; despite this, the overall horn efficiency remains high. Compared with diagonal horns, conventional pyramidal square horns have *H*-plane beamwidths which are about 35% wider than those in the *E*-plane, and side lobe levels in the *E*-plane which are only 12 to 13 dB down (although those in the *H*-plane are usually acceptable).

For applications which require optimum performance with narrow beamwidths, lenses are usually recommended for use in conjunction with diagonal horns. Diagonal horns can also be converted to radiate circular polarization by inserting a differential phase shifter inside the feed guide whose cross section is circular and adjusted so that it produces phase quadrature between the two orthogonal modes.

Another multimode horn which exhibits suppressed side lobes, equal beamwidths, and reduces cross-polarization is the *dual-mode* conical horn [39]. Basically this horn is designed so that diffractions at the aperture edges of the horn, especially those in the *E*-plane, are minimized by reducing the fields incident on the aperture edges and consequently the associated diffractions. This is accomplished by utilizing a conical

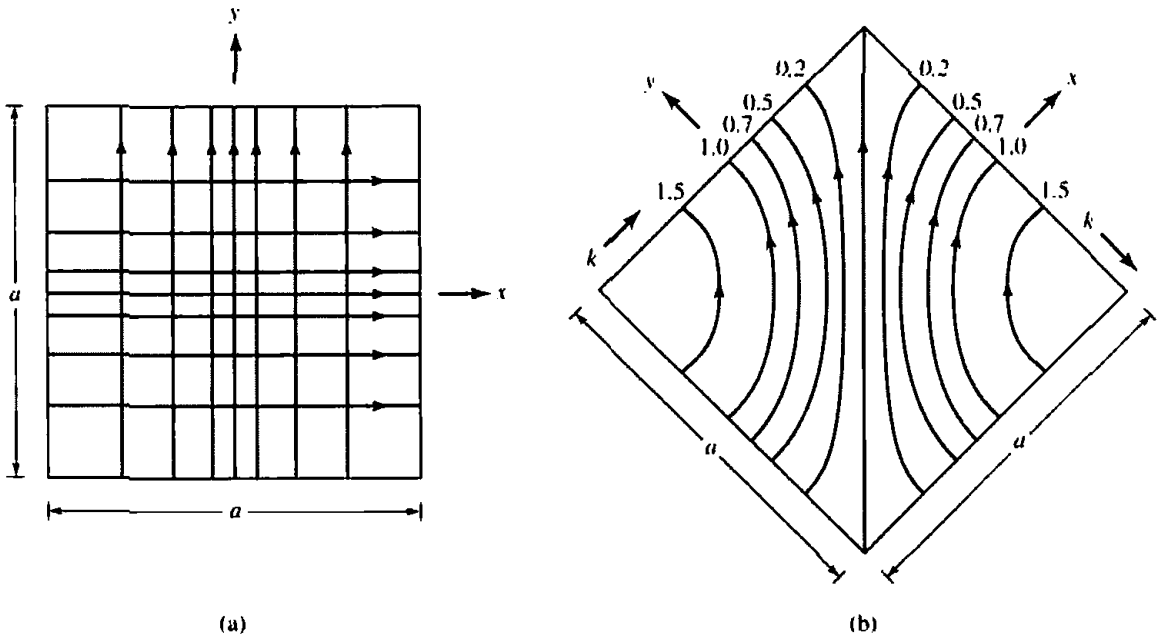

(a) (b)

Figure 13.36 Electric-field configuration inside square diagonal horn. (*a*) Two coexisting equal orthogonal modes. (*b*) Result of combining the two modes shown in (*a*). (*After Love* [38] *reprinted with permission of* Microwave Journal, Vol. V, No. 3, March 1962)

horn which at its throat region is excited in both the dominant TE_{11} and higher-order TM_{11} mode. A discontinuity is introduced at a position within the horn where two modes exist. The horn length is adjusted so that the superposition of the relative amplitudes of the two modes at the edges of the aperture is very small compared with the maximum aperture field magnitude. In addition, the dimensions of the horn are controlled so that the total phase at the aperture is such that, in conjunction with the desired amplitude distribution, it leads to side lobe suppression, beamwidth equalization, and phase center coincidence.

Qualitatively the pattern formation of a dual-mode conical horn operating in the TE_{11} and TM_{11} modes is accomplished by utilizing a pair of modes which have radiation functions with the same argument. However, one of the modes, in this case the TM_{11} mode, contains an additional envelope factor which varies very rapidly in the main beam region and remains relatively constant at large angles. Thus, it is possible to control the two modes in such a way that their fields cancel in all directions except within the main beam. The TM_{11} mode exhibits a null in its far-field pattern. Therefore a dual-mode conical horn possesses less axial gain than a conventional dominant-mode conical horn of the same aperture size. Because of that, dual-mode horns render better characteristics and are more attractive for applications where pattern plane symmetry and side lobe reduction are more important than maximum aperture efficiency. A most important application of a dual-mode horn is as a feed of Cassegrain reflector systems.

Dual-mode conical horns have been designed, built, and tested [39] with relatively good success in their performance. Generally, however, diagonal horns would be good competitors for the dual-mode horns if it were not for the undesirable characteristics (especially the cross-polarized components) that they exhibit in the very important 45° and 135° planes. Improved performance can be obtained from dual-mode horns if additional higher-order modes (such as the TE_{12}, TE_{13} and TM_{12}) are excited [40] and if their relative amplitudes and phases can be properly controlled. Computed

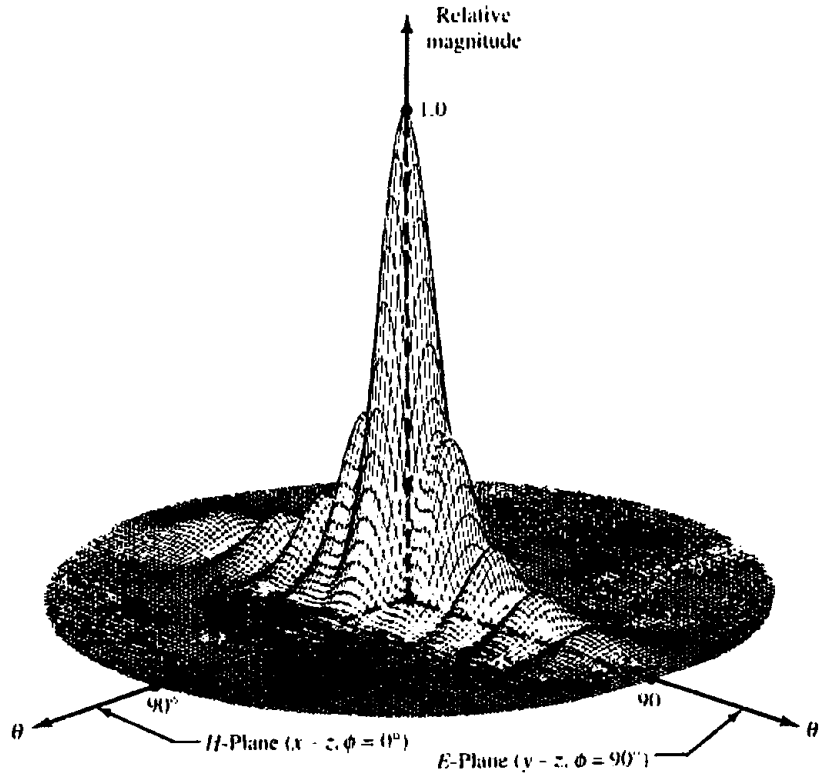

(a) Sum (TE_{10} + TE_{30} modes)

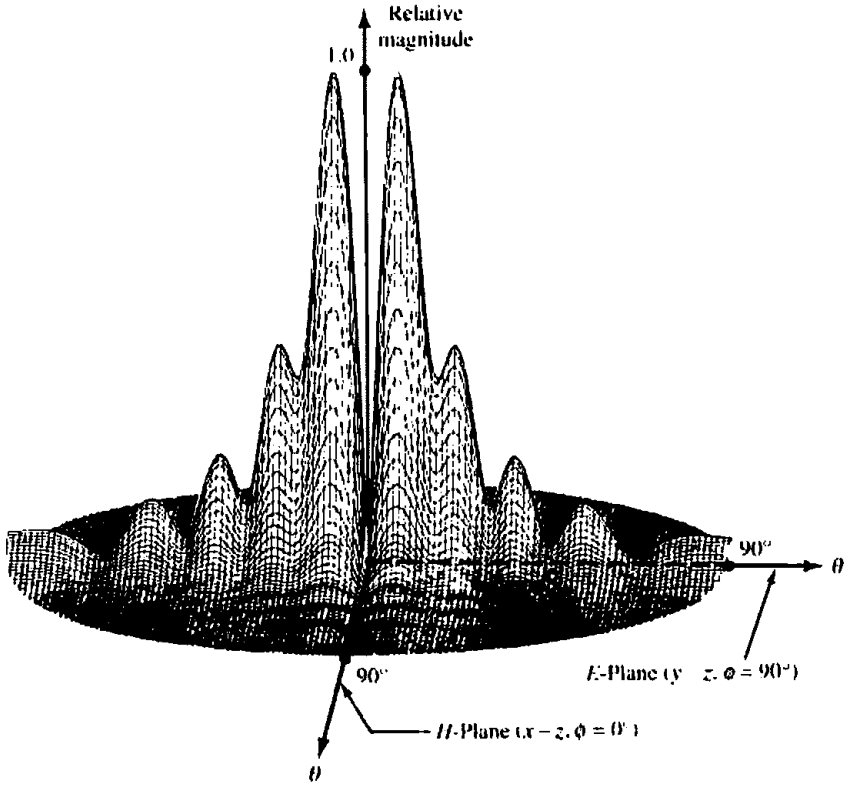

(b) E-plane difference (TE_{11} + TM_{11} modes)

Figure 13.37 Three-dimensional sum and difference (E- and H-planes) field patterns of a monopulse pyramidal horn. (C. A. Balanis, "Horn Antennas," in *Antenna Handbook* (Y. T. Lo and S. W. Lee, eds.). © 1988, Van Nostrand Reinhold Co., Inc.)

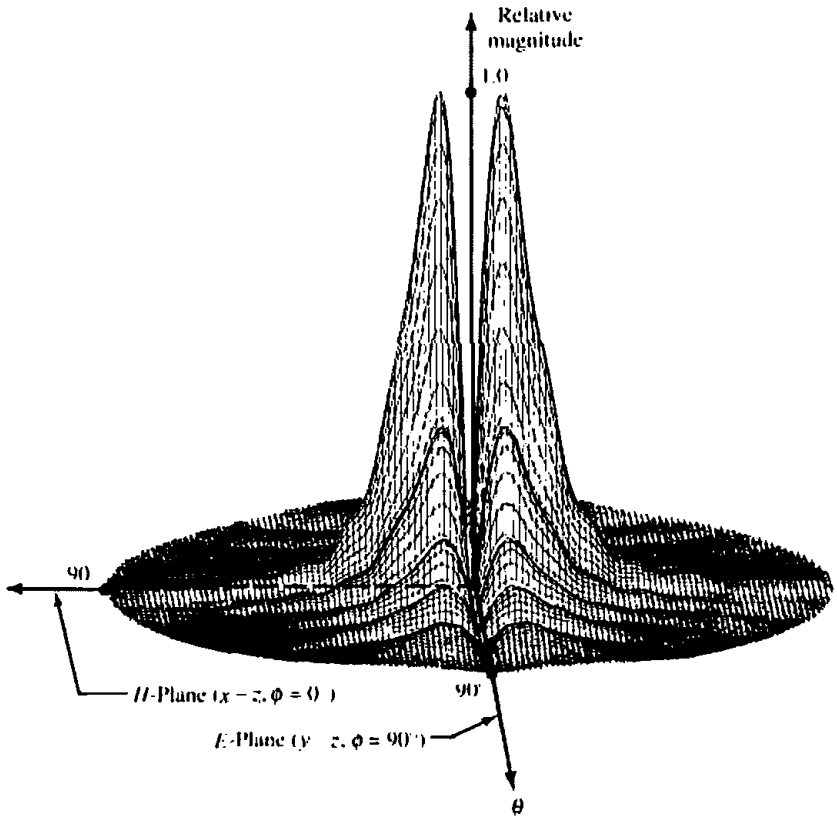

(c) *H*-plane difference (TE_{20} mode)

Figure 13.37 (Continued)

maximum aperture efficiencies of paraboloidal reflectors, using such horns as feeds, have reached 90% contrasted with efficiencies of about 76% for reflector systems using conventional dominant-mode horn feeds. In practice the actual maximum efficiency achieved is determined by the number of modes that can be excited and the degree to which their relative amplitudes and phases can be controlled.

The techniques of the dual-mode and multimode conical horns can be extended to the design of horns with rectangular cross sections. In fact a multimode pyramidal horn has been designed, built, and tested to be used as a feed in a low-noise Cassegrain monopulse system [41]. This rectangular pyramidal horn utilizes additional higher-order modes to provide monopulse capability, side lobe suppression in both the *E*- and *H*-planes, and beamwidth equalization. Specifically the various pattern modes for the monopulse system are formed in a single horn as follows:

(a) *Sum:* Utilizes $TE_{10} + TE_{30}$ instead of only TE_{10}. When the relative amplitude and phase excitations of the higher-order TE_{30} mode are properly adjusted, they provide side lobe cancellation at the second minor lobe of the TE_{10}-mode pattern

(b) *E-Plane Difference:* Utilizes $TE_{11} + TM_{11}$ modes

(c) *H-Plane Difference:* Utilizes TE_{20} mode

In its input the horn of [41] contained a four-guide monopulse bridge circuitry, a multimode matching section, a difference mode phasing section, and a sum mode excitation and control section. To illustrate the general concept, in Figure 13.37(a–c) are plots of three-dimensional patterns of the sum, *E*-plane difference, and *H*-plane difference modes which utilize, respectively, the $TE_{10} + TE_{30}$, $TE_{11} + TM_{11}$, and TE_{20}

modes. The relative excitation between the modes has been controlled so that each pattern utilizing multiple modes in its formation displays its most attractive features for its function.

13.9 DIELECTRIC-LOADED HORNS

Over the years much effort has been devoted in enhancing the antenna and aperture efficiencies of aperture antennas, especially for those that serve as feeds for reflectors (such as the horn). One technique that was proposed and then investigated was to use dielectric guiding structures, referred to as *Dielguides* [42], between the primary feed and the reflector (or subreflector). The technique is simple and inexpensive to implement and provides broadband, highly efficient, and low-noise antenna feeds. The method negates the compromise between taper and spillover efficiencies, and it is based on the principle of internal reflections, which has been utilized frequently in optics. Its role bears a very close resemblance to that of a lens, and it is an extension of the classical parabolic-shaped lens to other geometrical shapes.

Another method that has been used to control the radiation pattern of electromagnetic horns is to insert totally within them various shapes of dielectric material (wedges, slabs, etc.) [43]–[51] to control in a predictable manner not only the phase distribution over the aperture, as is usually done by using the classical parabolic lenses, but also to change the power (amplitude) distribution over the aperture. The control of the amplitude and phase distributions over the aperture are very essential in the design of very low side lobe antenna patterns.

Symmetrical loading of the H-plane walls has also been utilized, by proper parameter selection, to create a dominant longitudinal section electric (LSE) mode and to enhance the aperture efficiency and pattern-shaping capabilities of symmetrically loaded horns [43]. The method is simple and inexpensive, and it can also be utilized to realize high efficiency from small horns which can be used in limited scan arrays. Aperture efficiencies on the order of 92 to 96% have been attained, in contrast to values of 81% for unloaded horns.

A similar technique has been suggested to symmetrically load the E-plane walls of rectangular horns [45]–[51] and eventually to line all four of its walls with dielectric slabs. Other similar techniques have been suggested, and a summary of these and other classical papers dealing with dielectric-loaded horns can be found in [1].

13.10 PHASE CENTER

Each far-zone field component radiated by an antenna can be written, in general, as

$$\mathbf{E}_u = \hat{\mathbf{u}} E(\theta, \phi) e^{j\psi(\theta,\phi)} \frac{e^{-jkr}}{r} \tag{13-63}$$

where $\hat{\mathbf{u}}$ is a unit vector. The terms $E(\theta, \phi)$ and $\psi(\theta, \phi)$ represent, respectively, the (θ, ϕ) variations of the amplitude and phase.

In navigation, tracking, homing, landing, and other aircraft and aerospace systems it is usually desirable to assign to the antenna a reference point such that for a given frequency, $\psi(\theta, \phi)$ of (13-63) is independent of θ and ϕ (i.e., $\psi(\theta, \phi) =$ constant). The reference point which makes $\psi(\theta, \phi)$ independent of θ and ϕ is known as the *phase center* of the antenna [52]–[56]. When referenced to the phase center, the fields radiated by the antenna are spherical waves with ideal spherical wave fronts or

equiphase surfaces. Therefore a phase center is a reference point from which radiation is said to emanate, and radiated fields measured on the surface of a sphere whose center coincides with the phase center have the same phase.

For practical antennas such as arrays, reflectors, and others, a single unique phase center valid for all values of θ and ϕ does not exist; for most, however, their phase center moves along a surface, and its position depends on the observation point. However, in many antenna systems a reference point can be found such that $\psi(\theta, \phi)$ = constant, or nearly so, over most of the angular space, especially over the main lobe. When the phase center position variation is sufficiently small, that point is usually referred to as the *apparent phase center.*

The need for the phase center can best be explained by examining the radiation characteristics of a paraboloidal reflector (parabola of revolution). Plane waves incident on a paraboloidal reflector focus at a single point which is known as the *focal point.* Conversely, spherical waves emanating from the focal point are reflected by the paraboloidal surface and form plane waves. Thus in the receiving mode all the energy is collected at a single point. In the transmitting mode, ideal plane waves are formed if the radiated waves have spherical wavefronts and emanate from a single point.

In practice, no antenna is a point source with ideal spherical equiphases. Many of them, however, contain a point from which their radiation, over most of the angular space, seems to have spherical wavefronts. When such an antenna is used as a feed for a reflector, its phase center must be placed at the focal point. Deviations of the feed from the focal point of the reflector lead to phase errors which result in significant gain reductions of the antenna, as illustrated in Section 15.4.1(G) of Chapter 15.

The analytical formulations for locating the phase center of an antenna are usually very laborious and exist only for a limited number of configurations [52]–[54]. Experimental techniques [55], [56] are available to locate the phase center of an antenna. The one reported in [55] is also discussed in some detail in [2], and it will not be repeated here. The interested reader is referred to [2] and [55].

The horn is a microwave antenna that is widely used as a feed for reflectors [57]. To perform as an efficient feed for reflectors, it is imperative that its phase center is known and it is located at the focal point of the reflector. Instead of presenting analytical formulations for the phase center of a horn, graphical data will be included to illustrate typical phase centers.

Usually the phase center of a horn is not located at its mouth (throat) or at its aperture but mostly between its imaginary apex point and its aperture. The exact location depends on the dimensions of the horn, especially on its flare angle. For large flare angles the phase center is closer to the apex. As the flare angle of the horn becomes smaller, the phase center moves toward the aperture of the horn.

Computed phase centers for an E-plane and an H-plane sectoral horn are displayed in Figure 13.38(a,b). It is apparent that for small flare angles the E- and H-plane phase centers are identical. Although each specific design has its own phase center, the data of Figure 13.38(a,b) are typical. If the E- and H-plane phase centers of a pyramidal horn are not identical, its phase center can be taken to be the average of the two.

Phase center nomographs for conical corrugated and uncorrugated (TE_{11}-mode) horns are available [54], and they can be found in [2] and [54]. The procedure to use these in order to locate a phase center is documented in [2] and [54], and it is not repeated here. The interested reader is referred to [2] where examples are also illustrated.

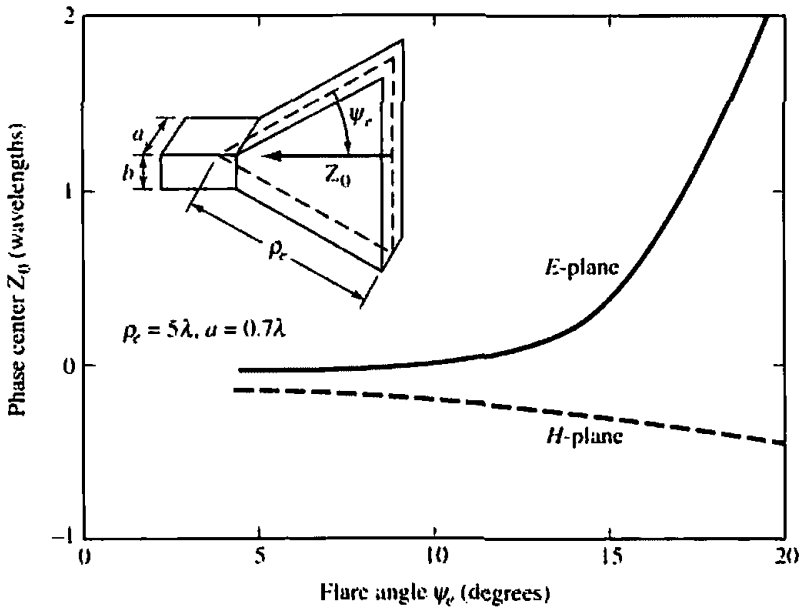

(a) E-plane

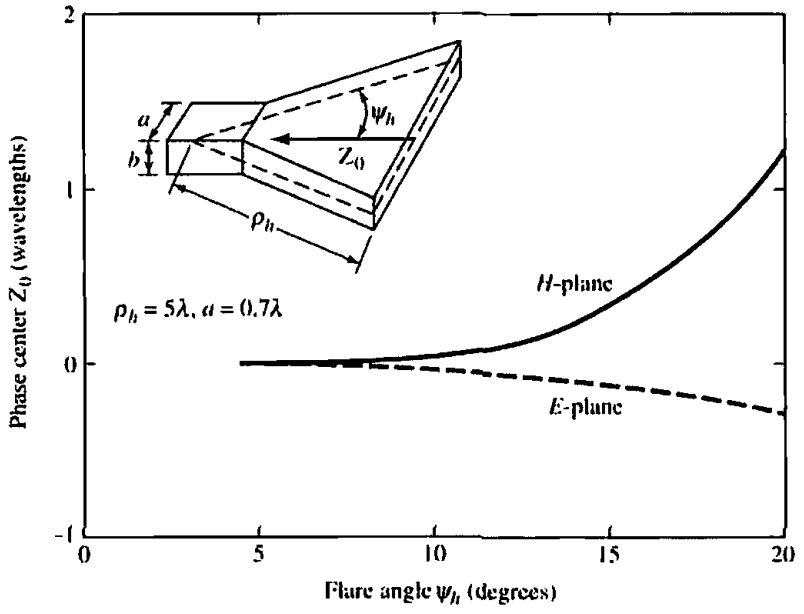

(b) H-plane

Figure 13.38 Phase center location, as a function of flare angle, for E- and H-plane sectoral horns. (*Adapted from Hu* [52])

References

1. A. W. Love, *Electromagnetic Horn Antennas*, IEEE Press, New York, 1976.
2. C. A. Balanis, "Horn Antennas," Chapter 8 in *Antenna Handbook: Theory, Applications and Design* (Y. T. Lo and S. W. Lee, eds.), Van Nostrand Reinhold Co., New York, 1988.
3. A. W. Love, "Horn Antennas," Chapter 15 in *Antenna Engineering Handbook* (R. C. Johnson and H. Jasik, eds.), New York, 1984.
4. R. F. Harrington, *Time-Harmonic Electromagnetic Fields*, McGraw-Hill, New York, 1961, pp. 208–213.

5. S. Silver (ed.). *Microwave Antenna Theory and Design*, MIT Radiation Laboratory Series, Vol. 12, McGraw-Hill, New York, 1949, pp. 349–376.
6. C. A. Balanis, *Advanced Engineering Electromagnetics*, John Wiley and Sons, New York, 1989.
7. M. J. Maybell and P. S. Simon, "Pyramidal Horn Gain Calculation with Improved Accuracy," *IEEE Trans. Antennas Propagat.*, Vol. 41, No. 7, pp. 884–889, July 1993.
8. K. Liu, C. A. Balanis, C. R. Birtcher and G. C. Barber, "Analysis of Pyramidal Horn Antennas Using Moment Method," *IEEE Trans. Antennas Propagat.*, Vol. 41, No. 10, pp. 1379–1389, October 1993.
9. M. Abramowitz and I. A. Stegun (eds.), *Handbook of Mathematical Functions*, National Bureau of Standards, United States Dept. of Commerce, June 1964.
10. J. Boersma, "Computation of Fresnel Integrals," *Math. Comp.*, Vol. 14, p. 380, 1960.
11. Y.-B. Cheng, "Analysis of Aircraft Antenna Radiation for Microwave Landing System Using Geometrical Theory of Diffraction," MSEE Thesis, Dept. of Electrical Engineering, West Virginia University, pp. 208–211, 1976.
12. E. V. Jull, "Gain of an E-Plane Sectoral Horn–A Failure of the Kirchoff Theory and a New Proposal," *IEEE Trans. Antennas Propagat.*, Vol. AP-22, No. 2, pp. 221–226, March 1974.
13. E. V. Jull, *Aperture Antennas and Diffraction Theory*, Peter Peregrinus Ltd., London, United Kingdom, pp. 55–65, 1981.
14. E. H. Braun, "Some Data for the Design of Electromagnetic Horns," *IRE Trans. Antennas Propagat.*, Vol. AP-4, No. 1, pp. 29–31, January 1956.
15. P. M. Russo, R. C. Rudduck, and L. Peters, Jr., "A Method for Computing *E*-Plane Patterns of Horn Antennas," *IEEE Trans. Antennas Propagat.*, Vol. AP-13, No. 2, pp. 219–224, March 1965.
16. J. S. Yu, R. C. Rudduck, and L. Peters, Jr., "Comprehensive Analysis for *E*-Plane of Horn Antennas by Edge Diffraction Theory," *IEEE Trans. Antennas Propagat.*, Vol. AP-14, No. 2, pp. 138–149, March 1966.
17. M. A. K. Hamid, "Diffraction by a Conical Horn," *IEEE Trans. Antennas Propagat.*, Vol. AP-16, No. 5, pp. 520–528, September 1966.
18. M. S. Narasimhan and M. S. Shehadri, "GTD Analysis of the Radiation Patterns of Conical Horns," *IEEE Trans. Antennas Propagat.*, Vol. AP-26, No. 6, pp. 774–778, November 1978.
19. P. A. Tirkas and C. A. Balanis, "Contour Path FDTD Method for Analysis of Pyramidal Horns with Composite Inner E-Plane Walls," *IEEE Trans. Antennas Propagat.*, Vol. AP-42, No. 11, pp. 1476–1483, November 1994.
20. M. G. Schorr and F. J. Beck, Jr., "Electromagnetic Field of a Conical Horn," *J. Appl. Phys.*, Vol. 21, pp. 795–801, August 1950.
21. A. P. King, "The Radiation Characteristics of Conical Horn Antennas," *Proc. IRE*, Vol. 38, pp. 249–251, March 1950.
22. A. F. Kay, "The Scalar Feed," AFCRL Rep. 64-347, AD601609, March 1964.
23. R. E. Lawrie and L. Peters, Jr., "Modifications of Horn Antennas for Low Side Lobe Levels," *IEEE Trans. Antennas Propagat.*, Vol. AP-14, No. 5, pp. 605–610, September 1966.
24. R. S. Elliott, "On the Theory of Corrugated Plane Surfaces," *IRE Trans. Antennas Propagat.*, Vol. AP-2, No. 2, pp. 71–81, April 1954.
25. C. A. Mentzer and L. Peters, Jr., "Properties of Cutoff Corrugated Surfaces for Corrugated Horn Design," *IEEE Trans. Antennas Propagat.*, Vol. AP-22, No. 2, pp. 191–196, March 1974.
26. C. A. Mentzer and L. Peters, Jr., "Pattern Analysis of Corrugated Horn Antennas," *IEEE Trans. Antennas Propagat.*, Vol. AP-24, No. 3, pp. 304–309, May 1976.
27. M. J. Al-Hakkak and Y. T. Lo, "Circular Waveguides and Horns with Anisotropic and Corrugated Boundaries," *Antenna Laboratory Report No. 73-3*, Department of Electrical Engineering, University of Illinois, Urbana, January 1973.

28. B. MacA. Thomas, G. L. James and K. J. Greene, "Design of Wide-Band Corrugated Conical Horns for Cassegrain Antennas," *IEEE Trans. Antennas Propagat.*, Vol. AP-34, No. 6, pp. 750–757, June 1986.
29. B. MacA. Thomas, "Design of Corrugated Conical Horns," *IEEE Trans. Antennas Propagat.*, Vol. AP-26, No. 2, pp. 367–372, March 1978.
30. B. MacA. Thomas and K. J. Greene, "A Curved-Aperture Corrugated Horn Having Very Low Cross-Polar Performance," *IEEE Trans. Antennas Propagat.*, Vol. AP-30, No. 6, pp. 1068–1072, November 1982.
31. G. L. James, "TE_{11}-to-HE_{11} Mode Converters for Small-Angle Corrugated Horns," *IEEE Trans. Antennas Propagat.*, Vol. AP-30, No. 6, pp. 1057–1062, November 1982.
32. K. Tomiyasu, "Conversion of TE_{11} mode by a Large-Diameter Conical Junction," *IEEE Trans. Microwave Theory Tech.*, Vol. MTT-17, No. 5, pp. 277–279, May 1969.
33. B. MacA. Thomas, "Mode Conversion Using Circumferentially Corrugated Cylindrical Waveguide," *Electronic Letters*, Vol. 8, pp. 394–396, 1972.
34. J. K. M. Jansen and M. E. J. Jeuken, "Surface Waves in Corrugated Conical Horn," *Electronic Letters*, Vol. 8, pp. 342–344, 1972.
35. Y. Tacheichi, T. Hashimoto, and F. Takeda, "The Ring-Loaded Corrugated Waveguide," *IEEE Trans. Microwave Theory Tech.*, Vol. MTT-19, No. 12, pp. 947–950, December 1971.
36. F. Takeda and T. Hashimoto, "Broadbanding of Corrugated Conical Horns by Means of the Ring-Loaded Corrugated Waveguide Structure," *IEEE Trans. Antennas Propagat.*, Vol. AP-24, No. 6, pp. 786–792, November 1976.
37. W. D. Burnside and C. W. Chuang, "An Aperture-Matched Horn Design," *IEEE Trans. Antennas Propagat.*, Vol. AP-30, No. 4, pp. 790–796, July 1982.
38. A. W. Love, "The Diagonal Horn Antenna," *Microwave Journal*, Vol. V, pp. 117–122, March 1962.
39. P. D. Potter, "A New Horn Antenna with Suppressed Side Lobes and Equal Beamwidths," *Microwave Journal*, pp. 71–78, June 1963.
40. P. D. Potter and A. C. Ludwig, "Beamshaping by Use of Higher-Order Modes in Conical Horns," *Northeast Electron. Res. and Eng. Mtg.*, pp. 92–93, November 1963.
41. P. A. Jensen, "A Low-Noise Multimode Cassegrain Monopulse with Polarization Diversity," *Northeast Electron. Res. and Eng. Mtg.*, pp. 94–95, November 1963.
42. H. E. Bartlett and R. E. Moseley, "Dielguides—Highly Efficient Low-Noise Antenna Feeds," *Microwave Journal*, Vol. 9, pp. 53–58, December 1966.
43. L. L. Oh, S. Y. Peng, and C. D. Lunden, "Effects of Dielectrics on the Radiation Patterns of an Electromagnetic Horn," *IEEE Trans. Antennas Propagat.*, Vol. AP-18, No. 4, pp. 553–556, July 1970.
44. G. N. Tsandoulas and W. D. Fitzgerald, "Aperture Efficiency Enhancement in Dielectrically Loaded Horns," *IEEE Trans. Antennas Propagat.*, Vol. AP-20, No. 1, pp. 69–74, January 1972.
45. R. Baldwin and P. A. McInnes, "Radiation Patterns of Dielectric Loaded Rectangular Horns," *IEEE Trans. Antennas Propagat.*, Vol. AP-21, No. 3, pp. 375–376, May 1973.
46. C. M. Knop, Y. B. Cheng, and E. L. Osterlag, "On the Fields in a Conical Horn Having an Arbitrary Wall Impedance," *IEEE Trans. Antennas Propagat.*, Vol. AP-34, No. 9, pp. 1092–1098, September 1986.
47. J. J. H. Wang, V. K. Tripp, and R. P. Zimmer, "Magnetically Coated Horn for Low Sidelobes and Low Cross-Polarization," *IEE Proceedings*, Vol. 136, pp. 132–138, April 1989.
48. J. J. H. Wang, V. K. Tripp, and J. E. Tehan, "The Magnetically Coated Conducting Surface as a Dual Conductor and Its Application to Antennas and Microwaves," *IEEE Trans. Antennas Propagat.*, Vol. AP-38, No. 7, pp. 1069–1077, July 1990.
49. K. Liu and C. A. Balanis, "Analysis of Horn Antennas with Impedance Walls," *1990 IEEE Antennas and Propagatation Symposium Digest*, Vol. 1, pp. 1184–1187, May 7–11, 1990, Dallas, TX.

50. K. Liu and C. A. Balanis, "Low-Loss Material Coating for Horn Antenna Beam Shaping," *1991 IEEE Antennas and Propagatation Symposium Digest*, Vol. 3, pp. 1664–1667, June 24–28, 1991, London, Ontario, Canada.
51. P. A. Tirkas, "Finite-Difference Time-Domain for Aperture Antenna Radiation," PhD Dissertation, Dept. of Electrical Engineering, Arizona State University, December 1993.
52. Y. Y. Hu, "A Method of Determining Phase Centers and Its Applications to Electromagnetic Horns," *Journal of the Franklin Institute*, Vol. 271, pp. 31–39, January 1961.
53. E. R. Nagelberg, "Fresnel Region Phase Centers of Circular Aperture Antennas," *IEEE Trans. Antennas Propagat.*, Vol. AP-13, No. 3, pp. 479–480, May 1965.
54. I. Ohtera and H. Ujiie, "Nomographs for Phase Centers of Conical Corrugated and TE_{11} Mode Horns," *IEEE Trans. Antennas Propagat.*, Vol. AP-23, No. 6, pp. 858–859, November 1975.
55. J. D. Dyson, "Determination of the Phase Center and Phase Patterns of Antennas," in *Radio Antennas for Aircraft and Aerospace Vehicles*, W. T. Blackband (ed.), AGARD Conference Proceedings, No. 15, Slough, England Technivision Services, 1967.
56. M. Teichman, "Precision Phase Center Measurements of Horn Antennas," *IEEE Trans. Antennas Propagat.*, Vol. AP-18, No. 5, pp. 689–690, September 1970.
57. W. M. Truman and C. A. Balanis, "Optimum Design of Horn Feeds for Reflector Antennas," *IEEE Trans. Antennas Propagat.*, Vol. AP-22, No. 4, pp. 585–586, July 1974.

PROBLEMS

13.1. Derive (13-1a)–(13-1c) by treating the E-plane horn as a radial waveguide.

13.2. Design an E-plane horn such that the maximum phase difference between two points at the aperture, one at the center and the other at the edge, is 120°. Assuming that the maximum length along its wall (ρ_e), measured from the aperture to its apex, is 10λ, find the
(a) maximum total flare angle of the horn
(b) largest dimension of the horn at the aperture
(c) directivity of the horn (dimensionless and in dB)
(d) gain of the antenna (in dB) when the reflection coefficient within the waveguide feeding the horn is 0.2. Assume only mismatch losses. The waveguide feeding the horn has dimensions of 0.5λ and 0.25λ

13.3. For an E-plane horn with $\rho_1 = 6\lambda$, $b_1 = 3.47\lambda$, and $a = 0.5\lambda$,
(a) compute (in dB) its pattern at $\theta = 0°$, 10°, and 20° using the results of Figure 13.6. Show all the steps for one angle.
(b) compute its directivity using (13-19) and (13-20c). Compare the answers.

13.4. Repeat Problem 13.3 for $\rho_1 = 6\lambda$, $b_1 = 6\lambda$, and $a = 0.5\lambda$.

13.5. For an E-plane sectoral horn, plot b_1 (in λ) versus ρ_1 (in λ) using (13-19a). Verify, using the data of Figure 13.8, that the maximum directivities occur when (13-19a) is satisfied.

13.6. For an E-plane sectoral horn with $\rho_1 = 20\lambda$, $a = 0.5\lambda$
(a) find its optimum aperture dimensions for maximum normalized directivity
(b) compute the total flare angle of the horn
(c) compute its directivity, using (13-19), and compare it with the graphical answer
(d) find its half-power beamwidth (in degrees)
(e) compute the directivity using (13-20c)

13.7. An E-plane horn is fed by an X-band WR 90 rectangular waveguide with inner dimensions of 0.9 in. (2.286 cm) and $b = 0.4$ in. (1.016 cm). Design the horn so that its maximum directivity at $f = 11$ GHz is 30 (14.77 dB).

13.8. Design an optimum directivity E-plane sectoral horn whose axial length is $\rho_1 = 10\lambda$. The horn is operating at X-band with a desired center frequency equal to $f = 10$ GHz.

The dimensions of the feed waveguide are $a = 0.9$ in. (2.286 cm) and $b = 0.4$ in. (1.016 cm). Assuming an 100% efficient horn ($e_t = 1$), find the
(a) horn aperture dimensions b_1 and ρ_e (in wavelengths), and flare half-angle ψ_e (in degrees)
(b) directivity D_E (in dB) using (13-20c)
(c) aperture efficiency
(d) largest phase difference (in degrees) between center of horn at the aperture and any point on the horn aperture along the principal E-plane

13.9. Derive (13-21a)–(13-21e) by treating the H-plane horn as a radial waveguide.

13.10. For an H-plane sectoral horn with $\rho_2 = 6\lambda$, $a_1 = 6\lambda$, and $b = 0.25\lambda$ compute the
(a) directivity (in dB) using (13-41), (13-42c) and compare the answers
(b) normalized field strength (in dB) at $\theta = 30°$, 45°, and 90°. Approximate it using linear interpolation

13.11. For an H-plane sectoral horn, plot a_1 (in λ) versus ρ_2 (in λ) using (13-41c). Verify, using the data of Figure 13.16, that the maximum directivities occur when (13-41c) is satisfied.

13.12. An H-plane sectoral horn is fed by an X-band WR 90 rectangular waveguide with dimensions of $a = 0.9$ in. (2.286 cm) and $b = 0.4$ in. (1.016 cm). Design the horn so that its maximum directivity at $f = 11$ GHz is 16.3 (12.12 dB).

13.13. Repeat the design of Problem 13.8 for an H-plane sectoral horn where axial length is also $\rho_2 = 10\lambda$. The feed waveguide dimensions and center frequency of operation are the same as in Problem 13.8. Assuming an 100% efficient horn ($e_t = 1$), find the
(a) horn aperture dimensions a_1 and ρ_h (in wavelengths), and the flare half-angle ψ_h (in degrees)
(b) directiviy D_H (in dB) using (13-42c)
(c) aperture efficiency
(d) largest phase difference (in degrees) between center of horn at the aperture and any point on the horn aperture along the principal H-plane

13.14. Show that (13-49a) and (13-49b) must be satisfied in order for a pyramidal horn to be physically realizable.

13.15. A standard gain X-band (8.2–12.4 GHz) pyramidal horn has dimensions of $\rho_1 \approx 13.5$ *in. (34.29 cm)*, $\rho_2 \approx 14.2$ *in. (36.07 cm)*, $a_1 = 7.65$ *in. (19.43 cm)*, $b_1 = 5.65$ *in.* (14.35 cm), $a = 0.9$ in. (2.286 cm), and $b = 0.4$ in. (1.016 cm).
(a) Check to see if such a horn can be constructed physically.
(b) Compute the directivity (in dB) at $f = 8.2$, 10.3, 12.4 GHz using for each (13-52a), (13-53), and (13-54e). Compare the answers. Verify with the computer program PYRAMIDAL HORN-ANALYSIS at the end of this chapter.

13.16. A standard gain X-band (8.2–12.4 GHz) pyramidal horn has dimensions of $\rho_1 \approx 5.3$ in. (13.46 cm), $\rho_2 = 6.2$ in. (15.75 cm), $a_1 = 3.09$ in. (7.85 cm), $b_1 = 2.34$ in. (5.94 cm), $a = 0.9$ in. (2.286 cm), and $b \approx 0.4$ in. (1.016 cm).
(a) Check to see if such a horn can be constructed physically.
(b) Compute the directivity (in dB) at $f = 8.2$, 10.3, 12.4 GHz using for each (13-52a), (13-53), and (13-54e). Compare the computed answers with the gains of Figure 13.24. Verify with the computer program PYRAMIDAL HORN-ANALYSIS at the end of this chapter.

13.17. Repeat the design of the optimum X-band pyramidal horn of Example 13.6 so that the gain at $f = 11$ GHz is 17.05 dB.

13.18. Design a pyramidal horn antenna with optimum gain at a frequency of 10 GHz. The overall length of the antenna from the imaginary vertex of the horn to the center of the aperture is 10λ and is nearly the same in both planes. Determine the
(a) Aperture dimension of the horn (in cm).
(b) Gain of the antenna (in dB)
(c) Aperture efficiency of the antenna (in %). Assume the reflection, conduction and dielectric losses of the antenna are negligible.

(d) Power delivered to a matched load when the incident power density is 10μ watts/m^2.

13.19. Design an optimum gain C-band (3.95–5.85 GHz) pyramidal horn so that its gain at $f = 4.90$ GHz is 20.0 dBi. The horn is fed by a WR 187 rectangular waveguide with inner dimensions of $a = 1.872$ in. (4.755 cm) and $b = 0.872$ in. (2.215 cm). Refer to Figure 13.18 for the horn geometry. Determine in cm, the remaining dimensions of the horn: ρ_e, ρ_h, a_1, b_1, p_e, and p_h. Verify using the computer program PYRAMIDAL HORN-DESIGN at the end of this chapter.

13.20. For a conical horn, plot d_m (in λ) versus l (in λ) using (13-60). Verify, using the data of Figure 13.27, that the maximum directivities occur when (13-60) is satisfied.

13.21. A conical horn has dimensions of $L = 19.5$ in. (49.53 cm), $d_m = 15$ in. (38.10 cm), and $d = 2.875$ in. (7.3025 cm).

(a) Find the frequency (in GHz) which will result in maximum directivity for this horn. What is that directivity (in dB)?

(b) Find the directivity (in dB) at 2.5 and 5 GHz.

(c) Compute the cutoff frequency (in GHz) of the TE_{11}-mode which can exist inside the circular waveguide that is used to feed the horn.

13.22. Design an optimum directivity conical horn, using (13-59)–(13-60), so that its directivity (above isotropic) at $f = 11$ GHz is 22.6 dB. Check your design with the data in Figure 13.27. Compare the design dimensions with those of the pyramidal horn of Example 13.6.

13.23. Design an optimum directivity conical horn so that its directivity at 10 GHz (above a standard gain horn of 15 dB directivity) is 5 dB. Determine the horn diameter (in cm) and its flare angle (in degrees).

13.24. As part of a 10-GHz microwave communication system, you purchase a horn antenna that is said to have a directivity of 75. The conduction and dielectric losses of the antenna are negligible, and the horn is polarization matched to the incoming signal. A standing wave meter indicates a voltage reflection coefficient of 0.1 at the antenna-waveguide junction.

(a) Calculate the maximum effective aperture of the horn.

(b) If an impinging wave with a uniform power density of 1 μ watts/m^2 is incident upon the horn, what is the maximum power delivered to a load which is connected and matched to the lossless waveguide?

13.25. For an X-band pyramidal corrugated horn operating at 10.3 GHz, find the

(a) smallest lower and upper limits of the corrugation depths (in cm)

(b) width w of each corrugation (in cm)

(c) width t of each corrugation tooth (in cm)

13.26. Find the E- and H-plane phase centers (in λ) of

(a) an E-plane ($\rho_e = 5\lambda$, $a = 0.7\lambda$)

(b) an H-plane ($\rho_h = 5\lambda$, $a = 0.7\lambda$)

sectoral horn with a total included angle of 30°.

COMPUTER PROGRAM - PYRAMIDAL HORN: ANALYSIS

```
C*************************************************************
C THIS IS A FORTRAN PROGRAM THAT COMPUTES FOR A PYRAMIDAL
C HORN THE:
C
C     I.   FAR-ZONE E- AND H-PLANE AMPLITUDE PATTERNS
C          BASED ON THE THEORY OF SECTION 13.4,
C          EQUATIONS (13-46) - (13-48c)
C     II.  DIRECTIVITY (in dB) BASED ON EQUATION (13-52)
C     III. DIRECTIVITY (in dB) OF THE CORRESPONDING E-PLANE
C          SECTORAL HORN BASED ON EQUATION (13-19)
C     IV.  DIRECTIVITY (in dB) OF THE CORRESPONDING H-PLANE
C          SECTORAL HORN BASED ON EQUATION (13-41)
C
C TO COMPUTE THE DESIRED HORN RADIATION CHARACTERISTICS:
C
C       **INPUT PARAMETERS
C       1. ρ1 =  RHO1 (in λ)
C       2. ρ2 =  RHO2 (in λ)
C       3. a & b    =  WAVEGUIDE DIMENSIONS (in λ)
C       4. a1 & b1  =  HORN APERTURE DIMENSIONS (in λ)
C
C       **NOTES
C       1. REFER TO FIGURE 13.18 FOR THE GEOMETRY
C       2. THE E- AND H-PLANE AMPLITUDE PATTERNS ARE STORED IN TW
C          DATA FILES; NAMELY, E-theta.dat AND E-phi.dat, RESPECTIVELY.
C
C*************************************************************
```

COMPUTER PROGRAM - PYRAMIDAL HORN: DESIGN

```
C*****************************************************************
C
C THIS IS A FORTRAN PROGRAM THAT DESIGNS AN OPTIMUM GAIN
C PYRAMIDAL HORN BASED ON THE FORMULATION OF SECTION 13.4.3,
C EQUATIONS (13-55) - (13-58b).
C
C THE PROGRAM COMPUTES THE:
C
C     I.  HORN DIMENSIONS a1, b1, RHOE ρe, RHOH ρh, pe and
C         ph (in cm)
C     II. HORN FLARE ANGLES PSIE ψe AND PSIH ψh (in degrees)
C
C TO DESIGN THE HORN:
C
C       **INPUT PARAMETERS
C       1. Go    =  DESIRED GAIN (in dB)
C       2. F     =  FREQUENCY (in GHz)
C       3. a & b =  FEED RECTANGULAR WAVEGUIDE DIMENSIONS (in cm)
C
C       **NOTES
C       1. REFER TO FIGURE 13.18 FOR THE GEOMETRY
C       2. THIS PROGRAM USES A BISECTION METHOD ROUTINE TO FIND
C          THE ROOT OF THE DESIGN EQUATION (see NUMERICAL RECIPES
C          IN FORTRAN, SECOND EDITION, PAGE 347)
C
C*****************************************************************
```